acta mechanica et automatica, vol.13 no.2 (2019)

CONTENTS

Patryk Różyło
Passive Safety of a Buggy Type Car in the Aspect of a Dynamic Analysis of the Frame 75

Eugene Safronov, Andrey Nosko
A Method to Determine Allowable Speed for a Unit Load in a Pallet Flow Rack 80

Vladimir Morkun, Ihor Kotov
Intellectualization of Emergency Control of Power Systems on the Basis of Incorporated Ontologies of Knowledge-Bases 86

Volodymyr Iasnii, Petro Yasniy
Degradation of Functional Properties of Pseudoelastic NiTi Alloy under Cyclic Loading: an Experimental Study 95

Oleh Knysh, Ivan Rehei, Nazar Kandiak, Serhij Ternytskyi
Experimental Evaluation of the Tractive Effort of the Chain Conveyor During Book Block Spine Processing by Cylindrical Milling Cutter at Perfect Binding 101

Leon Kukiełka, Radosław Patyk, Łukasz Bohdal, Wojciech Napadłek, Rafał Gryglicki, Piotr Kasprzak
Investigations of Polypropylene Foil Cutting Process Using Fiber Nb:Yag and Diode Nd:YVO4 Lasers 107

Vladimir Golik, Vladimir Morkun, Natalia Morkun, Vitaliy Tron
Investigation of Mechanochemical Leaching of Non-Ferrous Metals 113

Dorota Kula, Ewaryst Wierzbicki
Surface Localized Heat Transfer Equation for Periodic Composites 124

Zenon Hendzel, Jakub Wiech
Robotic Swarm Self-Organization Control 130

Maciej Rosół, Bogdan Sapiński
Ability of Energy Harvesting MR Damper to Act as a Velocity Sensor in Vibration Control Systems 135

Abstracts 146

sciendo
DOI 10.2478/ama-2019-0010 acta mechanica et automatica, vol.13 no.2 (2019)

PASSIVE SAFETY OF A BUGGY-TYPE CAR IN THE ASPECT OF A DYNAMIC ANALYSIS OF THE FRAME

Patryk RÓŻYŁO[*]

[*]Faculty of Mechanical Engineering, Department of Machine Design and Mechatronics, Lublin University of Technology, ul. Nadbystrzycka 36, 20-618 Lublin, Poland

p.rozylo@pollub.pl

received 4 October 2018, revised 24 April 2019, accepted 30 April 2019

Abstract: This article presents passive safety issues of a buggy-type car. The issue has been presented in the context of the dynamic impact analysis of the aluminium frame of the vehicle into a rigid wall. The study was conducted using the finite element method in the Abaqus® software. With regard to numerical calculations, a dynamic impact simulation was performed, which defined the critical areas of the structure. Numerical analysis allowed to obtain both the state of the strain of the frame structure and the characteristics of the construction work during the impact. The results of the research provide high-quality prepared FEM model.

Key words: Passive Safety, Finite Element Method, Dynamic Impact Analysis, Overload, Abaqus

1. INTRODUCTION

Nowadays, the safety aspect of drivers, passengers and other members of the traffic plays an important role in the automotive industry. Constant striving to minimise the harm resulting from a collision is a major aspect of the need to increase the level of road safety. The most advantageous solution, directly affecting the safety level in the event of potential collisions, is the ability to disperse kinetic energy within the plastic deformation of the structure. The work mainly involved passive safety issues. Passive safety constitutes a very important issue regarding the driving of passenger cars. Generalised division of security into passive and active was made by Bel Barneyi and Hans Scherenberg (Autokult, 2014). The division of passive and active safety in the automotive industry has been widely used since 1966 up to today. Passive safety systems provide all technical solutions to ensure the maximum possible protection for the driver and passengers in the event of a potential collision (Bolton, 1982). The additional task of this type of solution is also to reduce the impact of accidents on people being outside the vehicle. A brand known today as Mercedes-Benz (Bolton, 1982) is the precursor of passive safety in vehicles. The most important elements of the vehicle taking direct part in the process of increasing passive safety are the right bodywork and chassis. The right bodywork design, including lateral reinforcements, controlled crumple zone and ‘safety cage’, has a direct impact on collision safety. In addition, most vehicles have a collapsible steering column that absorbs part of the impact energy, seat belts, airbag systems, head restraints, engine mountings that prevent it from being in contact with people in the vehicle and no curved and sharp elements around the dashboard – increased security. Figure 1 shows exemplary front and lateral reinforcement and controlled crumple zones.

One of the most important elements of a vehicle design that directly affects passive safety is the vehicle frame. The design provides any reinforcements against lateral impacts, safety cage or additional crumple zones (Milanowicz et al., 2018) – the purpose of which is to absorb energy (Estrada et al., 2017).

Fig. 1. Reinforcement of the frame with the crumple zone (Szkielet, 2017)

Fig. 2. An example of a buggy vehicle (Jurczak, 2017)

Many research works introduce the problem of various energy-absorbing solutions, which aims to preserve the highest level of energy absorption because of their properties during crushing (Alavi and Khodabakhsh, 2015). Different energy-absorbing solutions by using specific cross-sectional shapes, the thickness of their walls or the incorporation of specific ‘triggers’ can directly influence the level of energy absorbed because of crush generated during a collision (Ferdynus et al., 2018). The work presents the subject of the numerical analysis of dynamic impact of the

DOI 10.2478/ama-2019-0010

buggy-type vehicle frame in the scope of passive safety (Guangjun et al., 2017). Owing to the specifics of the design of this type of vehicle, the frame is the main construction element that has main impact (Sun et al., 2018) on the safety level in the event of an impact (Gui et al., 2018). Buggy cars were designed and served initially to drive through dunes on the beaches and deserts. Over time, they were also adapted for recreational and off-road riding. Their characteristic feature is the open body, sturdy suspension and exposed engine located in the rear of the vehicle. Figure 2 shows the graphical representation of a typical buggy vehicle.

2. SUBJECT OF THE STUDY

The subject of the study was the construction of welded buggy frame. The geometric model was designed in Inventor CAD software and then imported to Abaqus 6.14 CAE software (Rozylo, 2016). The material model of the aluminium alloy 6061 used for the designed frame was based on the use of plastic–elastic features with bilinear characteristics, which were obtained from the Inventor materials' database. Details of the material data for aluminium alloy are given in Table 1.

Tab. 1. Material properties for aluminium alloy 6061

	Unit	Numerical value
Young's module	MPa	70,000
Poisson's ratio	-	0.33
Yield point	MPa	175
Tensile strength	MPa	250
Elongation at break	%	8
Density	kg/m^3	2,700

The geometry of the frame includes thin-walled profiles with circular and square cross sections with a 3-mm wall thickness as well as thin-walled square cross-sectional profiles (Deng et al., 2018) with a wall thickness of 1.5 mm included in the front crumple zone. Figure 3 shows the graphical representation of the frame model.

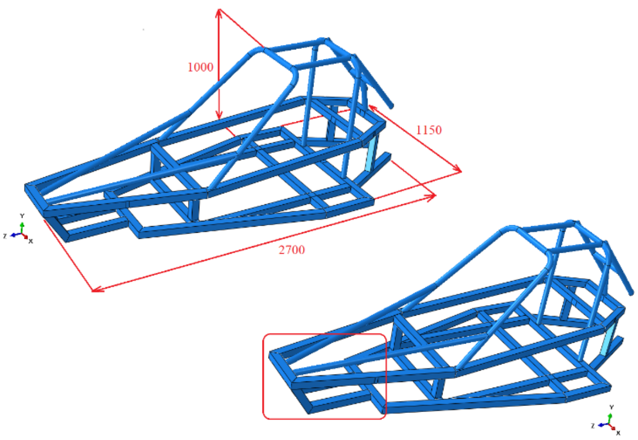

Fig. 3. Geometrical parameters of the model and crumple zone

With reference to the frame structure, Fig. 4 shows the area of the structure with base thickness and the crumple zone with reduced thickness.

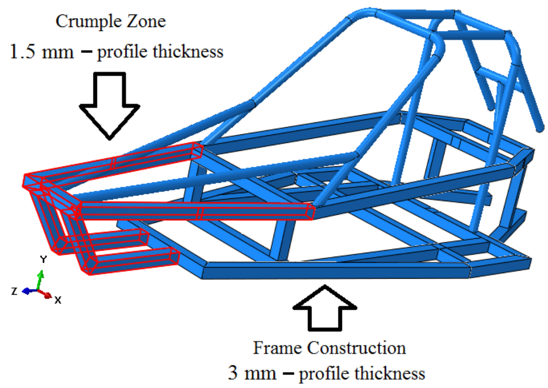

Fig. 4. Frame construction detailing areas

It was assumed that the designed frame was welded, thus importing the frame model from Inventor to Abaqus enabled the import of the entire structure as a single geometric model.

3. RESEARCH METHODOLOGY

Numerical analysis was based on the finite element method carried out as a dynamic issue (Ferdynus et al., 2018). The study investigated the way in which the energy was absorbed by the structure, with particular emphasis on the behaviour of the crumple zone. Additional attempts were made to identify the most sensitive areas that could adversely affect the driver's safety. The study investigated reaction forces, velocities, displacements, overloads and stresses in the dynamic impact to a rigid non-deformable wall (Lonkwic et al. 2015). Within the numerical analysis, a material model was defined based on the properties presented in Table 1. The impact process was defined based on the known parameters: the initial frame velocity of 50 km/h (about 14 m/s) and the potential duration of the impact process of 0.045 s. The distance travelled by the frame during the impact was calculated using equation (1):

$$s = v * t \tag{1}$$

where s is the distance, v is the velocity and t is the time.

The potential distance that was designated as part of the impact process was approximately 625 mm. The obtained value represents about 23% of the global frame length. This value, however, is not a parameter indicating the true depth of the structure into the rigid wall due to impact simulation – because of the inherent structural rigidity, material density and thickness, additional loads simulating engine load and driver mass. An important factor directly influencing the reduction of frame structure's length because of impact is the energy absorption and buckling mode (occurrence of local or global buckling) of the structure. Boundary conditions were set out as part of this work, which were connected with the complete restraint of a rigid plate (wall) and defining the frame structure's initial velocity of movement towards the plate. The frame structure additionally had determined concentrated masses, bound with a coupling type tie with proper frame surfaces, in order to simulate the load resulting from the engine's and person's own mass (round tags) – as shown in Fig. 5. In addition, a measuring point (triangular tag) was generated so as to collect the results for velocity and movement of the system.

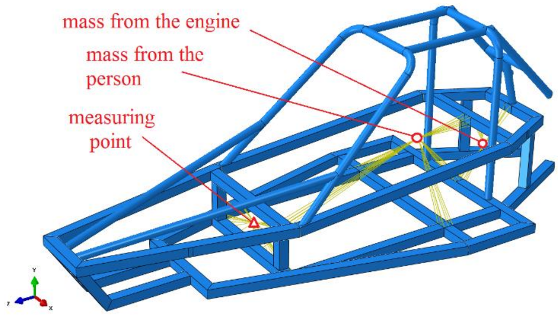

Fig. 5. The frame structure with the included loads from the engine and the person together with the presented measuring point

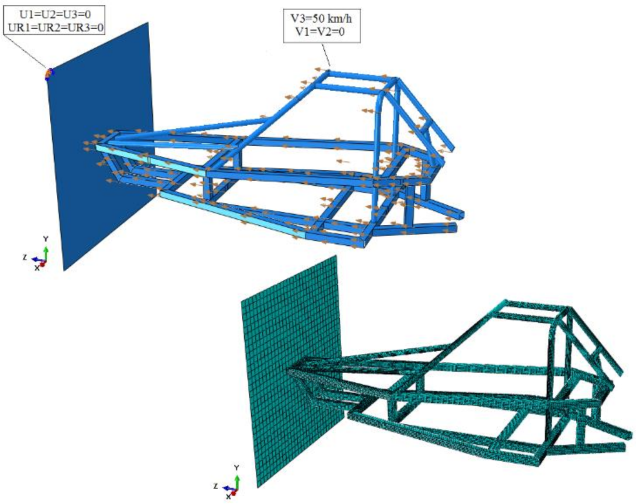

Fig. 6. Boundary conditions and discrete model

The boundary conditions referring to the complete restraint of the plate simulating a rigid wall were set out through the blocked possibility of movement and rotation of the plate in any direction. In the edge of the plate, a reference point was set out, closely connected to the entire geometry of the shell element in which all degrees of freedom were successively locked. In the case of the frame structure, a boundary condition was implemented to define the initial velocity parameter aimed towards the non-deformable plate. This way, the boundary conditions were described, which made possible the further simulation of the dynamic impact process with the inclusion of the possibility of reflection of the frame from the plate, as an effect of the structure's inertia. The discretisation process of the numerical model was conducted based on the use of shell-type elements (Wysmulski and Debski, 2017). The numerical model was described using a type S8R finite element mesh with the square shape function, constituting finite elements with 6 degrees of freedom in each of the 8 nodes for one element (Rusiński, 2000). The total number of finite elements describing the model is 140,000, whereas for the nodes, it is 91,500. The plate was modelled as a non-deformable object and the frame structure as deformable (Zienkiewicz, 2000). Figure 6 shows the boundary conditions and discrete model.

4. RESULTS

The testing results presented in the scope of passive safety were derived based on the conducted numerical analysis. As a part of the FEM analysis (Rozylo et al., 2018), a reaction value was initially evaluated, which was generated in the rigid plate hit by the frame structure. Figure 7 shows the characteristics of reaction force versus time.

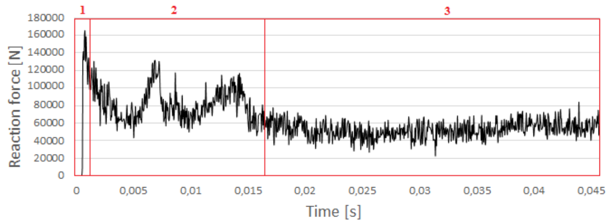

Fig. 7. The characteristic of the reaction force versus time

As a part of the obtained characteristic of the reaction force, in relation to the time of the analysis duration, it was observed that the work of the structure is divided into a number of stages. Contact interactions (in tangential and normal directions, with a friction coefficient of 0.15) were defined between the column ends and the rigid plate supports in tangential and normal directions (Ferdynus, 2013). Applied contact relations allow correct simulation of the crash test. Changing the friction coefficient has a negligible effect on the work of construction. Initially observed was the stage in which the maximum reaction value occurred as a part of the contact of the striking object with the rigid plate. The maximum reaction value is 165,180 N. The second stage is connected with the influence of the crumple zone. Specific reaction spikes occurred as a part of the second stage because of the 'folding' of the front crumple zone. The third stage is connected with the stabilisation of the reaction level (force range: 4,000–6,000 N). Fig. 8 shows the dynamic impact process.

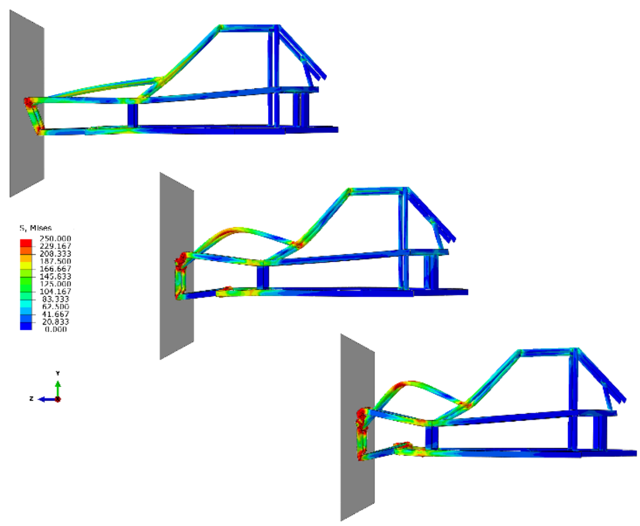

Fig. 8. The frame damage in 0.0045 s, 0.0225 s and 0.045 s

The test results point to the occurrence of a high level of structure deformation in the area of the crumple zone. Regarding the dynamic (explicit) analysis, strain-rate sensitivity (SRS) parameter is very important. SRS is a parameter that characterised deformation mechanism of materials. The definition of this parameter is mainly based on incremental changes in strain rate during dynamic tests (performed at fixed temperature and microstructure to determine adequate changes in flow stress), which are commonly called as strain hardening. Strain hardening is the strengthening

DOI 10.2478/ama-2019-0010

of a metal or polymer by plastic deformation. Incremental tests for SRS minimise the effects of changes in structure, temperature and strain hardening during testing and are used to determine the relationship between dislocation velocity and stress at constant structure. In case of metals, the Johnson-Cook model of material is often used. The Johnson-Cook model even includes strain-rate sensitive failure criteria that allow to obtain advanced numerical results in dynamic analysis.

In addition, the velocity in the measuring point, previously shown in Figure 5, was presented as a part of the testing results. Figure 9 shows the characteristic of the velocity and displacement in the time of the analysis duration.

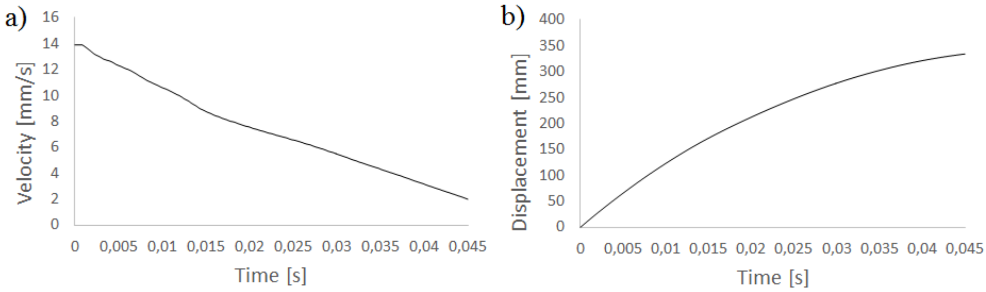

Fig. 9. Operation characteristics: (a) velocity and (b) displacement

It was observed that the velocity was reduced in an almost linear manner to the end of the time of the analysis duration, where, from the initial value of 14 m/s, it has achieved 2 m/s within 0.045 s. For the structure to brake completely, it was necessary to increase the numerical analysis time; however, it would entail a significant increase in the numerical calculation duration time. The movement of the frame structure (shortening of the crumple zone), which was observed in the measuring point, reached the value of 335 mm, which constitutes barely 12.5% of the entire structure length. The area of the shortening relates mainly to the area of the crumple zone, which has no negative effect on endangering the safety of the person driving the vehicle. The parameter that points directly to the possible occurrence of the negative effect on health and even life of the person is the overload. The parameter is known as a state of the body subjected to external forces and the resultant of which creates an acceleration different from that resulting from the gravitational force *g*. The overload is a multiple of the standard acceleration of gravity. The overload level of *5g* can be a deadly value for the human in many cases, however, only in the case of a few seconds of lasting of the effect. Nevertheless, in the case where a very high level of overload occurs, it is desirable that time of this effect is as short as possible. The overload characteristic versus time is presented in Fig. 10.

Because of the obtained overload result, it is possible to directly state that the obtained overload range, beginning with the initial moment up to 0.045 s, does not constitute a direct threat to human life. The overload factor should be as low as possible, because of its negative effect on the human body during a long period of overload. Only the initial stage in which the overload level reaches *60g* may negatively affect a human, which, however, is the value from the area of moderate injuries. In the first stage of impact, the value of the overload factor is high, whereas in the second half of the analysis, the value decreases three times. The remaining range of overloads until the end of the time of the analysis duration shows the work of the test system within the range allowed for maintaining the permissible safe level. The analysis of the designed frame shows that the thickness of the frame structure should be reduced (from the pre-assumed thickness of 1.5 mm of crumple zone and 3 mm of rest of the frame, as shown in Fig. 4), in order to reduce the level of overload. Constructions should usually be designed so that the initial overload 'peak' was the smallest as possible and the remaining range of the overload characteristics does not exceed a few *g*, as human-safety values.

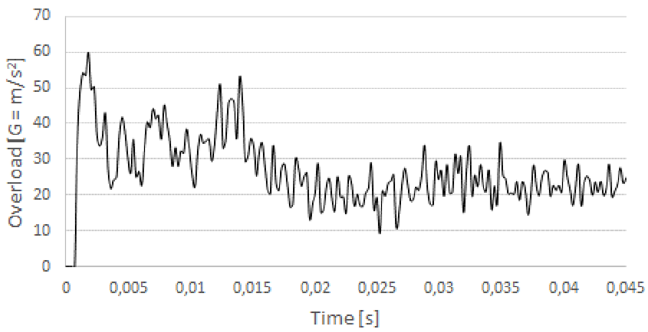

Fig. 10. The overload characteristic versus time

5. CONCLUSION

On the basis of the conducted simulation tests, a new contribution to the development of the described subject is presented, which is the analysis of not only the crumple zone but also the complete frame of the vehicle. A lot of scientific publications present only crumple zones or energy-absorbing elements. The author's contribution includes the analysis of the structure, using the example of a vehicle frame, taking into account both the crumple zone and the rest of the structure.

The aim of this work was the dynamic analysis of the buggy-type vehicle rack frame for the purpose of crash testing. After analysing the gathered results, conclusions regarding the safety of this type of construction were drawn. On the basis of the developed reaction, time characteristic, a multi-stage structure work was observed, beginning with the initial capture of the maximum value, through the work of the controlled crumple zone, ending with the stabilisation of the reaction. In the impact process, it was observed that the main work of the frame, with regard to the energy absorption, is performed by the front crumple zone. The designated velocity and movement values in the measuring point were located right behind the crumple zone point to the correctness of the structure work. The shortening of the structure that equalled

335 mm in the crumple zone does not constitute an immediate danger to human safety. The level of the overload equalling *60g* in the initial moment and from 0.015 to 0.045 s, where the overload range is about *20–30g*, does not constitute danger to human life, because of the occurrence of the dominating part of the range in the permissible area.

REFERENCES

1. **Alavi A., Khodabakhsh H.** (2015), The effect of radial distance of concentric thin-walled tubes on their energy absorption capability under axial dynamic and quasi-static loading, *Thin-Walled Structures*, 93, 188-197.
2. **Autokult** (2014), Retrieved from http://autokult.pl/1954,testy-zderzeniowe-co-jest-badane.
3. **Bolton W.** (1982), *Outline of physics*, „in Polish", PWN.
4. **Deng X., Liu W., Lin Z.** (2018), Experimental and theoretical study on crashworthiness of star-shaped tubes under axial compression, *Thin-Walled Structures*, 130, 321–331.
5. **Ferdynus M.** (2013), An energy absorber in the form of a thin-walled column with square cross-section and dimples, *Eksploatacja i Niezawodnosc – Maintenance and Reliability*, 15 (3), 253–258.
6. **Ferdynus M., Kotelko M., Kral J.** (2018), Energy absorption capability numerical analysis of thin-walled prismatic tubes with corner dents under axial impact, *Eksploatacja i Niezawodnosc – Maintenance and Reliability*, 20, 252-259.
7. **Guangjun G., Weiyuan G., Jian L., Haipeng D., Xiang Z., Wei C.** (2017), Experimental investigation of an active–passive integration energy absorber for railway vehicles, *Thin-Walled Structures*, 117, 89-97.
8. **Gui C., Bai J., Zuo W.** (2018), Simplified crashworthiness method of automotive frame for conceptual design, *Thin-Walled Structures*, 131, 324–335.
9. **Jurczak D.** (2017), Retrieved from http://jurczakautosport.pl.
10. **Lonkwic P., Rozylo P., Debski H.** (2015), Numerical and experimental analysis of the progressive gear body with the use of finite-element method, *Eksploatacja i Niezawodnosc – Maintenance and Reliability*, 17, 544-550.
11. **Milanowicz M., Budziszewski P., Kedzior K.** (2018), Numerical analysis of passive safety systems in forklift trucks, *Safety Science*, 101, 98–107.
12. **Molnar V., Fedorko G., Husakova N., Kral J., Ferdynus M.** (2016), Energy calculation model of an outgoing conveyor with application of a transfer chute with the damping plate, *Mechanical Sciences*, 7, 167-177.
13. **Rozylo P.** (2016), Optimization of I-section profile design by the finite element method, *Advances in Science and Technology - Research Journal*, 10, 52-56.
14. **Rozylo P., Debski H., Kral J.** (2018), Buckling and limit states of composite profiles with top-hat channel section subjected to axial compression, *AIP Conf Proc*, 1922, 080001.
15. **Rusiński E., Czmochowski J., Smolnicki T.** (2000), *The advanced finite elements method in load capacity structures*, "in Polish", Wrocław.
16. **Sun G., Tian J., Liu T., Yan X., Huang X.** (2018), Crashworthiness optimization of automotive parts with tailor rolled blank, *Engineering Structures*, 169, 201–215.
17. **Szkielet.** (2017), Passive Safety Official Website, Retrieved from http://www.bezpieczenstwo.strefa.pl/maps/szkiel1.jpg.
18. **Wysmulski P., Debski H.** (2017), The effect of eccentricity of load on the behavior of compressed composite columns in critical state, *Polymer Composites*, DOI https://doi.org/10.1002/pc.24601.
19. **Estrada Q., Szwedowicz D., Silva-Aceves J., Majewski T., Vergara-Vazquez J., Rodriguez-Mendez A.** (2017), Crashworthiness behavior of aluminum profiles with holes considering damage criteria and damage evolution, *International Journal of Mechanical Sciences*, 131-132, 776-791.
20. **Zienkiewicz O. C., Taylor R. L.** (2000), *Finite Element Method* (5th Edition) Volume 2 – Solid Mechanics, Elsevier.

 DOI 10.2478/ama-2019-0011

A METHOD TO DETERMINE ALLOWABLE SPEED FOR A UNIT LOAD IN A PALLET FLOW RACK

Eugene SAFRONOV,* Andrey NOSKO*

*Bauman Moscow State Technical University, Faculty of Robotics and Complex Automation, Department of Lifting and Transport Systems, 105005, Moscow, 2-ya Baumanskaya 5/1, Russian Federation

gen-s@mail.ru, dr.nosko@mail.ru

received 4 January 2019, revised 26 April 2019, accepted 30 April 2019

Abstract: Pallet flow rack are widely used in intralogistics to maximize warehouse capacity and to reduce the travel by fork-lifts. However, the use of pallet flow racks is associated with increased danger due to the use of gravity conveyors in their design. For this purpose, the gravity conveyors of pallet flow rack have a two safety elements – brake rollers and a stopping mechanism with pallet separator, which are working as a system. Brake rollers limit the speed of pallets, while the stopping mechanism allows exuding a pressure on the unloading pallet from the following behind it. A pallet should have such a speed, controlled by the brake rollers, so that it could be stopped by a stopping mechanism without damaging it. Based on the Cox impact theory, an original method for determining the allowable speed of a pallet in a pallet flow rack is proposed. The method ensures safe operation of the stopping mechanism with pallet separator and takes into account the mechanical properties and design parameters of the pallet separator stopper. A calculation example is provided for the most commonly used types of pallets – Euro pallet (1200 mm × 800 mm) and Industrial pallet (1200 mm × 1000 mm). The obtained results agree well with the pallet speed range of 0.2 to 0.3 m/s recommended by the manufacturers of pallet flow racks.

Key words: Gravity roller conveyor, pallet flow rack, dynamic pallet rack, pallet speed

1. INTRODUCTION

Reducing the cost of warehouse operations is one of the main tasks in the designing of warehouses and the selection of material handling equipment and storage systems. Solutions of this task can be found by optimizing space utilization (e.g., Derhami et al., 2017), reducing the total travelled distance by the fork-lifts (Ghalehkhondabi and Masel, 2018), using automated storage and retrieval systems (AS/RSs), autonomous vehicle storage and retrieval systems (AVS/RSs) (Heragu et al., 2011) and Shuttle-Based Storage and Retrieval Systems (SBS/Rs) (Lerher et al., 2017) for increasing the throughput of warehouse operations.

Optimizing space utilization of a warehouse and maximising warehouse capacity, also reducing the travel by fork-lifts, can be achieved with block storage or deep-lane storage systems (Sulirova et al., 2017; Boysen et al., 2018; Boywitz and Boysen, 2018). One of such systems is pallet flow rack (Fig. 1) (Accorsi et al., 2017 and Eo et al., 2015).

The construction of a pallet flow rack can be divided into two parts — static and dynamic. The static part includes standard racking elements, which provide stability in each direction as well as support for dynamic elements. The dynamic part includes a gravity roller conveyor and safety elements, such as brake rollers and a stopping mechanism with pallet separator (Vujanac et al., 2016) (Fig. 2). Pallets are the most common form of unit loads in warehouses. There are various types of pallets, of which Euro pallet (1200 mm × 800 mm) and Industrial pallet (1200 mm × 1000 mm) are widely used in the EU as well as in other countries (Rushton et al., 2010). The maximum pallet weight during transportation is determined experimentally for each type of product. The safe operation load is limited to 1250 kg (EPAL Euro Pallet).

As noted by Wu S et al. (2016), pallet flow racks save 22–25% of travelled distance by fork-lifts in comparison with single-deep racks. Therefore, pallet flow racks are widely using in automated warehouses with AS/RSs machines (Metahri and Hachemi, 2017; Ghomri and Sari, 2017; Hamzaoui and Sari, 2015), automated compact cross-dock system (Zaerpour et al., 2015) and with Just-In-Time production system (Halim et al., 2012).

However, the use of pallet flow racks is associated with increased danger due to the use of gravity conveyors in their design. At the same time, studies of the static part are widely reflected in the literature (e.g., Thombare et al., 2016; Talebian et al., 2018; Crisan et al., 2012; Saleh et al., 2018), in contrast to the safety elements of pallet flow racks – brake rollers and a stopping mechanism with pallet separator (Vujanac et al., 2016).

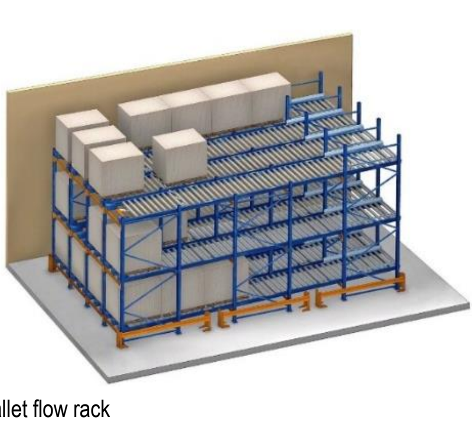

Fig. 1. Pallet flow rack

DOI 10.2478/ama-2019-0011 acta mechanica et automatica, vol.13 no.2 (2019)

As is known, human factor is one of the main causes of accidents on a production (Aleksandrov et al., 2016), and utilization of stopping mechanism with pallet separator allows to reduce the requirements for the fork-lift drivers working with pallet flow racks due to the exclusion of pressure on the unloading pallet from the following behind it.

A pallet should have such a speed so that it could be stopped by a stopping mechanism without damaging it. This condition is achieved by the utilization of brake rollers (Nosko et al, 2018).

a)

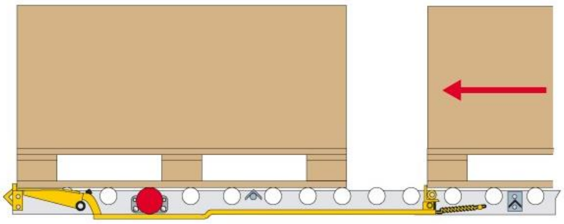

b)

Fig. 2. Safety elements of a pallet flow rack: a) brake roller; b) stopping mechanism with pallet separator

In addition, in gravity roller conveyors as well as in pallet flow racks using such conveyors, it is usually required to limit the speed of unit loads (Kulwiec, 1985). This requirement is pointed in some national standards of safety, for example, POT R M-029-2003 in Russia.

In practice, manufacturers recommend safe transportation speed to be in the range of 0.2 to 0.3 m/s. However, it was not possible to find methods for determining this speed.

The purpose of this study is to develop a method for calculating the allowable speed for pallets of different masses in a gravity rack.

2. ALLOWABLE LOAD ON THE STOPPER

When the pallet is transported by the gravity roller conveyor, it hits the stopper of stopping mechanism with pallet separator (hereinafter the 'stopper') from the side of the discharge.

In more than 90% of cases, a pallet is oriented along the gravity roller conveyor. Thereby, the impact of the pallet sump against a stopper occurs at the three lug faces, as shown in Fig. 3.

Review of patent and bibliographic sources including catalogues of such companies like Interroll, Damon Group, Rack & Roll, Mecalux and Euroroll showed that the most often used construction of the stopper represents a square or round cross-section tube with a welded plate. Such a stopper is schematically shown in Fig. 4.

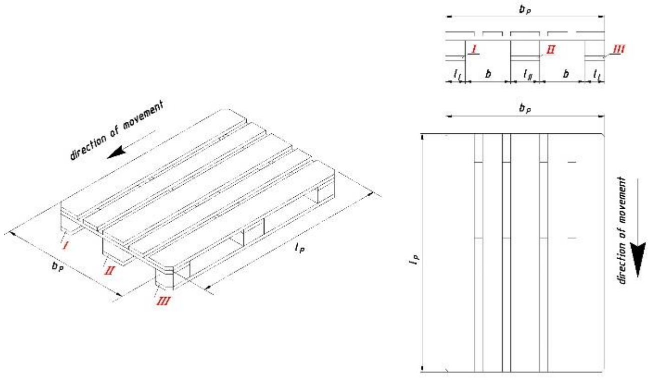

Fig. 3. Parameters of a pallet

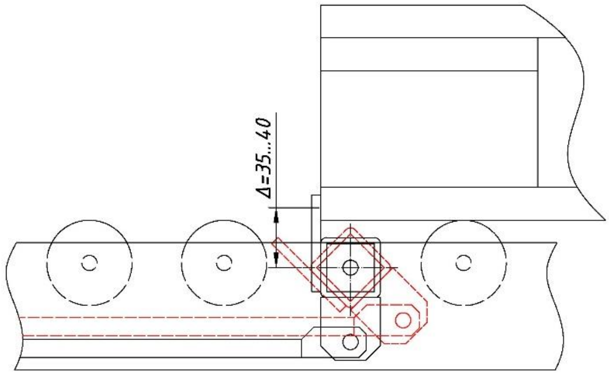

Fig. 4. Cross-section of the stopper

In the process of stopping the pallet, an off-centre impact occurs, resulting in bending and torsional deformations of the stopper. The schematic of the loading and the distributions of the bending moment and torque in the stopper is shown in Fig. 5. Because of the symmetry, a half of the stopper can be considered, for example, the sections 1–4. The geometric parameters of the stopper are presented in Table 1.

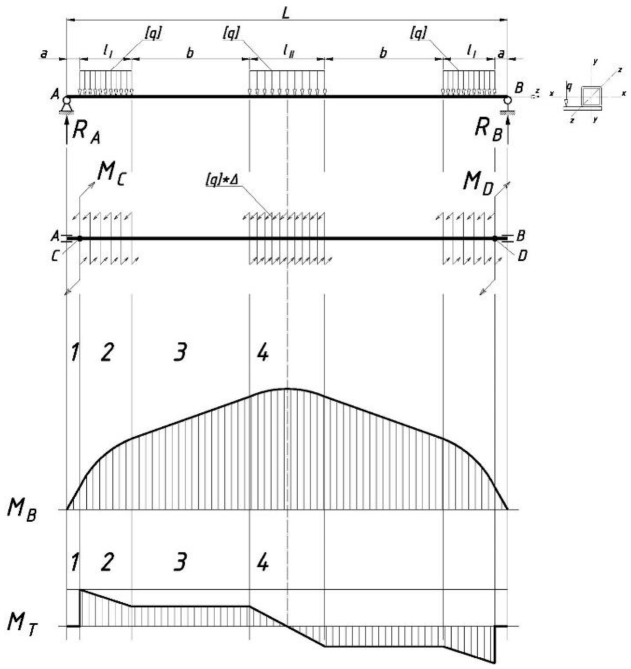

Fig. 5. Distributions of the bending moment and torque in the stopper

DOI 10.2478/ama-2019-0011

Tab. 1. Geometric parameters of the stopper

Type of pallet	*L*, mm	*a*, mm	*l*I, mm	*b*, mm	*l*II, mm	Δ, mm
Euro pallet	880	40	100	227.5	145	35–40
Industrial pallet	1100	50	145	282.5	145	

According to Fig. 5, the bending moment M_{iB} for the *i*-th section of the stopper can be calculated as follows:

$$\begin{cases} M_{1B}(z) = R_A \cdot z = q\left(l_I + \frac{l_{II}}{2}\right)z, 0 \le z \le a \\ M_{2B}(z) = \left(l_I + \frac{l_{II}}{2} - \frac{z}{2}\right)qz + M_{1B}^{z=a}, 0 \le z \le l_I \\ M_{1B}^{z=a} = q\left(l_I + \frac{l_{II}}{2}\right)a \\ M_{3B}(z) = \frac{l_{II}}{2}qz + M_{2B}^{z=l_1}, 0 \le z \le b \\ M_{2B}^{z=l_I} = \left(\frac{l_{II}}{2} + \frac{l_I}{2}\right)ql_I + q\left(l_I + \frac{l_{II}}{2}\right)\cdot a \\ M_{4B}(z) = (l_{II} - z)\frac{qz}{2} + M_{3B}^{z=b}, 0 \le z \le \frac{l_{II}}{2} \\ M_{3B}^{z=b} = \frac{l_{II}}{2}qb + \left(\frac{l_{II}}{2} + \frac{l_I}{2}\right)ql_I + q\left(l_I + \frac{l_{II}}{2}\right)\cdot a \\ M_{B\_MAX} = M_{4B}^{z={l_{II}}/{2}} = \frac{ql_{II}^2}{4} + M_{3B}^{z=b} \end{cases} \quad (1)$$

where: M_{iB} is the bending moment for the *i*-th section; z is the axial coordinate; M_{B_MAX} is the maximum bending moment; q is the distributed load.

We represent the bending moments in matrix form as:

$$\begin{pmatrix} M_{1B}(z) \\ M_{2B}(z) \\ M_{3B}(z) \\ M_{4B}(z) \end{pmatrix} = q \cdot \begin{pmatrix} A_{1B} & B_{1B} & C_{1B} \\ A_{2B} & B_{2B} & C_{2B} \\ A_{3B} & B_{3B} & C_{3B} \\ A_{4B} & B_{4B} & C_{4B} \end{pmatrix} \cdot \begin{pmatrix} z^2 \\ z \\ 1 \end{pmatrix} \quad (2)$$

where: A_{iB}, B_{iB}, C_{iB} are constant coefficients. Taking account of Eq. (1) and Eq. (2), these coefficients are calculated as:

$$\begin{pmatrix} A_{1B} & B_{1B} & C_{1B} \\ A_{2B} & B_{2B} & C_{2B} \\ A_{3B} & B_{3B} & C_{3B} \\ A_{4B} & B_{4B} & C_{4B} \end{pmatrix} = \begin{pmatrix} 0 & l_I + 0.5l_{II} & 0 \\ -0.5 & l_I + 0.5l_{II} & \left(l_I + \frac{l_{II}}{2}\right)a \\ 0 & 0.5l_{II} & (l_I + 0.5l_{II})(l_I + a) - 0.5l_I^2 \\ -0.5 & 0.5l_{II} & (l_I + 0.5l_{II})(l_I + a) - 0.5l_I^2 + 0.5bl_{II} \end{pmatrix} \quad (3)$$

According to Fig. 5, the torque M_{iT} for the *i*-th section of the stopper can be calculated as follows:

$$\begin{cases} M_{1T}(z) = 0, 0 \le z \le a \\ M_{2T}(z) = \left(l_I + {l_{II}}/{2} - z\right)\cdot q \cdot \Delta, 0 \le z \le l_I \\ M_{3T}(z) = M_{2T}^{z=l_I}, 0 \le z \le b \\ M_{2T}^{z=l_I} = {l_{II}}/{2} \cdot q \cdot \Delta \\ M_{4T}(z) = M_{3T}^{z=b} - z \cdot q \cdot \Delta, 0 \le z \le \frac{l_{II}}{2} \\ M_{3T}^{z=b} = {l_{II}}/{2} \cdot q \cdot \Delta, \end{cases} \quad (4)$$

where: M_{iT} is the torque for the *i*-th section; z is the axial coordinate; M_{B_MAX} is the maximum bending moment; q is the distributed load, Δ is the moment arm (see Fig. 5 and Table 1).

We represent the torque in matrix form as:

$$\begin{pmatrix} M_{1T}(z) \\ M_{2T}(z) \\ M_{3T}(z) \\ M_{4T}(z) \end{pmatrix} = q\Delta \begin{pmatrix} B_{1T} & C_{1T} \\ B_{2T} & C_{2T} \\ B_{3T} & C_{3T} \\ B_{4T} & C_{4T} \end{pmatrix} \begin{pmatrix} z \\ 1 \end{pmatrix} \quad (5)$$

where: B_{iT}, C_{iT} are constant coefficients. Taking account of Eq. (4) and Eq. (5), these coefficients are calculated as:

$$\begin{pmatrix} B_{1T} & C_{1T} \\ B_{2T} & C_{2T} \\ B_{3T} & C_{3T} \\ B_{4T} & C_{4T} \end{pmatrix} = \begin{pmatrix} 0 & 0 \\ -1 & l_I + {l_{II}}/{2} \\ 0 & {l_{II}}/{2} \\ -1 & {l_{II}}/{2} \end{pmatrix} \quad (6)$$

According to Fig. 5, dangerous section of the stopper is third section with z = b or:

$$\begin{cases} M_{3B}^{z=b} = \frac{l_{II}}{2}qb + \left(\frac{l_{II}}{2} + \frac{l_I}{2}\right)ql_I + q\left(l_I + \frac{l_{II}}{2}\right)\cdot a \\ M_{3T}^{z=b} = {l_{II}}/{2} \cdot q \cdot \Delta \end{cases}. \quad (7)$$

We represent bending moment and torque in the dangerous section of the stopper as:

$$\begin{cases} M_B = M_{3B}^{z=b} = K_B \cdot q \\ M_T = M_{3T}^{z=b} = K_T \cdot q' \end{cases} \quad (8)$$

where: K_B – coefficien of bending moment, K_T – torque coefficient.

The coefficients K_B and K_T are calculated with account of the data of Tab. 1.

Tab. 2 presents the values of K_B, M_B, K_T and M_T obtained using Eq. (7) and Eq. (8) for different pallet sizes.

Tab. 2. The values of coefficients K_B and K_T and expressions for calculating the maximum values of the bending moment and torque

Type of pallet	K_B, m²	M_B, Nm	K_T, m²	M_T, Nm
Euro pallet	0.0356	$0.0356\ q$	0.0029	$0.0029\ q$
Industrial pallet	0.035	$0.035\ q$	0.002	$0.002\ q$

Concerning the Mises yield criterion, the maximum allowable stress of the stopper is calculated (Jones R., 2009) as follows:

$$[\sigma] = \sqrt{\left(\frac{M_B \cdot Y_{MAX}}{I_X}\right)^2 + 3\left(\frac{M_T \cdot R_{MAX}}{I_T}\right)^2} \quad (9)$$

where: I_X – the second moment of area about the neutral axis *X*, Y_{MAX} – the maximum perpendicular distance to the neutral axis *X*, I_T – torsional constant of the cross-sectional shape of the stopper, R_{MAX} – the maximum distance from the axis of torsion to the point of section with maximum torsional stress.

Taking into account Eq. (8) and Eq. (9), the allowable distributed load $[q]$ is calculated as below:

$$[q]=\frac{[\sigma]}{\sqrt{\left(\frac{K_B\cdot Y_{MAX}}{I_X}\right)^2+3\left(\frac{K_T\cdot R_{MAX}}{I_T}\right)^2}} \tag{10}$$

3. STRAIN ENERGY OF THE STOPPER

According to Fig. 5, the strain energy of the stopper is determined by the sum of independent works of the two factors: bending moment and torque, and calculated as (Nash, 1998):

$$U=\frac{1}{2}\int_l\left(\frac{M_T^2}{G\cdot I_T}+\frac{M_B^2}{E\cdot I_X}\right)dz \tag{11}$$

where: G – modulus of elasticity in shear, E – the Young's modulus.

Taking into account Eq. (1), Eq. (2) and Eq. (11), and because of the symmetry, strain energy from work of bending moment for *i*-th section is found using the formula:

$$(U_B)_i=\frac{1}{2}\int_l\frac{2\cdot M_{iB}^2}{E\cdot I_X}dz=q^2\cdot\int_l\frac{\left(A_{iB}\cdot z^2+B_{iB}\cdot z+C_{iB}\right)_i^2}{E\cdot I_X}dz$$

Or in more convenient form as:

$$(U_B)_i=\frac{q^2}{E\cdot I_X}\cdot\left(K_{1iB}\cdot z_i+K_{2iB}\cdot z_i^2+K_{3iB}\cdot z_i^3+K_{4iB}\cdot z_i^4+K_{5iB}\cdot z_i^5\right) \tag{12}$$

where: K_{jiB} are constant coefficients for bending moment (*j* – exponent, *i* – number of section), which are calculated as:

$$\begin{cases} K_{1iB}=C_{iB}^2\\ K_{2iB}=2\cdot B_{iB}\cdot C_{iB}\\ K_{3iB}=\frac{B_{iB}^2+2\cdot A_{iB}\cdot C_{iB}}{3}\\ K_{4iB}=\frac{A_{iB}\cdot B_{iB}}{2}\\ K_{5iB}=\frac{A_{iB}^2}{5}\end{cases} \tag{13}$$

where: A_{iB}, B_{iB}, C_{iB} are constant coefficients, calculated with Eq. (3).

According Eq. (11) and Eq. (12) and Fig. 5, strain energy from the work of bending moments equals as sum of $(U_B)_i$:

$$U_B=\sum_{i=1}^4(U_B)_i=\frac{q^2}{E\cdot I_X}\cdot\sum_{i=1}^4\left(K_{1iB}\cdot z_i+K_{2iB}\cdot z_i^2+K_{3iB}\cdot z_i^3+K_{4iB}\cdot z_i^4+K_{5iB}\cdot z_i^5\right)=K_{U\_B}\cdot\frac{q^2}{E\cdot I_X} \tag{14}$$

where: K_{U_B} is a constant coefficient.

Strain energy for the *i*-th section from the work of torque accounts to Eq. (4), Eq. (5) and Eq. (11) because of the symmetry can be calculated as:

$$(U_T)_i=\frac{1}{2}\int_l\frac{2\cdot M_{iT}^2}{G\cdot I_T}dz=q^2\Delta^2\cdot\int_l\frac{(B_{iT}\cdot z+C_{iT})_i^2}{G\cdot I_T}dz$$

Or in more convenient form as:

$$(U_T)_i=\frac{q^2\Delta^2}{G\cdot I_T}\cdot(K_{1iT}\cdot z_i+K_{2iT}\cdot z_i^2+K_{3iT}\cdot z_i^3) \tag{15}$$

where: K_{jiT} are constant coefficients for torque (*j* – exponent, *i* – number of section), which are calculated as:

$$\begin{cases} K_{1iT}=C_{iT}^2\\ K_{2iT}=2\cdot B_{iT}\cdot C_{iT}\\ K_{3iT}=\frac{B_{iT}^2}{3}\end{cases} \tag{16}$$

where: B_{iT}, C_{iT} are constant coefficients, calculated with Eq. (6).

According Eq. (11) and Eq. (15) and Fig. 5, strain energy from the work of torque equals as sum of $(U_T)_i$:

$$U_T=\sum_{i=1}^4(U_T)_i=\frac{q^2\Delta^2}{G\cdot I_T}\cdot\sum_{i=1}^4(K_{1iT}\cdot z_i+K_{2iT}\cdot z_i^2+K_{3iT}\cdot z_i^3)=K_{U\_T}\cdot\frac{q^2}{G\cdot I_T} \tag{17}$$

where: K_{U_T} is a constant coefficient.

The coefficients K_{U_B} and K_{U_T} are calculated with account of the data of Tab. 1 and Tab. 2.

Tab. 3 presents the values of K_{U_B}, U_B, K_{U_T} and U_T obtained using Eq. (14) and Eq. (17) for different pallet sizes.

Tab. 3. The values of coefficients K_{U_B} and K_{U_T} and expressions for calculating the values of strain energy from the works of bending moments and torque

Type of pallet	K_{U_B}, m⁵	U_B, J	K_{U_T}, m⁵	U_T, J
Euro pallet	$3\cdot10^{-4}$	$\frac{3\cdot10^{-4}q^2}{E\cdot I_X}$	$4.7\cdot10^{-6}$	$\frac{4.7\cdot10^{-6}q^2}{G\cdot I_T}$
Industrial pallet	$3.3\cdot10^{-4}$	$\frac{3.3\cdot10^{-4}q}{E\cdot I_X}$	$3.2\cdot10^{-6}$	$\frac{3.2\cdot10^{-6}q^2}{G\cdot I_T}$

According to Eq. (11), Eq. (14) and Eq. (17), the strain energy of the stopper equals as:

$$U=q^2\cdot\left(\frac{K_{U\_B}}{E\cdot I_X}+\frac{K_{U\_T}}{G\cdot I_T}\right)$$

Therefore, allowable stain energy of the stopper is found as:

$$[U]=[q]^2\cdot\left(\frac{K_{U\_B}}{E\cdot I_X}+\frac{K_{U\_T}}{G\cdot I_T}\right)$$

where: $[q]$ is allowable distributed load.

Taking into account Eq. (10), $[U]$ is calculated as:

$$[U]=[\sigma]^2\cdot\frac{\left(\frac{K_{U\_B}}{E\cdot I_X}+\frac{K_{U\_T}}{G\cdot I_T}\right)}{\left(\frac{K_B\cdot Y_{MAX}}{I_X}\right)^2+3\left(\frac{K_T\cdot R_{MAX}}{I_T}\right)^2} \tag{18}$$

4. ALLOWABLE PALLET SPEED

Assuming the pallet as an absolutely rigid body, the kinetic energy of the pallet during the impact is converted into the strain energy of the stopper. Weight of the pallet with the load is at least an order of magnitude greater than the mass of the stopper. Therefore, the Cox impact theory can be used in engineering calculations (Ol'shanskii V.P. and Ol'shanskii S.V., 2013), and the allowable speed of a pallet is determined by the allowable strain energy of the stopper.

Taking into account the smallness of the angle of inclination of the gravity roller conveyor in pallet flow rack (no more than 2–3 degrees), the impact can be regarded as longitudinal with a sufficient degree of accuracy. Therefore, the kinetic energy of the pallet is equal to the strain energy of the stopper:

$$\frac{M\cdot[v]^2}{2}=[U] \tag{19}$$

where: M – weight of the pallet, $[v]$ – allowable speed of the pallet.

DOI 10.2478/ama-2019-0011

According to Eq. (18) and Eq. (19), the allowable speed for pallets in the pallet flow rack is calculated as:

$$[v] = [\sigma]\sqrt{\frac{2}{M}\cdot\frac{\left(\frac{K_{U\_B}}{E\cdot I_X}+\frac{K_{U\_T}}{G\cdot I_T}\right)}{\left(\frac{K_B\cdot Y_{MAX}}{I_X}\right)^2+3\left(\frac{K_T\cdot R_{MAX}}{I_T}\right)^2}} \qquad (20)$$

5. CALCULATION EXAMPLE

For the stopper shown in Fig. 6, made of a tube 40 x 40 x 3.5 and welded to it along the entire length of the steel plate 6 mm thick, we have the following data:

$$E = 2.1\cdot 10^{11}\ Pa;\ G = 8.2\cdot 10^{10}\ Pa;\ [\sigma] = 2.2\cdot 10^{8}\ Pa$$

$$I_X = 3.02\cdot 10^{-7}\ m^4;\ I_X = 3.0\cdot 10^{-7}\ m^4;\ I_T = \\ = 1.54\cdot 10^{-7}\ m^4$$

$$y_{MAX} = 26\cdot 10^{-3}\ m;\ R_{MAX} = 20\cdot 10^{-3}\ m$$

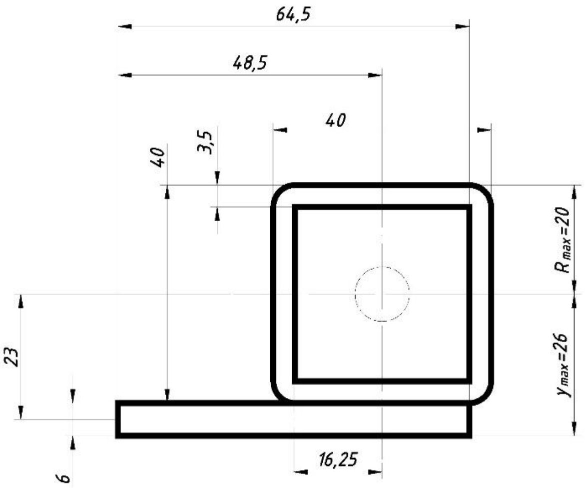

Fig. 6. Example of the stopper construction (cross-section view)

Fig. 7 presents the dependence of the allowable speed for pallets on its type and mass for the construction described above and calculated with Eq. (16).

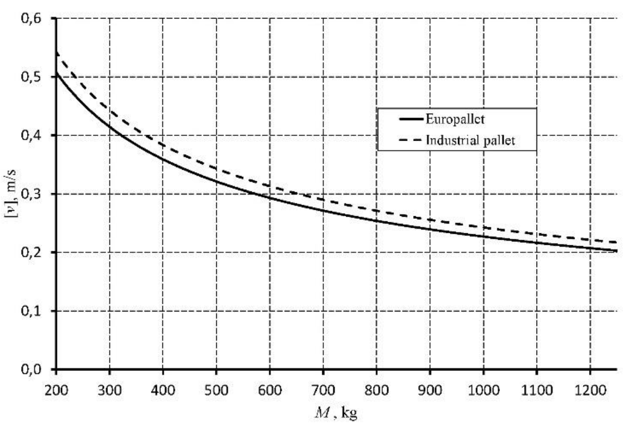

Fig. 7. Dependence of the allowable speed for pallets on its type and mass

6. CONCLUSION

1. The calculation method, based on the Cox impact theory, was developed to calculate the allowable speed for the pallets of different masses in a pallet flow rack.
2. The method takes into account the type of pallet, construction and material of the stopper.
3. Calculation examples of the allowable speed for the Euro pallet and Industrial pallet are presented for the stopper, made from square cross-section tube 40 x 40 x 3.5 mm with the welded plate of 6 mm thickness.
4. The calculated results agree well with the speed range of 0.2 to 0.3 m/s recommended by the manufacturers.

REFERENCES

1. **Accorsi, R., Baruffaldi, G., Manzini, R.** (2017), Design and manage deep lane storage system layout. An iterative decision-support model, *Int J Adv Manuf Technol*, 92(1-4), 57–67.
2. **Aleksandrov A.A., Devisilov V.A., Ivanov M.V.** (2016), A role of education system in creation of safety culture, *Chemical Engineering Transactions*, 53, 211–216.
3. **Boysen, N., Boywitz, D., Weidinger, F.** (2018), Deep-lane storage of time-critical items: one-sided versus two-sided access, *OR Spectrum*, 40(4), 1141–1170.
4. **Boywitz, D., Boysen, N.** (2018), Robust storage assignment in stack- and queue-based storage systems, *Computers & Operations Research*, 100, 189–200.
5. **Crisan, A., Ungureanu, V., Dubina, D.** (2012), Behaviour of cold-formed steel perforated sections in compression. Part 1-Experimental investigations, *Thin-walled structures*, 61, 86–96.
6. **Derhami, S., Smith, JS., Gue, KR.** (2017), Optimising space utilisation in block stacking warehouses, *Int J Of Prod Res*, 55(21), 6436–6452.
7. *Dynamic storage catalogue Damon* [available at: http://damon-group.com.au/catalogues/dynamic-storage-catalogue.pdf, access 29 March 2017].
8. **Eo, J., Sonico, J., Su, A., Wang, W., Zhou, C., Zhu, Y., Wu, S., Chokshi, T.** (2015), Structured comparison of pallet racks and gravity flow racks, *IIE Annual Conference and Expo 2015*, 1971–1980.
9. *EPAL Euro Pallet* [available at https://www.epal-pallets.org/eu-en/load-carriers/epal-euro-pallet, access 7 December, 2017]
10. *Gesamtkatalog_2012_D.pdf* [available at: http://www.euroroll.de/tl_files/Gesamtkatalog_2012_D.pdf, access 29 March 2017].
11. **Ghalehkhondabi, I., Masel, DT.** (2018), Storage allocation in a warehouse based on the forklifts fleet availability, *Journal Of Algorithms & Computational Technology*, 12(2), 127–135.
12. **Ghomri, L., Sari, Z.** (2017), Mathematical modeling of the average retrieval time for flow-rack automated storage and retrieval systems, Journal Of Manufacturing Systems, 44, 165–178.
13. **Halim, N.H.A., Jaffar, A., Yusoff, N., Adnan, A.N.** (2012), Gravity Flow Rack's material handling system for Just-in-Time (JIT) production, *2nd International Symposium on Robotics and Intelligent Sensors 2012, IRIS 2012, Procedia Engineering*, 41, 1714–1720.
14. **Hamzaoui, MA., Sari, Z.** (2015), Optimal dimensions minimizing expected travel time of a single machine flow rack AS/RS, *Mechatronics*, 31, 158–168.
15. **Heragu, SS., Cai, X., Krishnamurthy, A., Malmborg, CJ.** (2011), Analytical models for analysis of automated warehouse material handling systems, *Int J Of Prod Res*, 49(22), 6833–6861.
16. *Interroll Pallet Roller Flow PF 1100* [available at: https://www.interroll.ru/fileadmin/products/en/Resources_pdf_344683531.pdf, access 29 March 2017].

17. **Jones R.** (2009), *Deformation theory of plasticity*, Bull Ridge Publishing, USA.
18. **Kulwiec R.** (1985), *Material handling handbook*, 2nd edition, John Wiley & Sons, Inc, USA.
19. **Lerher, T., Borovinsek, M., Ficko, M., Palcic, I.** (2017), Parametric study of throughput performance in SBs/Rs based on simulation*, Int J Of Simul Model*, Vol. 16, No. 1, 96–107.
20. *Live pallet racking* [available at: https://mecaluxuk.cdnwm.com/catalogues/live-pallet-racking3.1.0.pdf#_ga=1.79741783.1709563512.1490605253, access 29 March 2017].
21. **Metahri, D., Hachemi, K.** (2017), Automated storage and retrieval systems: a performances comparison between Free-fall-flow-rack and classic flow-rack, *6-th International Conference On Systems And Control (ICSC' 17)*, Edited by: Drid, S., Mehdi D., Aitouche, A., 589–594.
22. **Nash W.** (1998), *Schaum's Outline of Theory and Problems of Strength of Materials*, 4-th edition, McGraw-Hill, USA.
23. **Nosko A.L., Safronov E.V., Soloviev V.A.** (2018), Study of Friction and Wear Characteristics of the Friction Pair of Centrifugal Brake Rollers, *Journal of Friction and Wear*, 39(2), 145–151.
24. **Ol'shanskii V.P., Ol'shanskii S.V.** (2013), Calculation of the dynamic deflection of a beam on inelastic impact by the Cox and Saint-Venant theories, *Strength of materials*, 45(3), 361–368.
25. *POT R M-029-2003 (2003)*, Mezhotraslevyye pravila po okhrane truda pri ekspluatatsiipromyshlennogo transporta (konveyyernyy, truboprovodnyy i drugiye transportnyyesredstva nepreryvnogo deystviya, Izd-vo NTS ENAS, Moscow (*in Russian*).
26. *Rollenbahnen-Trennvorrichtung* [available at: http://www.rackandroll.de/default.aspx?Pagename=Rollenbahnen_Trennvorrichtung, access 29 March 2017] (*in Deutsch*).
27. **Rushton A., Croucher P., Baker P.** (2010), *The handbook of logistics & distribution management,* 4th edition, Kogan Page Limited, London.
28. **Saleh, A., Far, H., Mok, L.** (2018), Effects of different support conditions on experimental bending strength of thin walled cold formed steel storage upright frames, *Journal of constructional steel research*, 150, 1–6.
29. **Sulirova, I., Zavodska, L., Rakyta, M., Pelantova, V.** (2017), State-of-the-art approaches to material transportation, handling and warehousing, *12th International scientific conference of young scientists on sustainable, modern and safe transport, Procedia Engineering*, 192, 857–862.
30. **Talebian, N., Gilbert, BP., Pham, CH, Chariere, R., Karampour, H.** (2018), Local and Distortional Biaxial Bending Capacities of Cold-Formed Steel Storage Rack Uprights, Proceedings of the 7th International Conference on Coupled Instabilities in Metal Structures, *JournaL Of StructuraL Engineering*, 144, No. 6.
31. **Thombare C.N., Sangle K.K., Mohitkar V.M.** (2016), Nonlinear buckling analysis of 2-D cold-formed steel simple cross-aisle storage rack frames, *Journal of Building Engineering*, 7, 12–22.
32. **Vujanac R., Miloradovic N., Vulovic S.** (2016), Dynamic storage systems, *ANNALS of Faculty Engineering Hunedoara – International Journal of Engineering*, XIV, 79–82.
33. **Wu S., Wu Ya., Wang Ya.** (2016), A structured comparison study on storage racks system, *Journal of Residuals Science & Technology*, 13(8), 2016.
34. **Zaerpour, N., Yu, YG., de Koster RBM** (2015), Storing Fresh Produce for Fast Retrieval in an Automated Compact Cross-Dock System, *Production And Operations Management*, 24(8), 1266–1284.

DOI 10.2478/ama-2019-0012

INTELLECTUALIZATION OF EMERGENCY CONTROL OF POWER SYSTEMS ON THE BASIS OF INCORPORATED ONTOLOGIES OF KNOWLEDGE-BASES

Vladimir MORKUN*, Ihor KOTOV*

*Faculty of Information Technology, Kryvyi Rih National University, Vitalii Matusevych Street, 11, Kryvyi Rih, 50027 Ukraine

morkunv@gmail.com, rioexito@gmail.com

received 13 November 2018, revised 14 May 2019, accepted 17 May 2019

Abstract: The research deals with improvement of methods and systems of controlling integrated power systems (IPSs) on the basis of intellectualization of decision-making support. Complex analysis of large-scale accidents at power facilities is performed, and their causes and damages are determined. There is substantiated topicality of building condition knowledge-bases as the foundation for developing decision-support systems in power engineering. The top priorities of the research include developing methods of building a knowledge base based on intensity models of control actions influencing the parameters of power system conditions and introducing the smart system into information contours of the automated dispatch control system (ADCS), as well as assessing practical results of the research. To achieve these goals, the authors apply methods of experiment planning, artificial intelligence, knowledge presentation, mathematical simulation, and mathematical statistics as well as methods of power systems studying. The basic research results include regression models of a power system sensitivity to control actions, methods of building a knowledge base based on the models of sensitivity matrices, a structure of the smart decision-support system, a scheme of introducing the decision-support system into the operating ADCS environment. The problem of building a knowledge base of the dispatch decision-support system on the basis of empirical data resulted from calculating experiments on the system diagram has been solved. The research specifies practical efficiency of the suggested approaches and developed models.

Key words: Power system, ontology, knowledge-base, decision-making support system, on-line dispatch control, factorial model

1. INTRODUCTION

Analysis of development and operation of the Ukrainian and foreign power systems allows deducing incremental integration, complexity and hierarchical pattern of their structure and control algorithms. Consequently, the total number of breakdowns and accidents is growing, as well as the salvage values. Ukrenergo's press service informs about the following (Avariynost v energosisteme Ukrainyi za god vyrosla vdvoye, 2015): 'The state-owned company "Ukrenergo", the operator of the integrated power system of Ukraine, is warning about possible critical situations in Ukraine's power system because of escalation of breakdowns of basic equipment in main, interstate and distributing electric grids of the country. As reported by the national power company, in 2014, the accident rate doubled as compared to that of 2013'.

The article studies a wide range of domestic and foreign sources dealing with accidents at large technological objects including electric power companies (Besanger et al., 2013; International Atomic Energy Agency, 2018; Report of the Unified Energy System of Russia on investigating the accident on May 25, 2005; Roy R. et al., 2015; Sibikin et al., 2017). There are some large-scale accidents worth mentioning considering their content, damage and personnel's wrong actions.

- The accident at Chagino 500-kV substation of the OJSC 'Mosenergo' mains caused interruption of power supply of socially significant objects in Moscow, Tula, Kaluga, Riazan and Smolensk regions of Russia. The damage made 1,600 mln RUB. The personnel failed to prevent massive power cut of 110 kV and 220 kV lines. Mikhailov-Chagino 500 kV line of the double-extended mode was not provided. The personnel's actions to provide and restore acceptable voltage in the southern part of the Moscow power system were not efficient;
- As a result of the power cut in Rio-de-Janeiro and São Paulo (Brazil), the oceanic coast of Rio-de-Janeiro with 10 mln residents was completely cut off power. The defect was not identified in due time and accurately;
- In the USA and Mexico, two reactors of the NPP were cut off and more than 10 mln people were left without electricity. The accident was caused by a company worker's error while organizing works at the substation;
- The massive power cut took place in the capital of Argentina, Buenos-Aires. The capital centre, the presidential palace, the Congress and government buildings were powered off. The personnel spent a lot of time on clarifying all the details of the accident and coordinating their actions;
- Munich and Moosburg (Germany) were powered off when the underground and electric trains did not work. About 500 thousand people suffered from the most large-scale accident in the last 20 years. It took a lot of time to eliminate the accident;
- The started-up 500 MW reactor of the French NPP 'St. Lawrence' exploded and about 50 kg of liquid nuclear fuel escaped because of the operator's inattention as the fuel channel was loaded inappropriately;

- There was leakage of water of the intermediate circuit and detonation of the relief valve at Unit 2 of Zaporizhzhia NPP (Ukraine). The unplanned idle time of the unit caused serious losses because of reduced generation of electricity. The operators allowed temperatures of independent circuits to increase.

Besides, let us provide some generalized data for analysing malfunctions at electric power plants, thermal and electric grids, power generating and supplying companies and power systems of the national power company Ukrenergo (Accident rates of Ukrainian power engineering facilities in 2005. The industry data document, 2005). According to the data given, at the Ukrainian power engineering objects, the number of breakdowns caused by 'the personnel's wrong actions' has increased by 25% making 6.7% of their total number, those due to 'wrong actions of the supervising personnel, service and laboratory workers' – by 6.6% making 17.8% of their total number, those due to 'influence of unauthorized people and organizations' – 52.5% making 6.8% of their total number. In general, violations of technological processes due to the personnel's wrong actions (the human error factor) make 31.3% in total according to the classifying features.

The considered factors greatly reduce the level of power security of industrial entities and the state as a whole. The term 'power security' is based on the notions of an accident, an emergency and a crisis (Reliability standards for the bulk electric systems of North America. NERC, 2007; Maintenance of power stations and grids. Rules, 2003).

In the situations described above, specific responsibility lies on the shoulders of the operating and dispatch personnel (ODP) of power facilities. Duties of ODP can be described as a chain of controlling decisions based on operational/on-line data. Decisions are made either under the standard operational mode of the power system or in case of emergency. When the standard operational mode is on, the personnel do not feel any psychological pressure, people's decisions are balanced as they have enough time to assess a situation and make a decision. In case of emergency, when the power system's stability is essential, the personnel are to take responsibility and not always make evident decisions within the shortest possible time under the pressure of taking care of material assets and people's lives.

Analysis has revealed that emergencies and accidents at large industrial plants cause great losses both in men and material. Improvement of automated control systems is accompanied by growing complexity of industrial complexes (Morkun et al., 2014). Therefore, the amount of accident damages is increasing rather than decreasing. The authors systematized and analysed the latest and most relevant factual materials on accidents and emergencies in aviation, surface and water transport, industry and power engineering. It is evident to deduce from the research the necessity of reasonable combination of automatic and automated control means as well as corresponding engineering complexes. The increased number of the latest accidents indicates expedience and urgency of human factor consideration. Automated control in power systems is one of the priorities. Special responsibility rests upon the dispatch personnel. They are unable to respond to emergencies appropriately because of psycho-physiological limitations and high emotional overload. Consequently, the problem of on-line control over such a complicated object as a power system should be solved by means of automation of smart decision-support means. Therefore, researches aimed at developing and implementing smart decision-support systems are of great scientific and practical significance (Status Review of Regulatory Approaches to Smart Electricity Grids, 2011; Tolshakov, 2014).

Assuming that the ODP is considered a component of the ADCS of power systems, the problem of intellectualization of the ADCS emergency functions is extremely acute while managing power systems in emergency operation (Bao et al., 2018; Heliodore et al., 2014; Morkun et al., 2014).

Results' analysis and the problem topicality allow formulating the following key goals of the research:

- analysing and generalizing causes of accidents in power systems and the role of dispatch personnel in emergency response;
- substantiating the topicality of the problem of intellectualization of the ACDS emergency functions of power systems;
- specifying the problems of developing and implementing digital substations;
- building a regression model of the sensitivity matrix of the electric grid to control actions;
- checking adequacy of applied methods and obtained regression models;
- developing incorporated knowledge ontologies to manage integrated power system conditions in emergency operation;
- determining a scheme and points for implementing an expert system into the ADCS complex of the integrated power system;
- demonstrating application of incorporated knowledge ontologies to power system management;
- testing the obtained results through clear and understandable examples.

2. ANALYSIS OF RESEARCH AND PUBLICATIONS

Many international scientists are investigating the theory, methods and implementation of smart power grids, their results being significant. The following works are worth mentioning (Baldinger et al., 2010; Benysek et al., 2011; *Council of European Energy Regulators, CEER Status Review of Regulatory Approaches to Smart Electricity Grids,* Brussels, 2011; Hashmi et al., 2011; Joas et al., 2018; Sobczyński et al., 2015; Swora 2011; Woszczyk, 2009). Besides, the works by Robert W. Gee (Vice President, Development and Partner Relations, The Electricity Innovation Institute), Jeffrey R. Pillon (Michigan Public Service Commission), Terry Surles (Director, Technology Systems Division, California Energy Commission), Marek Woszczyk (Vice President Energy Regulatory Office in Poland) should be considered as well.

Among the Ukrainian specialists dealing with problems of power system intellectualization, one should mention Bashlykov, Liubarskiy, Khoroshevskiy, Tolshakov, and so on.

Modern development of power systems and economic conditions of their functioning raise strict demands to their management (Bevrani H. et al., 2017; Morkun et al., 2015), the basic of which are the following:

- operational choice of generating sources;
- integration of heterogeneous power sources in the power system;
- automated elimination of accident consequences;
- efficient and reliable rendering of market ancillary services;
- resistance to security threats;
- efficient use of production assets.

Solution of the given problems is within global trends implying transformation of conventional power systems into smart power

DOI 10.2478/ama-2019-0012

systems (SPS) which are a version of 'smart grids' (Babu, 2018; Buchholz et al., 2014; Lund et al., 2017). The SPS is mostly noted for the ability to make independent decisions, self-diagnostics and recovery. Wide area management systems (WAMS) of power parameters, digital devices of relay protection and automation, advanced metering infrastructure (AMI), integrated user-side service/duel service interface (DSI), and so on are good examples of SPS services. The smart approach to preventing accidents comprises three basic components – monitoring, security assessment and security enhancement or control. Transition from conventional power systems to smart ones is given in (Technology roadmap. SmartGrid, 2011; Vingerhoets et al., 2016) and illustrated in Fig. 1.

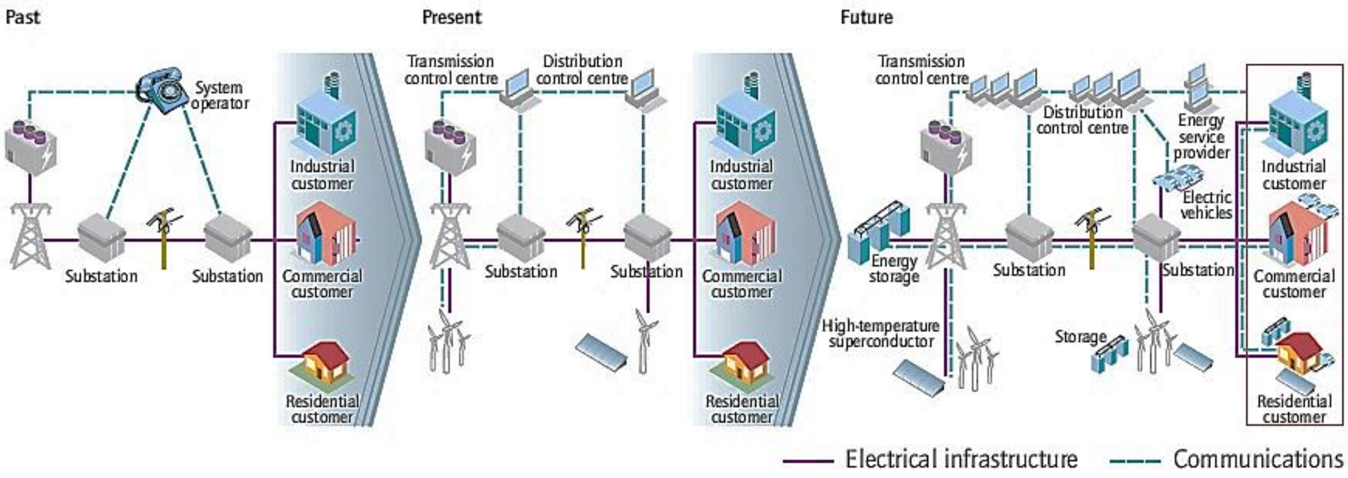

Fig. 1. Transition of power system architecture into smart one

Solution of these tasks is obligatory for controlling power system conditions (Lund et al., 2017; Morkun et al., 2018; Panasetskiy et al., 2014). To detect near-accident conditions, there is accomplished smart monitoring and security assessment based on data collection and classification of power system conditions. Data collection is performed by SCADA, which detects a set of disturbed parameters. Smart monitoring and analysis are possible solutions of the problem as, according to Morkun et al. (2014) and Negnevitskiy et al. (2013), most near-accident conditions causing system accidents are unique and there is no single algorithm of detecting these conditions.

It can be said that the concept of smart power systems and resulting smart power system management are a long-term trend in the development of large power engineering systems and their ADCS. This concept is based on the term 'intellectualization', which means making decisions by hardware items or decision-makers on the basis of accumulated and structured knowledge (professional experience).

The concept of intellectualization of power systems along with its basic principles and ways of realization is presented on a system-defined and reasonable basis by Morkun et al. (2015) and Volkova et al. (2011). The main argument in favour of intellectualization of power systems and automated emergency systems is the fact that 'potential economic and social damages because of threats and possible breakdowns of power system elements within the whole power grid are comparable to damages caused by natural disasters (hurricanes, floods, etc.) or even surpass them' (Volkova et al., 2011).

Basic functions of SPS and smart systems are accomplished through a set of digital devices and IT elements of the SPS. One of the basic SPS units is a digital substation (Berdnikov et al., 2012; Morkun et al., 2015; Morzhin et al., 2013). A digital substation is a highly automated substation in which almost all processes of data exchange between its elements and external systems and those of controlling the substation operation are controlled digitally as prescribed by the International Electrotechnical Commission – IEC 61850 ('Systems and communication networks in substations'). Meanwhile, both initial equipment of digital substations and components of information-technological and controlling systems are functionally and structurally oriented on supporting digital data exchange. Fig. 2 reveals an integrated system of a digital substation as part of SmartGrid and the group of 'smart' buildings and facilities.

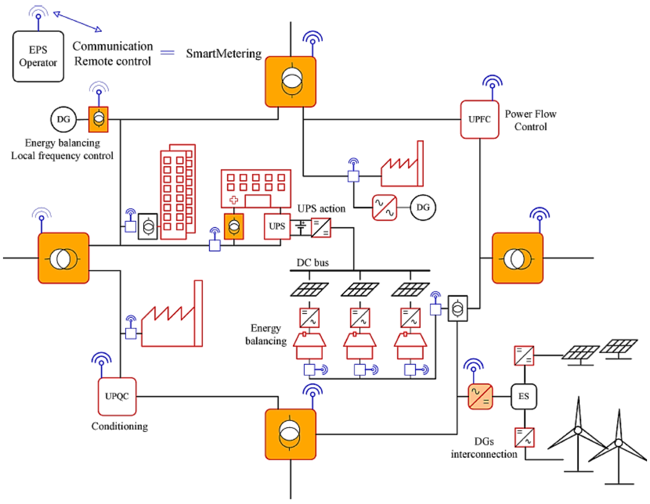

Fig. 2. SmartGrid with SmartMetering & SmartBuilding technology (The figure is borrowed from the paper by Benysek, Kazmierkowski, Popczyk J., Strzelecki R., 2011)

Introduction of digital technologies and intellectualization of the ADCS of power systems have a considerable positive effect. Yet, intellectualization of power systems faces serious problems of updating certain power facilities. Additional problems arise from social and economic conditions, namely, scarce funding, personnel's low qualification, outdated regulatory and instructive bases, established traditions of work organization, and so on, for example, indicates that 'most similar systems are restricted to functions of data acquisition, pre-processing and visualization. Generalizing assessments of current situations and decision-making resulting in corresponding plans of further actions remain the responsibility of the personnel as before'. Analysis of the potential of current smart power facilities and systems (Dronova, 2016) allows concluding that 'systems of personnel's support in decision making are reasonable to be used as new components integrated into the automated control system of the given power equipment'.

Following the analysis of many research works, we can draw a conclusion that creating smart power systems and facilities is quite promising, yet at present, there are some objective problems of realizing these projects.

Some smart hardware and software complexes-advisers can be used as the most balanced and efficient solutions to the problem of emergency control system automation within the automated dispatch management system of power systems. They are noted for relatively low initial investment, absence of auxiliary requirements to the current data infrastructure for installation, high technical and economic efficiency. Dispatch advisers are hardware and software packages of decision-support systems (DSS) based on artificial intelligence. There is available wide national and international experience of creating DSS for controlling power systems (Kuno et al., 2012).

Thus, comparative analysis of available scientific and engineering decisions in the sphere of automated emergency control systems allows for the conclusion about topicality and necessity of developing smart DSS and their introduction as part of the ADMS of power systems.

3. RESEARCH OBJECTIVES

The conducted analysis enables formulating the task of creating a support system of the power system dispatcher's managerial decisions. Basic functions performed by DSS should be guiding. The whole variety of the functions can be presented as two basic directions of DSS actions:

- identifying an emergency;
- developing and applying controlling impacts.

The problem of identifying an emergency should be solved by methods of recognition (classification). In this case, on the basis of a training sample (when disturbance, the character of transition and severity estimates are known), a function of measured parameters of the mode and disturbance distributing conditions according to severity is built (Bao et al., 2015).

The second subtask is associated with finding the most effective points of applying control actions (power system units) and the structure of the actions to enhance the system's stable functioning. This problem can be solved by means of methods of experiment design, taxonomy, and so on.

After creating the DSS and determining the technology of introducing it into the current online data management complex, its knowledge base should be replenished. For this purpose, experiments of the dispatcher's impacts on the grid scheme of the power system are planned and conducted. The knowledge-base is filled with images of emergency conditions and formalisms of the dispatcher's decisions accompanied by estimates of control actions in the form of response matrices. The procedure of DSS functioning is based on developing a scenario of a software package operation in the environment of the total system of automated dispatch management of power systems. According to the operation scenario, efficiency of the DSS is assessed and corresponding indices are chosen and grounded.

When using the methods of factorial design, a range of changes of control dispatch actions is determined in various units of the power system and their influence on the system's condition is assessed. Multiple calculations of the transient process guided by the factorial design followed by data processing should result in forming a dependency of a response on the control action vector.

The relevant value of significance of separate impacts is reflected in corresponding factors, their impact on the response being assessed by setting them equal to zero. Considering reciprocal influence of substations in the transient condition, they can be combined into classes according to the influence quantity.

The presented plan provides the following research tasks:

- determination of mode parameters characterizing the current condition of the power system;
- design and conduction of experiments to assess the influence of control actions on modes of characteristic controlled units of the power system;
- assessment of adequacy of models and formation of influence response functions of control actions on conditions of controlled units of the power system;
- formation of empirical response matrices of the power system as to control actions on the basis of response functions;
- formation of professional ontologies based on empirical knowledge-bases of condition characteristics of controlled units of the power system;
- development of the integrated scheme of the DSS accompanied by ADMS means based on incorporated professional ontologies.

4. RESEARCH RESULTS

To solve the research problems, the general methodology of the research should be expressed as follows. Solution of the problem of providing high-quality control of the power system condition is based on the fact that bulk of the input data on the system scheme and condition under study is processed in advance and asynchronously. Therefore, the data can be considered a knowledge base. Control functions are formed according to detected application points and adjustment of control actions. The control-action adjustment is conditioned by methods of multiple planned designed experiments and built regression models. After statistic adequacy tests of the resulted models, they can be used as new knowledge about the control over the condition of a certain dispatch control object. The research applies general methods of building architecture of smart systems and automated dispatch control systems. There are used methods of experiment planning, mathematical statistics, the theory of sets, the theory of electrical circuits and formal languages. Adequacy of obtained results is checked and harmonized with the activity of dispatch personnel. For this reason, the research methods are relevant and can be applicable to the professional field chosen. The problem of determining a subset of controlling units of the power system involves transformation of $Y = F(X)$ (X is the initial n-dimensional space of factors, *Y* is a new m-dimensional space, *n* > *m*). Dimensionality in the space Y should be minimal, yet sufficient for distinguishing this class-taxon. Next, the problem of choosing optimal control actions is solved by the methods of the experiment design theory.

Parameters characterizing a standard condition, a disturbance and a grid structure are chosen as independent factors. An adaptive criterion of the system condition quality (the amount of cut load and generating capacities, reconfiguration of the grid scheme) are used as control actions.

To study a particular emergency, a set of calculation experiments is conducted to determine optimal amounts of control actions and obtain a satisfactory mode. After processing all experiment results, there are obtained polynomial dependencies characterizing the standard (near-accident) condition, the grid structure and disturbance (independent impacts) and optimal control action adjustment (Gluskin et al., 2009):

$$u_i = K_{i0} + \sum_{j=1}^{n} K_{ij}X_j + \sum_j \sum_l K_{ijl}X_jX_l + \cdots . \quad (1)$$

The considered methods provide the basis for the expert DSS of the power system dispatcher. The research is conducted on the operational guidance materials of the dispatch control office of the National Dispatch Centre (NDC) of the Integrated Power System (IPS) of the NPC 'Ukrenergo'.

The knowledge base is formed by combining dispatch instructions to control active power interchange and new knowledge based on experiment data of mode tests.

To assess condition parameters of the studied cluster of the power grid, a model of equations of the established condition is used in the form of power balance in the units:

$$\dot{\omega}_{sk}(\dot{U}) = \dot{S}_k^* - \dot{Y}_{kk}\dot{U}_k\dot{U}_k^* - \sum_{j=1, j\neq k}^{N} \dot{Y}_{kj}\dot{U}_j\dot{U}_k^* , \quad (2)$$

where: $\dot{\omega}_{sk}(\dot{U})$ – is an unbalance function in the unit k, $\dot{S}_k^*$ – is a conjugate complex of the k-th unit power, $\dot{Y}_{kk}$ – is intrinsic conduction of the k-th unit, $\dot{U}_k$ – is a voltage complex of the k-th unit, $\dot{U}_k^*$ – is a conjugate voltage complex of the k-th unit, $\dot{Y}_{kj}$ – is reciprocal conduction of the k-th and j-th units, N – is the number of units in the studied cluster of the grid.

To make model (2) applicable in the software package, the variables are separated and presented by real numbers in polar coordinates:

$$\omega_{Pk}(U) = P_k - g_{kk}U_k^2 - U_k \sum_{j=1, j\neq k}^{N} U_j\left(g_{kj}\cos\delta_{kj} - b_{kj}\sin\delta_{kj}\right), \quad (3)$$

$$\omega_{Qk}(U) = Q_k - b_{kk}U_k^2 - U_k \sum_{j=1, j\neq k}^{N} U_j\left(b_{kj}\cos\delta_{kj} + g_{kj}\sin\delta_{kj}\right), \quad (4)$$

where: $\delta_{kj} = \delta_k - \delta_j$, δ_k, δ_j – are phase angles of vectors of the voltage modules of the k-th and j-th units.

The experiments are aimed at finding characteristics of intensities of interconnection of condition controlled parameters of a dispatch control object, in particular, active power flow and factors of dispatch control actions as to the electric grid (for example, by varying capacities of generating units and transformation factors of coupling transformers of 750/330-kV nominal voltage).

The resulted set of models present a binary relation defined on the subsets of controlling and controlled parameters:

$$N'\beta P' = \begin{matrix} \{(n_1', p_1'), & \ldots, & (n_1', p_k'), \\ (n_2', p_1'), & \ldots, & (n_2', p_k'), \\ \ldots, & \ldots, & \ldots \\ (n_m', p_1'), & \ldots, & (n_m', p_k')\} \end{matrix} , \quad (5)$$

where: $N'\beta P'$ – is a binary relation defined on the subsets of controlling $N' = \{n'|i = 1, m\}$ and controlled $P' = \{p'|j = 1, k\}$ – parameters.

Interconnection models of subsets of controlling and controlled parameters are presented in the form of a response matrix:

$$\begin{vmatrix} \beta_{11} & \ldots & \beta_{1k} \\ \beta_{21} & \ldots & \beta_{2k} \\ \ldots & \beta_{ij} & \ldots \\ \beta_{m1} & \ldots & \beta_{mk} \end{vmatrix} , \quad (6)$$

where: $\beta_{ij} = (n_i, p_j)$ – is an impact ratio, n_i, p_j – are controlling and controlled parameters of a dispatch control object. The ratio β_{ij} – is realized as standard regression models:

$$\bar{Y} = b_0 + \sum_{i=1}^{k} b_iX_i + \sum_{i=1}^{k}\sum_{j=1}^{k} b_{ij}X_iX_j + \sum_{i=1}^{k} \ldots \sum_{n=1}^{k} b_{i\ldots n}X_{i\ldots n} + \sum_{i=1}^{k} b_{ii}X_i^2 , \quad (7)$$

where: $b_0, b_i, b_{ij}, b_{i\ldots n}, b_{ii}$ – are estimates of regression factors determined by experiment results.

After statistical study of the obtained models to assess their adequacy, they are used as new knowledge about controlling a dispatch control object's condition. Application of this kind of knowledge as elements of the response matrix allows rejecting full-scale calculations of the set mode of the power system while assessing the required actions and designing dispatch decisions. This fact facilitates the DSS switching over to an on-line mode.

The network map of the following classes of nominal voltage (750 kV, 500 kV, 330 kV, 220 kV) is used in the function of the rated one. The studied line has 156 units and 210 branches, ten of which are parallel. There are 26 autotransformers and 184 power lines. 9 autotransformers are characterized by complex values of transformation factors. In 42 units, values of voltage modules are fixed and variation limits of the available reactive power are set. To compensate the charge capacity of 750 kV ETL (electric transmission line), reactors are switched on in 13 units of the network map.

Parameters of the mode taken as the initial one correspond to the autumn consumption schedule and time of the day from 4 p.m. to 5 p.m.

While forming the experimental part of the knowledge-base, the research focuses on the dispatch interchange control at South-Ukraine Nuclear Power Plant-Vinnitsa through controlling the power of some large generating units and complex transformation factors of coupling autotransformers. The impact of reactive power flow in the function of an important factor of dispatch control is not studied because of invariance of tested methods in terms of the content of the models.

Tab. 1 presents input parameters of the experiments for controlled units of the power system (a linear response model is chosen in a first approximation).

Calculation and analytical experiments result in sets of response functions for control actions in the given units. Obtained regression models adequately describe the influence of active power flow at South-Ukraine Nuclear Power Plant-Vinnitsa and can be used to form dispatch control actions.

After checking the value of regression factors, the following response function is obtained:

$$Y = 1409.32 + 81.40X_2 + 49.69X_3 + 142.98X_4 . \quad (8)$$

True factors of the model can be verified by control computation of the steady-state condition. Let us choose the values of parameters at the zero level. This variant provides an evident result while using the model P = 1557.99 MW. The calculated steady-state condition for the given conditions result in the flow value of P = 1558.50 MW corresponding to the relative error of 0.03 %.

Tab. 1. Levels of experiment factors and variation intervals

#	Units	Factors	Factor levels			Interval, *I*	Dimension
			-I	*0*	*+I*		
1	2	3	4	5	6	7	8
1	Kakhovka MSDS	X1	-413.41	-327.41	-241.41	86.00	MVA
2	Kaniv HPP	X2	-220.48	-99.32	21.82	121.15	MVA
3	Kyiv TPP6	X3	-68.60	68.16	204.91	136.76	MVA
4	Dniester HPP	X4	59.91	239.64	419.38	179.73	MVA

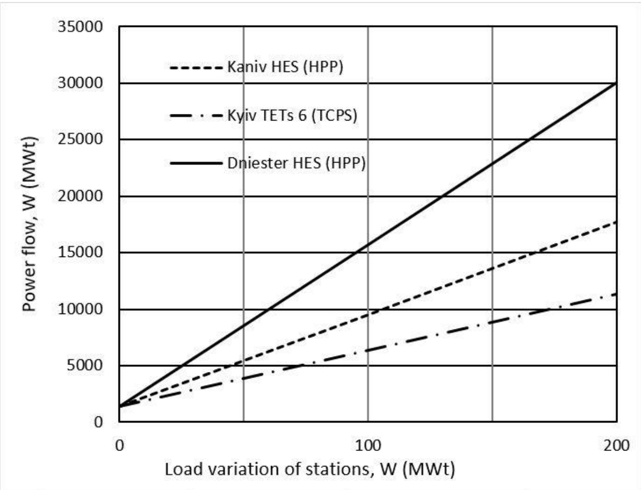

Fig. 3. Experiment data of the impact of generating stations on power flow at South-Ukraine Nuclear Power Plant-Vinnitsa

When fixing some regression parameters (4) at the zero level, illustrations of the impact of generating stations on power flow are obtained (Fig. 3).

To verify the adequacy of the applied mathematical apparatus in building regression models, Shapiro-Wilk *W*-test is used (Hanusz Z., 2016).

While analysing the conditions of power systems, full-scale tests are replaced by model calculations, so dispersion of parameters can be assessed in a simplified form:

$$\sigma^2(y) = \sum_{i=1}^{n} b_i^2 \sigma^2(X_i^H) + \sum_{i=1}^{N}\sum_{j=1}^{N} b_{ij}^2 \sigma^2(X_i^H)\sigma^2(X_j^H). \quad (9)$$

Experiment results reveal that $\bar{Y} = 1409.32$.

In this case,

$$\sum_{i=1}^{16}(Y_i - \bar{Y})^2 = 472864.11$$

and the value of adequacy dispersion is

$$\sigma^2 = \frac{472864.11}{15} = 31524.27.$$

As the *n*-sample is an even number, the difference number is *k* = 16/2 = 8.

According to table data, we obtain

$$b = \sum_{i=1}^{8} a_{nk}\Delta k = 672.40\ .$$

In this case, the *W*-test is

$$W = \frac{b^2}{(n-1)\sigma^2} = \frac{452121.76}{15*31524.27} = 0.956\ .$$

As $W > W_{0.05}$, the mathematical apparatus is adequate to solve problems and its application does not cause any false interpretation of the object domain.

To introduce the developed DSS, it is necessary to solve two important problems:

- determination of possible places to install the system and its functional orientation at installation points;
- creation of software-to-software interface of the system on a real-time basis.

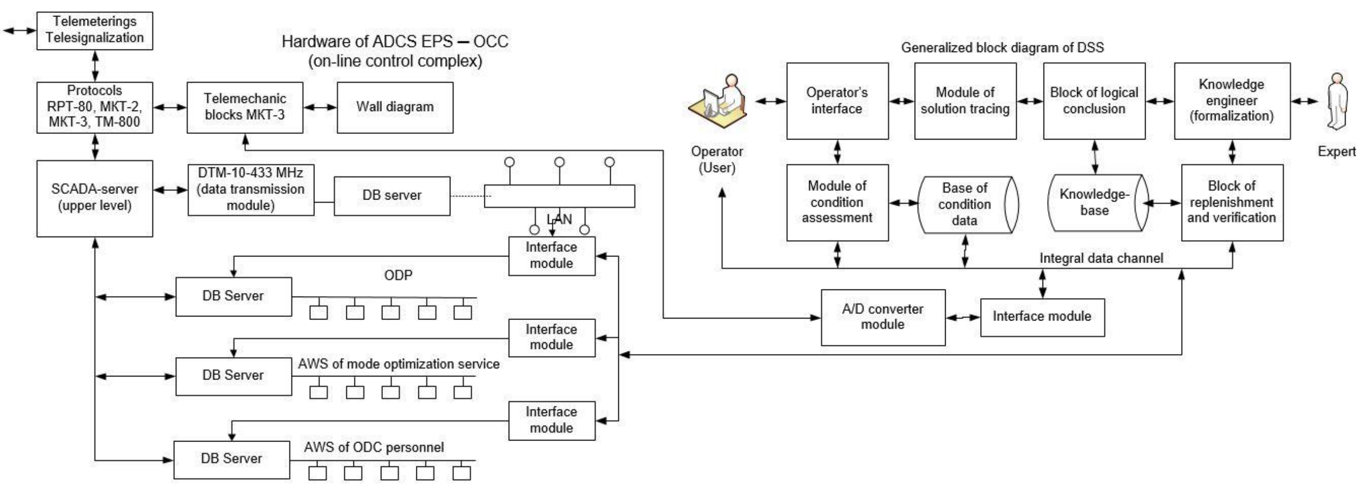

Fig. 4. Suggested structural scheme of integration of the DSS into the ADCS to monitor power system conditions

The indicated problems can be solved after considering the structure and principles of functioning software and hardware means of the ADCS of a particular power facility. The dispatch control tasks are realized by means of data collection, transmission, processing and display as well as and CASE-tools enhancing the solution of control tasks and data connection with hierarchical control levels. The control levels are equipped with universal computers to exchange on-line information with a set of hardware means of the integrated dispatch control (IDC). The overall description of the ADCS hardware is provided in Morkun et al. (2015), Peng et al. (2018), and PKP Energetyka (2018). The following scheme of DSS incorporation into the ADCS of power systems is suggested (Fig. 4).

Possible installation points of the created expert system can be defined in the following way.

With regard to hardware means of data processing:

- a local network of IBM-compatible PCs with cross-machine exchange of on-line data including an automated work place connected through a file-server computer with the central computer to access hardware means, programs and the data bank;
- a circuit for cross-machine exchange of on-line data along with automated formation of daily records, process-statistical and economic-planning data based on teleprocessing;
- within the circuit of data acquisition, display and processing, the use of the mentioned hardware means of transmission of on-line telemetry data.

With regard to subsystems of mathematical support:

- the environment of software means of on-line data and computation complexes;
- tasks of dispatching on-line control and statistical data processing;
- the subsystem of recording and analysing efficiency of previous daily conditions;
- software support of an on-line data base;
- applied mathematical support associated with restriction of power flows across separate sections and lines;
- tasks of current improvement of HPP modes by computing means;
- tasks of current improvement in terms of transformation factors and loads;
- mathematical support of process-statistical data processing.

With regard to the dispatch and technological personnel:

- a dispatcher's automated work place;
- a process engineer's automated work place based on the local computer network;
- an automated work place of an engineer of the mode optimization service;
- an automated work place of an engineer of the mathematical support development and operation service.

5. TESTING

To test the suggested method, a clear and understandable example is provided.

Considering instructive and empirical data, the DSS is built to control power flow at the interchange of South-Ukraine Nuclear Power Plant-Vinnitsa (SUNPP-Vinnitsa). A knowledge base provides the foundation to build ontologies of concepts, facts, products and databases.

The DSS controls power flows for a current condition of the grid. When the value exceeds the standardized limits, the system generates control actions on the basis of sensitivity matrices. Next, the products from the rule base are used to form pieces of advice for a dispatcher to provide directions, rates of controlling the condition or changing the power system diagram.

The obtained designs provided the basis for testing emergency trainings (TET) of the dispatch personnel. The calculating models of Ukraine's integrated power system were used as control objects. Two equal groups of dispatchers of equal qualification and work experience took part in the trainings:

- group 1 (2 people per shift) without using the DSS;
- group 2 (2 people per shift) using the DSS.

The dispatchers' actions were assessed by experts on a scale from one to five according to the methods suggested in (Merkurev G.V., 2002).

The initial conditions of the training include:

- the controlled object is the interchange of SUNPP-Vinnitsa including the following high-voltage (HV) lines: 750 kV HV-line of SUNPP-Vinnitsia, 330 kV HV-line of Konotop-Nizhyn, 330 kV HV-line of KremHPP-Cherkasy, 330 kV HV-line of SUNPP-Pobuzhzhia, 330 kV HV-line of Tryhaty-Adzhalyk, 330 kV HV-line of Homel-Chernihiv, 330 kV HV-line of Mozyr-ChNPP;
- the operation mode is standard;
- the operation mode with the Interconnected Power System (IPS) of East European countries is parallel;
- the power flow value along the 750 kV HV-line of SUNPP-Vinnitsia is 1300 MW;
- the admissible power flow in the interchange for the set conditions is 3600 MW;
- the fixed current power flow along the intersystem transit (interchange) is 3640 MW;
- the fixed exceeded limit of the intersystem power flow is 40 MW;
- the partial failure or insufficient efficiency of the emergency control automatics is fixed;
- there is a failure of synchronous operation of Ukraine's IPS and the East European one.

The training is aimed at eliminating the exceeded intersystem power flow within 1–2 hours according to the instruction. Otherwise, the power system dispatcher has to divide asynchronously operating parts of the integrated power system.

The training strategy implies fulfilling the training task and forming the following assessment parameters of the dispatchers' activity (Merkurev G.V., 2002):

- q_1 is correct timely actions;
- q_2 is unfulfilled actions;
- q_3 is incorrect actions;
- q_4 is behind-schedule actions;
- q_5 is actions performed earlier than necessary;
- q_6 is unnecessary actions;
- q_7 is non-optimal actions.

The results of the conducted trainings are in Tab. 2.

During the training, on the basis of the DSS knowledge base and the sensitivity matrices, the required controlling actions are determined:

- the total controlling action is 12.5 MW;
- the controlling action of the Dniester HPP is 11.36 MW:
- the controlling action of Kaniv HPP is 1.14 MW.

After conducting independent emergency trainings (both with and without using the DSS) and obtaining the parameters q_1–q_7,

the following expert professional and psychological characteristics of dispatchers are obtained:
- α is expertise;
- ρ is reliability;
- β is proficiency level;
- γ is psychological stability;
- δ is immediacy and accuracy;
- λ is the intensity of natural failures of dispatcher shifts;
- Y is the evaluation of contingent damage due to power under-supply and its reduced quality.

Tab. 2. Final results of the dispatch personnel's testing emergency trainings

Indices without using of the DSS	Indices with the DSS
q_1 = 4.80	q_1 = 4.96
q_2 = 1.0	q_2 = 1.0
q_3 = 0.5	q_3 = 0.42
q_4 = 2.2	q_4 = 1.94
q_5 = 0.2	q_5 = 0.2
q_6 = 0.2	q_6 = 0.12
q_7 = 1.8	q_7 = 0.55
α = 4.8/11.0 = 0.43	α = 4.96/9.19 = 0.54
ρ = 1 − 4.4/11.0 = 0.6	ρ = 1 – 3.68/11.03 = 0.67
β = 1 − 3 / 11.0 = 0.76	β = 1 – 2.36/11.03 = 0.79
γ = 1− 0,4/11.0 = 0.964	γ = 1− 0,32/11.03 = 0.971
δ = 1 – 4.3 / 11.0 = 0.61	δ = 1 – 2.49/11.03 = 0.77
λ = 0.048, failures/month	λ = 0.042, failures/month
Y = $\alpha_1 P_1 2.8$	Y = $\alpha_1 P_1 0.92$

Generalization of the training results enables conclusions of the DSS efficient application to dispatch control of the IPS in emergency, concerning the following:
- the personnel's professional and psychological characteristics have improved due to the DSS;
- intensity of dispatcher shifts' failures has reduced;
- the contingent damage due to power undersupply has decreased.

6. CONCLUDING REMARKS

The research is an original investigation into intellectualization of power facilities control. The manuscript is original research as a specific approach to building a knowledge base is suggested. The knowledge base is based on the dispatchers' instructions for accident response. At the same time, regression dependencies of the power system's sensitivity to controlling dispatcher actions are included into production rules. The method of incorporating various forms of knowledge representation within a single smart system is developed to build the knowledge base. The study formulates an integrated approach to incorporating professional knowledge to build smart decision-support systems and automated control of complex-structured objects. It differs by simultaneous implication of integrated forms of knowledge representation comprising concepts, facts and production rules. All the levels of the knowledge structure are described by means of a single model of ontologies enabling us to unify representation and processing of knowledge of power grid conditions.

The mathematical apparatus of presenting and using ontologies is improved and noted for being based on fundamental forms of representing knowledge irrespective of the subject areas.

Thus, we can draw the following conclusions:
- there are determined condition parameters characterizing the current condition of the IPS, power flows in certain power system lines being such parameters;
- a set of experiments has been planned and conducted, the influence of control actions on condition parameters characterizing the controlled areas of the IPS being determined;
- the obtained ratios of impacts have confirmed numerical adequacy of the regression models of response functions to generate control actions on the power system parameters;
- the sensitivity matrices as ratios between the values of controlling and controlled parameters of the power system condition have been built;
- there are suggested new ontologies of knowledge bases of the dispatch control over the power system conditions in the form of sensitivity matrices based on factor condition models considering the interrelation of controlling and controlled parameters of the power system condition;
- a scheme of integrating the DSS into the ADCS is offered to monitor the IPS condition on the basis of the empiric knowledge base of condition characteristics of the power system;
- practical testing of the obtained results through a clear and understandable example is conducted and the elaborated theoretical models are confirmed.

REFERENCES

1. Accident rates doubled in Ukraine's power system (2015) (in Russian), retrieved from: https://economics.unian.net/energetics/1073586-avariynost-v-energosisteme-ukrainyi-za-god-vyirosla-vdvoe.html – 30.04.2015.
2. Accident rates of Ukrainian power engineering facilities in 2005. The industry data document (2005). Association of power enterprises 'Industry Reserve and Investment Fund of Power Engineering Development' (in Ukrainian). Enerhia, Kyiv.
3. **Babu N. R.** (2018), *Smart Grid Systems: Modeling and Control*, CRC Press, Apple Academic Press, 290.
4. **Baldinger F., Jansen T., Riet M., Volberda F.** (2010), Nobody knows the future of Smart Grid, therefore separate the essential in the secondary system – *Developments in Power System Protection, the 10th IET International Conference (DPSP)*, 29 March – 1 April 2010, Manchester, UK.
5. **Bao Y., Guo Ch., Zhang J., Wu J., Pang S., Zhang Zh.** (2018), Impact analysis of human factors on power system operation reliability, *J. Mod. Power Syst. Clean Energy*, Springer Verlag, Berlin, 6(1), 27–39.
6. **Bao Y., Li Z., Wen D., Guo Ch.** (2015), Development and design of dispatcher training simulation evaluation system based on IDAC, *Conference: 2015 IEEE PES Asia-Pacific Power and Energy Engineering Conference (APPEEC)*, 1–5.
7. **Benysek G., Kazmierkowski M.P., Popczyk J., Strzelecki R.** (2011), Power electronic systems as a crucial part of Smart Grid infrastructure – a survey, Bulletin of the Polish Academy of Sciences: Technical Sciences, Power electronics, 59(4), 455–473.
8. **Berdnikov R.N., Morzhin Yu.I., Shakaryan Yu.G.** (2012), Basic principles of the smart power engineering system of Russia with the active and adaptive grid. Power of the Unified Grid(in Russian), *Energiya Yedinoy Seti*, 4, 4–11.

DOI 10.2478/ama-2019-0012

9. **Besanger Y., Eremia M., Voropai N.** (2013), Major grid blackouts: Analysis, classification, and prevention, *Handbook of Electrical Power System Dynamics: Modeling, Stability, and Control*, New Jersey: Wiley – IEEE Press, 789–863.
10. **Bevrani H., Hiyama T.** (2017), *Intelligent Automatic Generation Control*, CRC Press, Taylor & Francis Group, 308.
11. **Buchholz B.M., Styczynski Z.** (2014), *Smart Grids - Fundamentals and Technologies in Electricity Networks*, Springer Verlag, Berlin, 396.
12. **Dronova Yu.V**. (2016), Risks of implementing smart grids into power complexes of the Russian Federation regions. Economy and Management: Problems, Solutions, Management Problems (in Russian), 2 (6), 77–83.
13. **Gluskin I.Z., Iofev B.I.. Meklin A.A., Chekalovec L.N.** (2009), Emergency automation in power systems (in Russian), Moscow: Znak, 568.
14. **Hanusz Z., Tarasinska J., Zielinski W.** (2016), Shapiro–Wilk test with known mean, REVSTAT Statistical Journal, 14(1), 89–100.
15. **Hashmi H.M., Hanninen S., Maki K.** (2011), *Survey of Smart Grid Concepts, Architectures and Technological Demonstrations Worldwide*, IEEE PES Conference, Innovative Smart Grid Technologies (ISGT), Medellin, Oct.
16. **Heliodore F., Poullain S., Boussaad I., Nakib A.** (2014), Methodology for management of power system emergency situations, *PGMO-COPI'14 Conference on optimization & practices in industry*, 3.
17. **International Atomic Energy Agency** (2018), Nuclear Power Plant Operating Experience, *IAEA*, Vienna, 53.
18. **Joas F., Oswald K., Wido Witecka** (2018), *RAP: Report on the Polish Power System. Version 2.0 Study commissioned by Agora Energiewende*, Mercator Foundation and the European Climate Foundation, 48.
19. **Kuno M.Ya., Kondratev A.N., Chalisov Yu.I., Malyishev A.V., Morozovich R.B., Sulimov V.A.** (2012), Dispatch Adviser for eliminating overloads in the power system. Technical and Software Means of Automation Systems (in Russian), 5(34), 34–37.
20. **Lund H., Østergaard P.A., Connolly D., Mathiesen B.V.** (2017), Smart energy and smart energy systems, *Energy*, 137, 556–565.
21. **Merkurev G.V.** (2002), Operative and dispatch control of power systems. Methodological Guide. Teaching Guide (in Russian). Edition of the Energy Training Center, 116.
22. **Morkun V., Morkun N., Tron V., Hryshchenko S.** (2018), Synthesis of robust controllers for the control systems of technological units as iron ore processing plants, *Eastern European Journal of Enterprise Technologies*, 1(2-91), 37–47.
23. **Morkun V., Tcvirkun S.** (2014), Investigation of methods of fuzzy clustering for determining ore types, *Metallurgical and Mining Industry*, 5, 11–14.
24. **Morkun V., Morkun N., Pikilnyak A.** (2015), Adaptive control system of ore beneficiation process based on Kaczmarz projection algorithm, *Metallurgical and Mining Industry*, 2, 35–38.
25. **Morkun V., Morkun N., Pikilnyak A.** (2014), The adaptive control for intensity of ultrasonic influence on iron ore pulp, *Metallurgical and Mining Industry*, 6, 8–11.
26. **Morkun V., Morkun N., Tron V.** (2015), Model synthesis of nonlinear nonstationary dynamical systems in concentrating production using Volterra kernel transformation, *Metallurgical and Mining Industry*, 10, 6–9.
27. **Morkun V., Morkun N., Tron V.** (2015), Formalization and frequency analysis of robust control of ore beneficiation technological processes under parametric uncertainty, *Metallurgical and Mining Industry*, 5, 7–11.
28. **Morzhin Yu.I., Popov S.G.** (2013), Digital substation. Concept, implementation technology (in Russian). Unified Grid Power, 5, 4–19.
29. **Negnevitsky M., Tomin N., Panasetsky D., Kurbatsky V.** (2013), Intelligent Approach for Preventing Large-Scale Emergencies in Electric Power Systems, *Proceedings from IEEE International Conference on Electric Power Engineering PowerTech*, Grenoble, France, 16-20 June, 1–6.
30. Report of the Unified Energy System of Russia on investigating the accident on May 25, 2005 (2005) (in Russian). RAO «UES of Russia», appointed by order, 331, Moscow, 48.
31. **Panasetskiy D.A., Tomin N.V., Kurbatskiy V.G., Voropay N.I., Efimov D.N.** (2014), Smart emergency control of power system modes (in Russian). The Institute of Control Problems named after V.A. Trapeznikov of the Russian Academy of Sciences, Moscow, 4770–4782.
32. **Peng Zh., Na Liu, Jing Ch., Qi-feng Zh., Man-man Lin** (2018), A New Dispatch Control Integration System of the Smart Grid Based on the Regional Network Centralized Protected Mode, *Journal of Clean Energy Technologies*, 6(4), 324–332.
33. **PKP Energetyka** (2018), Implementation of the centralised system of controlling traffic in the SCADA / ADMS power and traction system. Engineering standards for NC facilities. Standardisation and Data Quality (in Polish), Warszawa, 33.
34. Reliability standards for the bulk electric systems of North America. NERC (2007), Retrieved from: http://www.nerc.com – 18.08.2017.
35. **Roy R., Vijayakumar A., Nair R.** (2015), A Study on Electrical Accidents and Safety Measures, *International Journal of Latest Trends in Engineering and Technology* (IJLTET), 5(2), 147–154.
36. **Sibikin Yu.D.** (2017), Maintenance of electrical equipment of power stations and substations: teaching guide for students of higher educational institutions (in Russian). Moscow: Berlin, Direkt-Media, 447.
37. **Sobczyński D., Balawejder M.** (2015) Participation of consumers in Smart Grid development (in Polish), *Scientific Journals of Rzesziw University of Technology, Series: Electrotechnics*, RUTJEE , 34(4), 5–13.
38. Status Review of Regulatory Approaches to Smart Electricity Grids (2011), Council of European Energy Regulators, CEER, Brussels, 37–40.
39. **Swora M.** (2011), Smart Grids after the Third Liberalization Package: Current Developments and Future Challenges for Regulatory Policy in the Electricity Sector, *Yearbook of Antitrust and Regulatory Studies*, 4(4), 9–22.
40. Maintenance of power plants and grids. Rules (2003) (in Ukrainian), DP "NTUKC" AsElEnergo, 599.
41. Technology roadmap. Smart Grids (2011), International Energy Agency, OECD/IEA, 49.
42. **Tolshakov, A.V.** (2014), Smart Grid: development, practice, problems (in Russian). Enerhonadzor, 1(53).
43. **Vingerhoets P., Chebbo M., Hatziargyriou N.** (2016), *The Digital Energy System 4.0, European technology platform Smartgrids*, 72.
44. **Volkova I.O., Okorokov V.R., Okorokov R.V., Kobets B.B.** (2011), Concept of smart power systems and its potential in the Russian power engineering (in Russian). The Russian Academy of Sciences. The Institute of National Economy Forecasting. The Open Seminar "Economic Problems of the Power Complex", INP RAN, Moscow.
45. **Woszczyk M.** (2009), The Smart Grid and Smart Metering Polish Perspective, *ERRA Chairmen Meeting*, Istanbul, 17 November, 19.

DOI 10.2478/ama-2019-0013 acta mechanica et automatica, vol.13 no.2 (2019)

DEGRADATION OF FUNCTIONAL PROPERTIES OF PSEUDOELASTIC NiTi ALLOY UNDER CYCLIC LOADING: AN EXPERIMENTAL STUDY

Volodymyr IASNII*, Petro YASNIY*

*Department of Structural Mechanics, Ternopil Ivan Puluj National Technical University, Ruska str. 56, 46001 Ternopil, Ukraine

v_iasnii@tntu.edu.ua, petroyasniy@gmail.com

received 14 March 2019, revised 3 June 2019, accepted 6 June 2019

Abstract: The influence of the cyclic loading on the functional properties of NiTi was studied. Cylindrical specimens with a diameter of 4 mm and a gage length of 12.5 mm were tested under uniaxial cyclic loading with control crosshead displacement at a temperature of 0°C. The dependences of the stress and strain range as well as dissipation energy on the number of loading cycles at different initial stress range were analysed. During the first 10 loading cycles, a rapid decrease in the strain range and energy dissipation was observed. Dissipation energy was invariant to the loading cycles' number at N > 20 cycles and to the stress range that did not exceed the martensite finish stress level, was within the same scatter band and can be described by the single dependence. With the stress range growth at N < 20 cycles from 509 to 740 MPa, the value of dissipation energy increases and that of relative dissipation energy decreases. Loss coefficient, which characterises material damping ability, significantly decreases during the first 10 loading cycles and remains practically unchanged up to the failure of the specimens. At the stabilisation area, the loss coefficient is almost non-sensitive towards the stress range.

Key words: pseudoelastic alloy, functional properties, dissipation energy, strain range, stress range

1. INTRODUCTION

Shape memory alloys (SMA) are the functional materials characterised by the shape memory effects and pseudoelasticity. Their application depends on the phase transformation temperatures, mechanical and functional properties, type of loading (static, cyclic, multiaxial and thermo-mechanical) (Sun L. et al., 2012; Hsu et al., 2019) and environment (Gamaoun et al., 2014; Iasnii et al 2019).

SMA are increasingly used in actuators (Nespoli et al., 2010), implants (Auricchio et al., 2015; Morgan, 2004; Chen and Thouas, 2015), and in earthquake engineering (Qiu and Zhu, 2017) because of the high ability to energy dissipation, as well as damping devices (Ozbulut et al., 2011; Yasniy et al., 2017; Torra et al., 2012; Isalgue et al., 2006) or other structural elements (Menna et al., 2015; Mohd Jani et al., 2014). As they are subjected to intense cyclic loading during operation, it is important to ensure their reliability and lifetime for low-cycle fatigue.

The balance between energy dissipation and structural fatigue lifetime should be reasonably taken into account whilst designing damping devices made of NiTi alloy.

It is known that with the increasing loading cycles, the SMA functional properties (pseudoelasticity) degrade. These properties can be characterised by the strain range, residual strain, dissipated energy (Kang et al., 2012; Predki, 2006, Iasnii and Yasniy, 2018; Eggeler et al., 2004) and loss factor. This factor represents the ratio of dissipated energy per cycle to maximum potential energy and was considered by Predki et al. (2006), Piedboeuf and Gauvin (1998) and Pan and Cho (2008). An increase in the average stress significantly reduces the residual strain of NiTi alloy under strain-controlled cyclic test (Kang et al., 2012). The residual strain is regarded as related to some oriented martensite, which is not transformed back into austenite during the reverse phase (Auricchio et al., 2003). Repeated changes in forward and reverse phases produce some defects in the material (Abeyaratne and Kin, 1997), resulting in localised internal stress (Tanaka et al., 1995) enabling two-way shape memory effect in SMA.

Particularly, residual and transformation hardening increase with the increase in the number of loading cycles and strain rates from 3.3×10^{-4} s^{-1} to 3.3 10^{-2} s^{-1} in super-elastic NiTi SMA microtube (50.32 % Ni) specimens during strain-controlled testing (Kan et al., 2016). The dissipation energy decreases with the increase in loading cycles. However, with the increase in the strain rate from 3.3×10^{-3} s^{-1} to 10^{-3} s^{-1}, the dissipation energy increases and further decreases. An increase in the residual strain is also observed at low-cycle fatigue of the NiTi wire under uniaxial tension (Moumni et al., 2009).

Therefore, in order to develop the behaviour models of structural elements and devices made of SMA, it is necessary to study the regularities of changing stress- and strain-based parameters, which characterise the functional properties.

The effect of loading range on the stress–strain curve, residual strain and dissipation energy of NiTi alloy was studied.

2. MATERIAL AND EXPERIMENTAL SETUP

Tests were carried out on commercial NiTi bar (8 mm, Wuxi Xin Xin glai Steel Trade Co., Ltd.).

The influence of the cyclic loading on the functional properties of Ni55,8Ti44,2 in the form of the rod of 8 mm in diameter was

DOI 10.2478/ama-2019-0013

studied. The chemical alloy composition stated in the certificate is 55.78% Ni; 0.005% Co; 0.005% Cu; 0.005% Cr; 0.012% Fe; 0.005% Nb; 0.032% C; 0.001% H; 0.04% O; 0.001% N; 44.12% Ti.

Phase transformation temperatures were identified using differential scanning calorimetry (DSC) by Q1000 TAI (Iasnii and Yasniy, 2018; Iasnii and Junga, 2018). Mechanical properties and influence of cyclic loading on the functional properties were studied at a temperature of 0°C under the uniaxial tension. Cylindrical specimens with a diameter of 4 mm and a gage length of 12.5 mm were machined from 8-mm rod (Iasnii and Yasniy, 2018). The tests were carried out on servo-hydraulic testing machine STM-10 (Yasniy et al., 2005) with automated control and data acquisition system under constant maximal crosshead displacement and sinusoidal load with a frequency of 0.5 Hz. Displacement ratio was $r = S_{min}/S_{max} = 0$, where S_{min}, S_{max} were the minimum and maximum value of crosshead displacement, respectively. During the tests at the first and following cycles at $S_{min} = 0$, the stress in the specimens becomes zero. This was provided by the structural feature of the grips. Force, crosshead displacement and elongation of the gauge length were recorded during the testing. Longitudinal strain was measured by Bi-06-308 extensometer produced by Bangalore Integrated System Solutions (BISS); maximum error did not exceed 0.1%. The crosshead displacement was determined by inductive Bi-02-313 sensor with an error not more than 0.1%. The tests were carried out in the chamber filled with ice and ice water. This provided the constant temperature of 0°C measured by chromel–alumel thermocouple mounted on the sample with an error not more than 0.5°C.

Literature data analysis shows that water has complex influence on the NiTi alloy fatigue behaviour. The low-cycle fatigue of NiTi SMA under the rotating–bending fatigue tests in air, in water and in silicone oil was studied by Tobushi et al. (2000). The influence of corrosion fatigue in water did not appear in the region of low-cycle fatigue. The fatigue life of NiTi alloy at an elevated temperature in air coincides with the fatigue life at the same elevated temperature in water.

No clear influence of the air or water environment on the fatigue life of NiTi alloys was found (Matsui et al., 2004). Rotating-bending fatigue tests were carried out in air and in water at room temperature and at 303 K.

Three conventional super-elastic NiTi instruments and two new CM wire instruments were subjected to rotational bending at the curvature of 35° in air and deionised water by Shen et al. (2012). The fatigue life of CM instruments was longer in water than in air.

Instruments of one brand of NiTi engine file were subjected to rotational bending either in air or under water and the number of revolutions to fracture was recorded using an optical counter and an electronic break-detection circuit by Cheung and Darvell (2007). A significant effect of the environmental condition on the LCF life was observed, water being more detrimental than air.

3. RESULTS AND DISCUSSION

The DSC (Fig. 1) curves show the martensitic–austenitic and austenitic–martensitic phase transformations occurring in SMA during the heating and cooling cycles relatively (Iasnii and Yasniy, 2018). Whilst heating the sample, the phase transformation takes place in the temperature range between −60.5°C and −38.7°C, and the transition temperature is −45.7°C. The reverse phase transformation during cooling is between −95.9°C and −69.4°C.

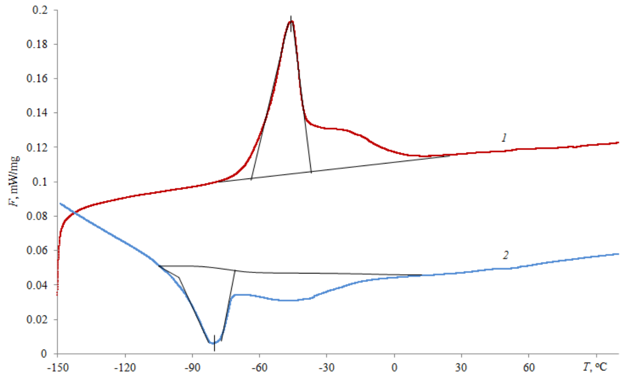

Fig. 1. Enthalpy change during phase transformation in SMA whilst heating (1) and cooling (2) (Iasnii and Yasniy, 2018)

Mechanical properties were determined according to ASTM F2516-14 standard, (2014) in ice water at 0°C which is higher than the austenitic finish temperature (A_f = −38.7°C): yield strength, $\sigma_{0,2}$ = 447 MPa, ultimate tensile strength, σ_{UTS} = 869 MPa (Iasnii and Yasniy, 2018).

Typical hysteresis loops for different values of the stress range and different number of load cycles (*N* = 1, 10, 20 cycles) are shown in Figure 2.

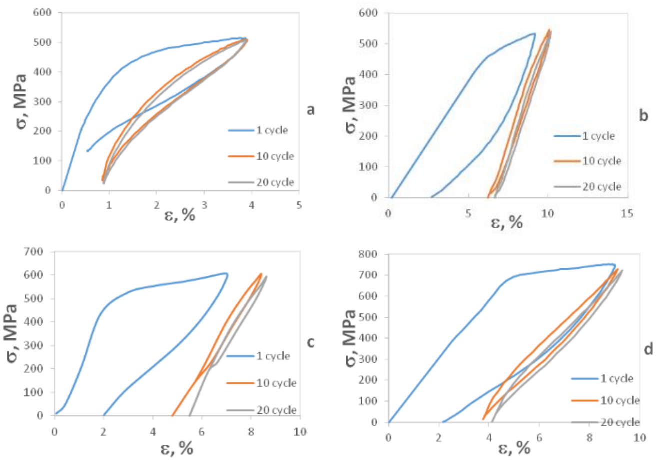

Fig. 2. Typical hysteresis loops for 1, 10 and 20 load cycles and stress range $\Delta\sigma_1$ = 509 MPa (a), 530 MPa (b), 605 MPa (c) and 748 MPa (d)

The dependences of the stress range (Fig. 3a) and the relative stress range (Fig. 3b) on the number of loading cycles at different initial values are shown in Figure 3. During the first cycle, all values of the initial stress range increase, that is, the material is strengthening. Then we can note weakening and stabilising regions followed by the decrease in the stress range. An exception is only for specimen with the initial stress range $\Delta\sigma_1$ = 748 MPa, where the value continuously decreases during testing.

Using the maximum stress related to the first cycle and ignoring the minor (up to 3%) deviation from the initial stress value, we can assume that the stress range remains constant and is equal to $\Delta\sigma_1$ during the testing (Fig. 3b).

DOI 10.2478/ama-2019-0013 acta mechanica et automatica, vol.13 no.2 (2019)

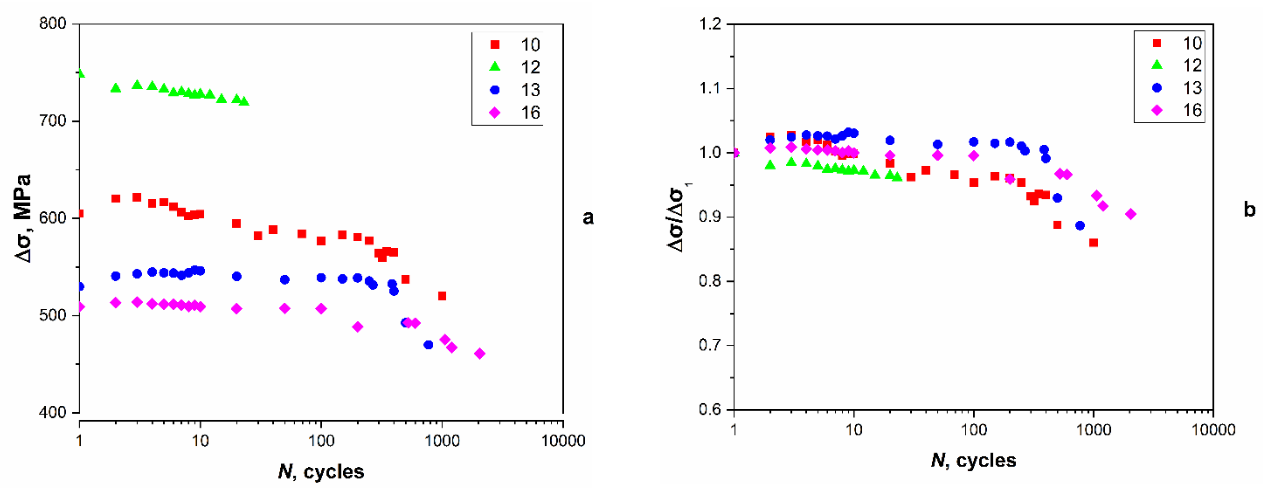

Fig. 3. Dependence of (a) the stress range and (b) the relative stress range on the number of loading cycles. $\Delta\sigma_1$ = 509 MPa (16), 530 MPa (13), 605 MPa (10) and 748 MPa (12). The specimen number is indicated in brackets

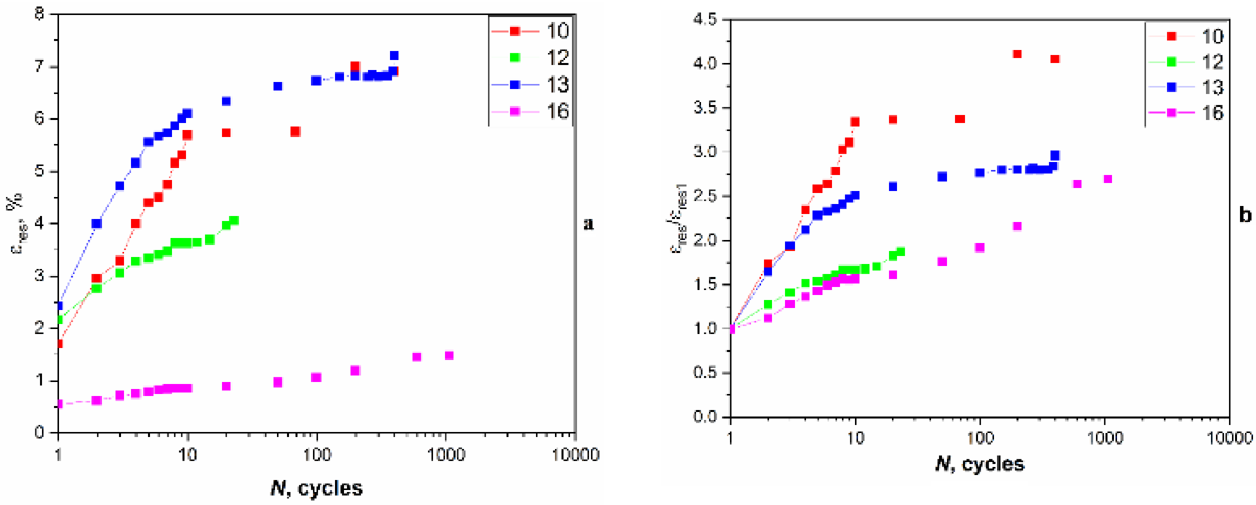

Fig. 4. Dependence of (a) the residual strain and (b) the relative residual strain on the number of loading cycles. $\Delta\sigma_1$ = 509 MPa (16), 530 MPa (13), 605 MPa (10) and 748 MPa (12)

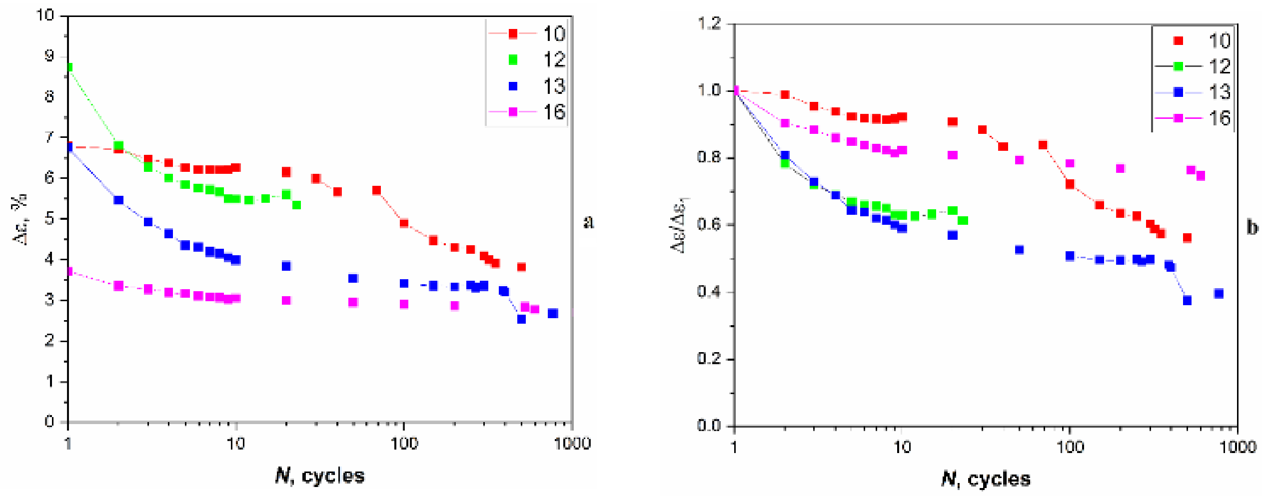

Fig. 5. Dependence of (a) the strain range and (b) the relative strain range on the number of loading cycles. $\Delta\sigma_1$ = 509 MPa (16), 530 MPa (13), 605 MPa (10) and 748 Mpa (12)

The functional properties of the pseudoelastic SMA can be characterised by residual strain. With the increase in the loading cycles, the residual strain (Fig. 4.a) and the relative residual strain $\bar{\varepsilon_r} = \varepsilon_r/\varepsilon_{r1}$, that is, the residual stress divided by the residual strain in the first loading cycle (Fig. 4b), grow. An increase in the stress range from 509 to 605 MPa increases the residual strain

DOI 10.2478/ama-2019-0013

that leads to the degradation of pseudoelasticity. However, with the further increase in the initial stress range to $\Delta\sigma_1$ = 740 MPa, the dependence of residual deformation on the number of loading cycles shifts below the same dependence for $\Delta\sigma_1$ = 605 MPa (Fig. 4a). The relative dependence of residual strain on the loading cycles' number at $\Delta\sigma_1$ = 740 MPa is the same as that at $\Delta\sigma_1$ = 509 MPa (Fig. 4b). The indicated inversion from the general law could be due to the fact that the strain range at $\Delta\sigma_1$ = 740 MPa in the first cycle is 8.7% that exceeds the maximum strain under which the superelastic effect is still visible.

The functional properties of the superelastic SMA can also be characterised by the strain range per cycle.

The dependences of residual strain (Fig. 5a) and relative residual strain (Fig. 5b) on the number of loading cycles for different stress range values in the first load cycle are shown in Figure 5.

For all values of the initial strain range during the first 10 loading cycles, a rapid decrease in the strain range, followed by the stabilisation area of strain range, or its less intensive reduction was observed.

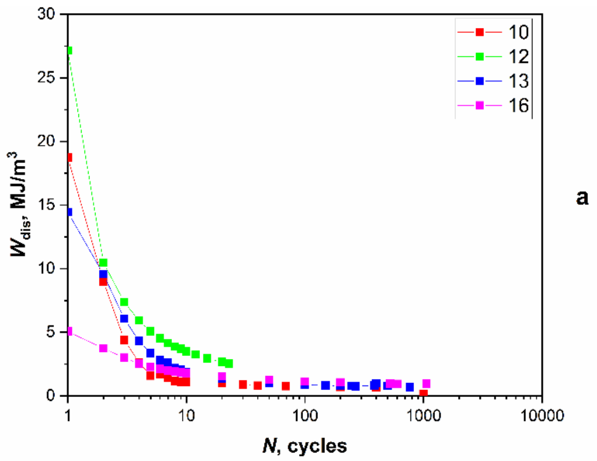

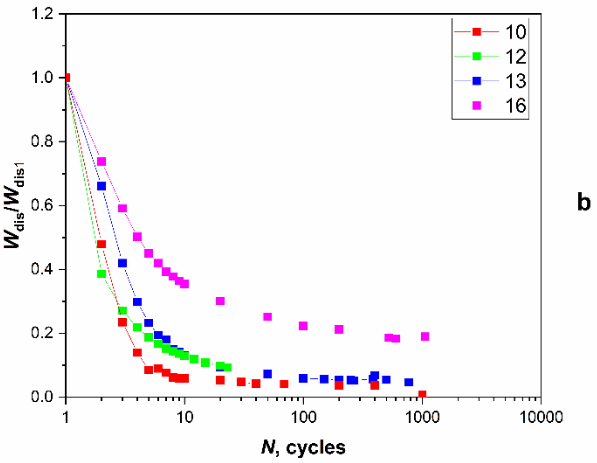

Fig. 6. Dependence of (a) dissipation energy and (b) relative dissipation energy on the number of load cycles. $\Delta\sigma_1$ = 509 MPa (16), 530 MPa (13), 605 MPa (10) and 748 MPa (12)

With the increasing in the stress range from 509 to 748 MPa, the strain range in the first cycle increase from 3.7% to 7.7% (Fig. 5b).

In general, the difference of strain range at a different stress level decreases with the increases in the number of loading cycles.

Dependences of dissipation energy and relative dissipation (energy) on the loading cycle number are given in Figure 6. For all values of the initial stress range as well as in the case of strain range, during the first 10–20 load cycles, a rapid decrease in the dissipation energy and relative dissipation energy passing into the stabilization region is observed. As the stress range increases in the first load cycle from 509 to 740 MPa, the value of the dissipation energy at the initial deformation stage increases up to 20 cycles (Fig. 6a) and that of the relative dissipative energy decreases before the failure specimens (Fig. 6b). The experimental values of the dissipation energy on the loading cycles' number (at N > 10 cycles) that are invariant to the stress range, which does not exceed the stress levels at which the martensite transformation completes, are located within the same scatter range and can be described by a single dependence.

The loss coefficient η, an effective parameter for measuring the device damping ability, is defined as the specific damping capacity per radian of the damping cycle (Pan and Cho, 2008):

$$\eta = \Delta W / (\pi(2W - \Delta W)) \quad (1)$$

where ΔW is the dissipated energy and W is the maximum potential energy of damping element.

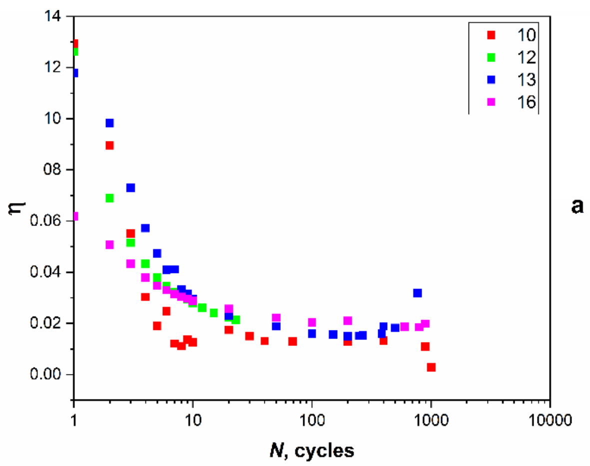

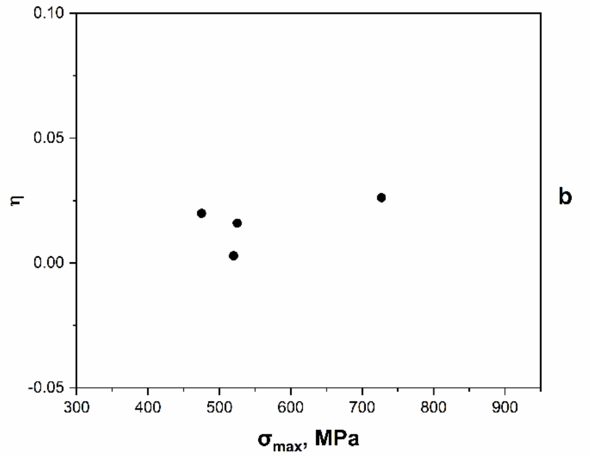

Fig. 7. The dependence of the loss coefficient on (a) the number of load cycles and (b) the stress range at $N = 0.5N_f$ – b. $\Delta\sigma_1$ = 509 MPa (16), 530 MPa (13), 605 MPa (10), 748 MPa (12)

At the initial stage of loading, with the increase in the cycles' number, the loss coefficient of NiTi alloy decreases, provided that the fastest drop in the loss coefficient is observed during the first 10 load cycles (Fig. 7a).

After 30–40 load cycles, the loss coefficient curves reach the plateau without regard to the applied value, the experimental points are located within the range of one scatter band of 0.01–0.02 (Fig. 7a).

According to the results of experimental investigations, the diagrams of cyclic alloy deformation for lifetime (Fig. 8) were built.

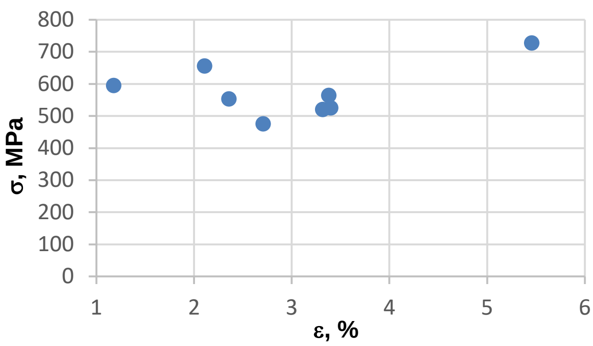

Fig. 8. Stress–strain curves of pseudoelastic NiTi alloy under cyclic loading for lifetime 0.5 N_f

These curves are important for the refined calculation of the stress–strain state of the structural elements made of SMA subjected to cyclic loading, as well as for the recalculation of power criteria of fatigue failure into deformation criteria and vice versa.

4. CONCLUSIONS

At the temperature higher than the temperature of the SMA, martensitic–austenitic transformation was completed under the conditions of controlled grips shifting; the dependence of the strain range on the cyclic operating time in general can be characterised by areas of strengthening, weakening and stabilisation.

The rapid decrease in the strain range observed during the first 10 loading cycles, without regard to the initial value of the strain range, is replaced by the stabilisation area that changes into the area of continuous strain range reduction of the extent of the strain resulting in specimen fracture. The residual strain and the strain range increase with the increase in the stress range for the same number of loading cycles.

Dissipation energy is invariant to the loading cycles' number at $N > 20$ cycles and to the strain range that does not exceed the martensite finish stress level, is within the same scatter band and can be described by the single dependence. With the stress range growth at $N < 20$ cycles from 509 to 740 MPa, the value of dissipation energy increases and that of the relative dissipation energy decreases before the failure specimens.

Loss coefficient, which characterizes material damping ability, significantly decreases during the first 10 loading cycles and remains practically unchanged up to the failure specimens. At the stabilisation area, the loss coefficient is almost non-sensitive towards the strain range.

REFERENCES

1. **Abeyaratne R., Kim S.-J.** (1997), Cyclic effects in shape-memory alloys: a one-dimensional continuum model, *International Journal of Solids and Structures*, 34(25), 3273-3289.
2. **Auricchio F., Boatti E., Conti M.** (2015), SMA Biomedical Applications, *Shape Memory Alloy Engineering*, Chapter 11, 307-341.
3. **Auricchio F., Marfia S., Sacco E.** (2003), Modelling of SMA materials: training and two way memory effect, *Computers & Structures*, 81, 2301-2317.
4. **ASTM F2516-14** (2014), Standard Test Method for Tension Testing of Nickel-Titanium Superelastic Materials.
5. **Chen Q., Thouas G.A.** (2015), Metallic implant biomaterials, *Materials Science and Engineering: R: Reports*, 87, 1-57**.**
6. **Cheung G.S.P., Darvell B.W.** (2007), Fatigue testing of a NiTi rotary instrument. Part 1: strain-life relationship, *International Endodontic Journal*, 40(8), 612-618.
7. **Eggeler G., Hornbogen E., Yawny A., Heckmann A., Wagner M.** (2004), Structural and functional fatigue of NiTi shape memory alloys, *Materials Science and Engineering: A*, 378(1-2), 24-33.
8. **Gamaoun F., Skhiri I., Bouraoui T., Ben Zineb T**. (2014), Hydrogen effect on the austenite–martensite transformation of the cycled Ni–Ti alloy, *Journal of Intelligent Materials Systems and Structures*, 25(8), 980-988.
9. **Hsu W.N., Polatidis E., Šmíd M., Van Petegem S., Casati N., Van Swygenhoven H.** (2019), Deformation and degradation of superelastic NiTi under multiaxial loading, *Acta Materialia*, 167, 149-158.
10. **Iasnii V., Junga R.** (2018), Phase Transformations and Mechanical Properties of the Nitinol Alloy with Shape Memory, *Materials Science*, 54(3), 406-411.
11. **Iasnii V., Nykyforchyn H., Tsyrulnyk O., Student O. (2019),** Specific features of deformation of the nitinol alloy after electrolytic hydrogenation, Materials Science, 54(4), 582-588.
12. **Iasnii V., Yasniy P., Lapusta Y., Shnitsar T.** (2018), Experimental study of pseudoelastic NiTi alloy under cyclic loading, *Scientific Journal of TNTU*, 92(4), 7-12.
13. **Isalgue A., Lovey F., Terriault P., Martorell F., Torra R., Torra V.** (2006), SMA for Dampers in Civil Engineering, *Materials Transactions*, 47(3), 682–690.
14. **Kan Q., Yu C., Kang G., Li J., Yan W.** (2016), Experimental observations on rate-dependent cyclic deformation of superelastic NiTi shape memory alloy, *Mechanics of Materials*, 97, 48-58.
15. **Kang G., Kan Q., Yu C., Song D., Liu Y.** (2012), Whole-life transformation ratchetting and fatigue of super-elastic NiTi Alloy under uniaxial stress-controlled cyclic loading, *Materials Science and Engineering: A*, 535(15), 228-234.
16. **Matsui R., Tobushi Y., Furuichi Y., Horikawa H.** (2004), Tensile Deformation and Rotating-Bending Fatigue Properties of a Highelastic Thin Wire, a Superelastic Thin Wire, and a Superelastic Thin Tube of NiTi Alloys, *Journal of Engineering Materials and Technology***,** 126(4), 384.
17. **Menna C., Auricchio F., Asprone D.** (2015), *Shape Memory Alloy Engineering*, Elsevier.
18. **Mohd J., Leary M., Subic A., Gibson M.** (2014), A review of shape memory alloy research, applications and opportunities, Materials & Design, 56, 1078-1113.
19. **Morgan N.B.** (2004) Medical shape memory alloy applications - the market and its products, *Materials Science and Engineering: A*, 378(1-2), 16-23.
20. **Moumni Z., Zaki W., Maitournam H.** (2009), Cyclic Behavior and Energy Approach to the Fatigue of Shape Memory Alloys, *Journal of Mechanics of Materials and Structures*, 4(2), 395-411.
21. **Nespoli A., Besseghini S., Pittaccio S., Villa E., Viscuso S.** (2010), The high potential of shape memory alloys in developing miniature mechanical devices: A review on shape memory alloy mini-actuators. *Sensors and Actuators A: Physical*, 158, 149-160.
22. **Ozbulut O.E., Hurlebaus S., Desroches** R. (2011), Seismic response control using shape memory alloys: A review, *Journal of Intelligent Material Systems and Structures*, 22(14), 1531-1549.
23. **Pan Q., Cho C.** (2008), Damping property of shape memory alloys, *The 17th International Metallurgical and Materials Conference METAL*, 1-5.

24. **Piedboeuf M.C., Gauvin R.** (1998), Damping behaviour of shape memory alloys: strain amplitude, frequency and temperature effects, *Journal of Sound and Vibration*, 214(5), 885-901.
25. **Predki W., Klönne M., Knopik A.** (2006), Cyclic torsional loading of pseudoelastic NiTi shape memory alloys: Damping and fatigue failure, *Materials Science and Engineering: A*, 417(1-2), 182-189.
26. **Qiu C., Zhu S. (2017),** Shake table test and numerical study of self-centering steel frame with SMA braces, *Earthquake Engineering & Structural Dynamics*, 46(1), 117-137.
27. **Shen Y., Qian W., Abtin H., Gao Y., Haapasalo M.** (2012), Effect of environment on fatigue failure of controlled memory wire nickel-titanium rotary instruments, *Journal of Endodontics*, 38(3), 376-380.
28. **Sun L., Huang W.M., Ding Z., Zhao Y., Wang C.C., Purnawali H., Tang C.** (2012), Stimulus-responsive shape memory materials: A review, *Materials & Design*, 33, 577-640.
29. **Tanaka K., Nishimura F., Hayashi T., Tobushi H., Lexcellent C.** (1995), Phenomenological analysis on subloops and cyclic behavior in shape memory alloys under mechanical and/or thermal loads, *Mechanics of Materials*, 19(4), 281-292.
30. **Tobushi H., Nakahara T., Shimeno Y., Hashimoto T.** (1999), Low cycle fatigue of TiNi shape memory alloy and formulation of fatigue life, Journal of Engineering Materials and Technology, 122(2), 186-191.
31. **Torra V., Isalgue A., Auguet Sangra C., Carreras G.** (2012), The SMA: An Effective Damper in Civil Engineering that Smoothes Oscillations, *Materials Science Forum*, 706-2015, 2020-2025.
32. **Yasniy P., Hlado V., Hutsaylyuk V., Vuherer T.** (2005), Microcrack initiation and growth in heat-resistant 15Kh2MFA steel under cyclic deformation, *Fatigue & Fracture of Engineering Materials & Structures*, 28(4), 391-397.
33. **Yasniy P., Kolisnyk M., Kononchuk O., Iasnii V.** (2017), Calculation of constructive parameters of SMA damper, *Scientific Journal of TNTU*, 88(4), 7-15.

DOI 10.2478/ama-2019-0014 acta mechanica et automatica, vol.13 no.2 (2019)

EXPERIMENTAL EVALUATION OF THE TRACTIVE EFFORT OF THE CHAIN CONVEYOR DURING BOOK BLOCK SPINE PROCESSING BY CYLINDRICAL MILLING CUTTER AT PERFECT BINDING

Oleh KNYSH*, Ivan REHEI*, Nazar KANDIAK*, Serhij TERNYTSKYI*

* Faculty of Computer Printing Engineering, Department of Computerized Complexes of Printing and Packaging Industries
Ukrainian Academy of Printing, Lviv, 79020, Pid Goloskom street, 19, Ukraine

knolehb@gmail.com, regey.ivan@gmail.com, kandyak.nazar@gmail.com, serhij86@gmail.com

received 16 May 2018, revised 14 June 2019, accepted 19 June 2019

Abstract: The article reports on a device for book block spines processing that was designed and assembled on a perfect binding machine Trendbinder. The article shows workability of designed device. The authors have developed a methodology for the experimental study of the tractive effort of chain conveyors by technological load, the wireless module for data measurement and software for its processing. Extensive coverage is given to experimental research of the tractive effort of chain conveyors during book block spine processing depending on book block velocity, type of paper from which they are made and setting angle of cylindrical milling cutter relatively to direction of book blocks movement. The authors have examined the change in the tractive effort. The article experimentally confirms that sluggishness of chain drive causes vibration of the tractive effort. This effect can be observed during free-running movement of chain with carriers of perfect binding machine as well as during technological load influence. The article describes that between research parameters the setting angle of cylindrical milling cutter has the main impact relatively on the direction of book blocks movement.

Key words: tractive effort, cylindrical milling cutter, chain conveyor, book block, perfect binding

1. INTRODUCTION

Perfect binding of book block is the most common way of books and magazines binding. This is due to a number of factors amongst which the main is low cost. Along with that, it has characteristic well-known drawback: sufficient strength and durability of binding cannot be achieved always (Kipphan, 2001). Quality improvement of perfect bound book blocks carried out mainly in two directions: improvement of adhesives and the spine preparation before its applying (Knysh et al., 2019).

The spine preparation before applying adhesive provides for spine folds cutting and its processing by the spine microgeometry ‘development’ and applying additional grooves for better glue ingress. The development.of means of block spine cutting and processing is on use of tools without any electromechanical drive. As an example, multi-blade cutting tools (Vatuljak and Ju, 2018), screw with sided aggravation of helical cutting edge (Poliudov and Knysh, 2014) and cylindrical milling cutter (Viniarskyi and Knysh, 2003) can be considered. It is apparent that in all cases, technological load causes the increase in the tractive effort, which effects on conveyor drive power. In view of the outlined problem, it can be argued the actuality of researches directed on the experimental evaluation of tractive effort during book block spine processing by cylindrical milling cutter.

Analysis of previous research.

Tokarchuk (2014) studied the change in the tractive effort during the use of conveyor for granular materials with horizontal, curved and vertical sections. The author considered the conveyor as a mean of product transportation, thus the influence of technological loads on the tractive effort is absent. Pilipenko and Poluyan (2015) analysed the influence of sprocket and chain material (metal and plastics) on dynamics of chain conveyor. The experimental researches have defined the average value of dynamic chain loads, which gave an opportunity to calculate drive power, chose pitch and number of chain. Udovytskyi and Soltys (2017) have developed recommendations for reducing the negative impact of dynamic phenomena on the work of conveyors. They have proposed to minimise forced oscillations by reducing chain pitch or changing chain structure. This practice makes possible to reduce the negative impact of oscillations on the dynamic processes in the conveyor. The research of oscillation processes in the traction units of the chain conveyors (Lazutkyna, 2013) has shown that in the oscillations spectrum there are a frequency of natural free oscillations of the traction unit. Such effect is caused by periodic impact of conveyor roller on guide rail joint of plate conveyors. Senkus et al. (2015) have proposed changing of leading sprocket drive by using combined cam-lever mechanism for nonuniformity minimisation of conveyor links running. The study by Egorov et al. (2015) has identified a method that allows determining the torque and the efficiency of chain drives. This method does not require additional equipment, is more cost-effective and gives an opportunity to evaluate the chain drive efficiency with high measurement rate. In the works by Pereira et al. (2010a, 2010b), they have proposed the methodology of evaluation of the initial positions and velocities of all components of the chain drive that are consistent with the kinematic. The article by James and Johnson (1996) has shown the results of experimental studies of roller chain drives dynamics. They have studied the chain tension during the change of its velocity by use of strain gauges. According to the research results, it has been established that chain dynamics phenomenon increases by increasing its velocity. In addition, they have studied the change in horizontal and vertical resistance force in bearing depending on chain velocity. The article by Ambrosio et al. (1996) has shown a multibody dynamics methodology for the study of roller chain drives. The chain drive mechanisms are described as a planar multibody system. The contact force model includes the geometric contact detection and the contact force evaluation, which in turn includes energy dissipative features resulting from the friction and restitution coefficients terms used in the model. Niels et al. (2016a) have researched kinematic and dynamic model of chain drive and, as a result, received models that provide a basis for analytical and experimental research of roller chain transmissions. The work by Niels et al. (2016b) presents precise and approximate kinematic analysis of chain drive that has been modelled as a quadro-lever mechanism. They have studied kinematic parameters of sprocket rotation and behaviour pattern of its change. Comparative analysis of kinematic research results has shown their proximity to modelling results. These results have given new conceptions about the kinematic characteristics of the chain drive and the impact of the basic structural parameters. For the purpose of theoretical analysis of chain drive, Junzhou et al. (2013) have proposed and have used mechanical models. They have established that teeth quantity and pitch of sprockets have the most impact on chain vibrations. The article has shown the research of external loads impact on chain tension. These modelling results are well consistent with the theoretical results and illustrate the significant impact of pulsed loads on chain tension. The article by Perawat et al. (2018) has shown the results of experimental research of increase in endurance and hardness of roller chain elements. It has been established that improvement of these parameters increases chain lifetime. This ensures better dynamics of chain conveyor during long-term lifetime. In the article by Troedsson and Vedmar (2001), they have exemplified the results of calculations of loads distribution on sprockets of chain transmission, which work with moderate or high velocity. Chain roller position and their impact on dynamics distribution of loads in chain drive have been considered. The article by Kozar (2014) has given the results of experimental research of book block cutting by flat curvilinear knife. The author studied the components of cutting force and transportation force. However, it is noteworthy that track conveyor has been used as a mean of transportation, which is rarely used in perfect binding equipment. In the article by Xu et al. (2010), they have proposed a model that can well simulate the transverse and longitudinal vibration of the chain spans and the torsional vibration of the sprockets. This study can provide an effective method for the analysis of the dynamic characteristics of all the chain drive systems. The kinematic analysis demonstrates that the total length of the chain wrapped around the sprockets generally varies during one-tooth period. Some researchers proposed new structure of chain and sprockets to avoid problems of existed one. Liu et al. (2012) provided a reference for the optimisation design of the structure of the chain and sprocket wheel, through the analysis on the moving velocity and acceleration curve of the chain.

Because of the analysis, we can conclude that in the recent years, considerable research on the chain drive has been done. There are no results concerning the problem of the study of the technological load impact on the tractive effort in the conveyors of perfect binding machines. Therefore, we assume that the study of experimental research of tractive effort during book block spine processing by cylindrical milling cutter is the topical problem.

The aim of the article is to study the tractive effort of chain conveyor of perfect binding machine during book block spine processing by cylindrical milling cutter.

To achieve the aim of the article, we need to determine the following tasks:

- to design, manufacture and assemble the testing bench in perfect binding machine Trendbinder;
- to develop the experimental research methodology of tractive effort on driving chain of perfect binding machine Trendbinder;
- to design and manufacture wireless module for transferring of experimental data and to develop the processing software;
- to study the changing characteristics of the tractive effort during book block spine processing by cylindrical milling cutter;
- to study the impact of book block velocity, paper type from which blocks are made and setting angle of cylindrical milling cutter on the tractive effort.

2. TECHNIQUE AND EXPERIMENTAL TEST BENCH

We have conducted the experimental research on special designed test bench, which had been assembled on perfect binding machine Trendbinder-18 («Muller Martini», Switzerland). Because of this, it is possible to get accurate value of the tractive effort because of the change in studied parameters. Trendbinder-18 is the conveyor type machine. For book blocks transportation, it has 18 carriers that are connected by roller chain with pitch p = 25.4 mm. The axle spacing of transmission is 5,360 mm. Chain conveyor consists of drive R1 and driven R2 sprockets with a radius of 283 mm (Fig. 1). The machine has consecutive assembled units: (1) feeder and jogging stations, (2) cut-off of the folded sheets station, (3) spine processing station, (4) spine processing station by cylindrical milling cutter, (5) main gluing station, (6) infrared drying station (if polyvinyl acetate dispersions are used), (7) side gluing station, (8) back-stripping unit (lining station), (9) cover bonding station, (10) drying unit for PVAD by high-tension current, (11, 12) pressing stations and (13) delivery of bound book block out of machine. The power of the conveyor drive is 5.5 kW.

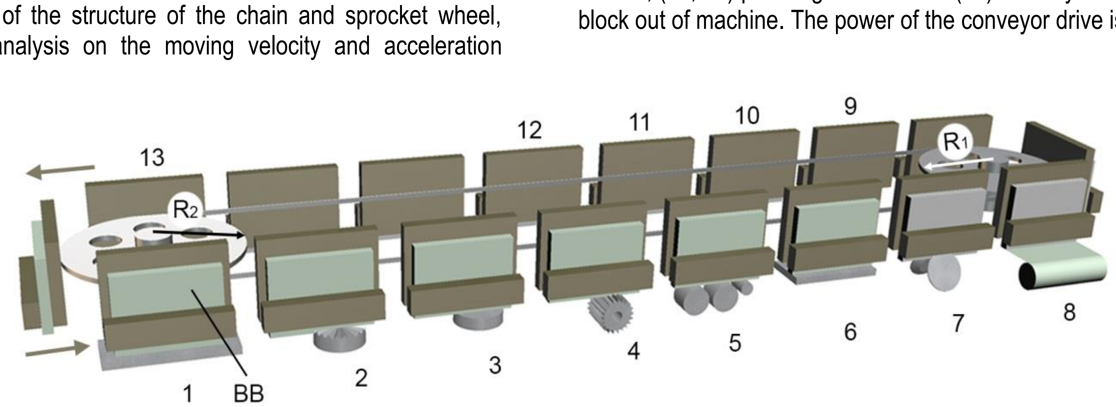

Fig. 1. Principal scheme of perfect binding machine Trendbinder-18

DOI 10.2478/ama-2019-0014 acta mechanica et automatica, vol.13 no.2 (2019)

Experimental test bench (Figs. 2 and 3) consists of cylindrical milling cutter 1 with a tooth pitch of 7 mm, a sharpening angle of 20° and an outer diameter of 50 mm. Milling cutter is fixed on the shaft 2, which freely rotates in the support of support-bracket 3 that is inflexible and fixed to frame 4 of the machine. Book block BB is fixed by moving clamp 5 in carriage 6. Carriage connects by bracket 7 to chain 8 of conveyor. Linear translation of carriage is accomplished on guides 9. Guides 10 additionally press the spine part of book block, which bulges out the carriage.

Book block spine processing passes in a sequence given as follows. Book block that is fixed by moving clamp 5 in carriage 6 after cut-off of the folded sheets (not shown) transports to the cylindrical milling cutter 1. Contacting the spine and cogs of the milling cutter 1 during the movement of the blocks gradually makes incisions on block spine surface (Viniarskyi and Knysh, 2003).

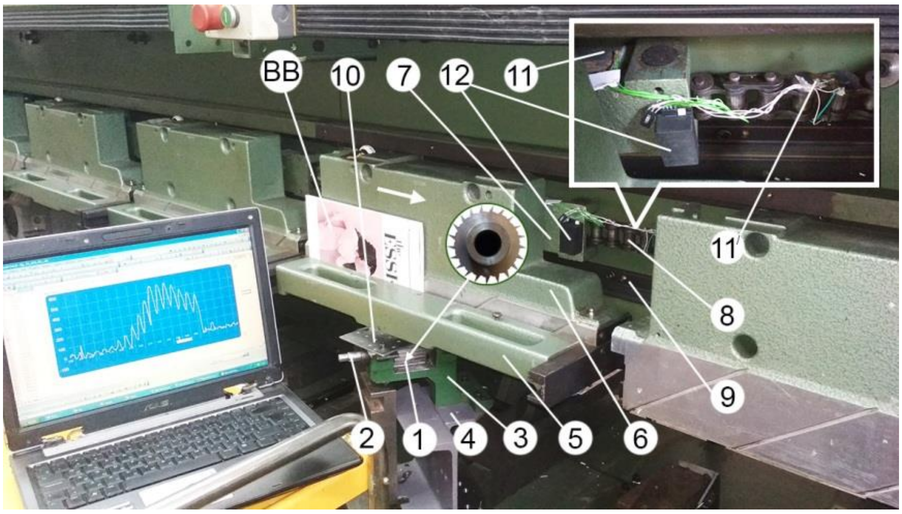

Fig. 2. Photo of the part of perfect binding machine Trendbinder and the experimental test bench

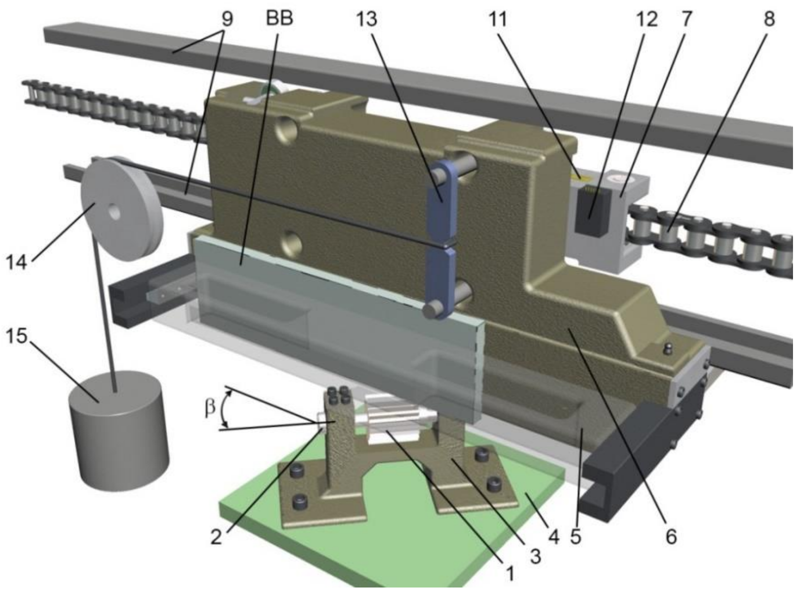

Fig. 3. 3D model of carriage and experimental test bench

For experimental research of tractive effort during book block spine processing by cylindrical milling cutter, we have used the method of strain gauge measurement. For this purpose, four foil resistance strain gauges type N2A-06-T007R-350 with a resistance of 350 Ohm and a base of 150 mm have been used. These strain gauges have been connected into complete bridge connection. We have connected strain gauge bridge to measurement equipment by specially designed module 12 for data processing and its wireless transferring. Such principle of wireless data transferring has been used because of carrier movement by a closed trajectory at a comparatively long distance (about 10 m) that makes data transferring by wire impossible.

Module 12 of wireless data transferring consists of three elements: 24-digit analogue-to-digital converter (ADC) H×711 with integrated amplifier (gain 128 times), microcontroller ATmega 328P and Bluetooth unit HC05. The principle of module 12 works as follows. Microcontroller makes data processing from ADC and its transfer by UART protocol to Bluetooth HC05 unit, which transfers the data by wireless method. For wireless data reception by Bluetooth v2.0 + EDR protocol from module 12, we have used the programme IVT BlueSoleil that receives data and creates virtual COM port and transfers data there.

For data reception and mapping in real time, we have created in spreadsheet MS Excel macros in Visual Basic for applications that get data from microcontroller by virtual COM port, interpret and write data into appropriate cells of spreadsheet without any other software. Final data processing and visualisation were made by inbuilt and own functions of MS Excel.

For matching between indexes of ADC and real values of loads, we have made calibration. For this purpose, we have inflexibly fixed the drive sprocket of chain conveyor and have connected special plate 13 (Fig. 3) to which a reference mass is applied by means of a rope through block 14. For recording of calibration diagram (Fig. 4), loads with different masses 15 were changed.

Due to fact that different masses have been applied, we have used next dependence for data conversion of ADC into effort values:

$$F = n_0 \cdot K, \tag{1}$$

where n_0 is the starting value of ADC, n is the current value of ADC and K is the conversion ratio of ADC values into loads, which is determined by the formulae:

$$K = \frac{(m \cdot g)}{n_t}, \tag{2}$$

where n_t is the quantity of ADC values that corresponds to change of applied mass.

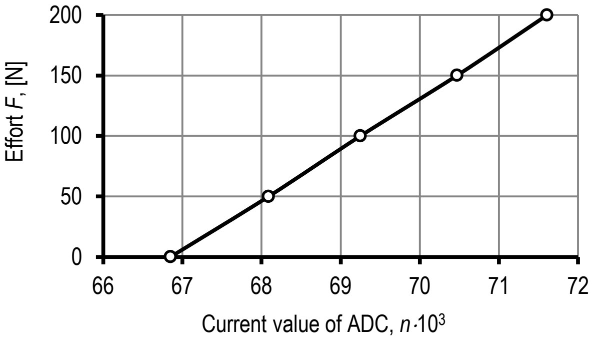

Fig. 4. Calibration diagram

Calibration diagram (Fig. 4) helps to transform values of ADC into indexes of tractive effort values. Here, the load F is laid off along the X-axis, which had been applied to the carriage, and the value n of ADC is laid off along the Y-axis. As seen from the diagram, we have got linear dependence that proves the correctness of strain gauges installation and possibility of getting trustworthy data of experimental research. At the first stage of research, we have used strain gauges 11′ (Fig. 2) on chain link and have connected to module of data processing and transferring. However, this method of tractive effort determination cannot give correct values. It can be explained by the fact that in case of such an arrangement of strain gauges, we have got parametric oscillations that had been raised by resistance effort and carriage mass. At the same time, it was impossible to distinguish tractive effort caused by technological loads. The dependence of tractive effort on time in case of strain gauges arranged on chain link at the book block velocity 0.3 m/s is shown as an example in Figure 5.

As we see (Fig. 5), oscillations peak of tractive effort of chain at idle on intervals t = 0.00–1.38 s and t = 2.02–2.95 s is round 350–400 N. On the interval of working stroke (t = 1.35–2.05 s), we can observe an increase in the tractive effort. However, the character of its change is chaotic and does not reproduce the real value of technological loads on conveyor drive.

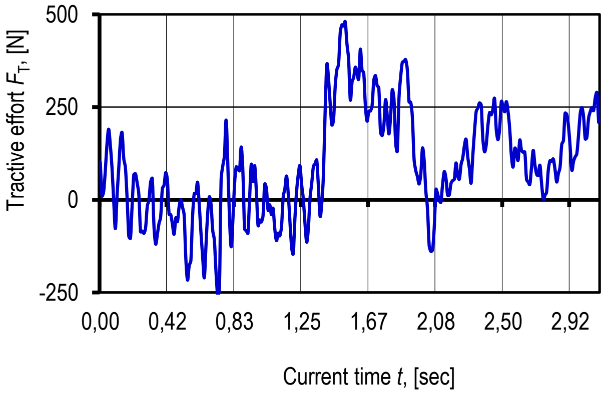

Fig. 5. Diagram of tractive effort dependence on time in case of strain gauges arrangement on connecting chain link

For the aim of avoidance of such a drawback, we have performed new run of experimental research. This time we have arranged strain gauges 11 (Fig. 2) on bracket 7, which connects carriage 6 to chain 8. This has given an opportunity to avoid the impact of inertial loads of conveyor and to determine the tractive effort directly on carriage with book block.

3. RESULTS OF EXPERIMENTAL RESEARCH

For experimental research of tractive effort, we have used book blocks format 60x84/8 with 20mm of thickness made of five types of paper: printing (55 g / m2), offset (70 g / m2), offset (75 g / m2), coated (85 g / m2) and coated (120 g / m2).

The graphical dependence $F_T = f(t)$ of tractive effort on period of spine processing by cylindrical milling cutter with the book block velocity V = 0.3 m/s and the setting angle of cylindrical milling cutter β = 45° is shown in Figure 6. The diagram had been taken when strain gauges were stuck on bracket that connects the carrier and the chain. Comparative analysis of dependencies, which are shown in Figures 5 and 6, shows more accurate character of tractive effort change in second case. There has been minimal impact of vibrations caused by inertia of conveyor on the tractive effort change. The amplitude of tractive effort oscillations at idle without technological loads is minimal and is 50–70 N.

We have conditionally divided the graphical dependence on five segments:

- segment I – carrier idle;
- segment II – smooth increase of tractive effort;
- segment III – maximal value of tractive effort;
- segment IV – tractive effort decrease;
- segment V – carrier idle.

As we can see from segments I and V of carrier at idle oscillations, period of tractive effort for book blocks velocity V = 0.3 m/s is about 0.06 s. Therewith, the constancy of oscillation period can be observed even on segments II–IV but with technological loads superposition.

Segment II shows gradual teeth incision of cylindrical milling cutter into book block spine. At the same time, the resistance to the carriage with the book block movement is created, which causes the gradual decrease in gaps of conveyor and, as a consequence, the increase in the tractive effort to the maximum value. In segment III, tractive effort reaches the maximum value and constant character, which can be explained by final decrease in gaps in conveyor. Character of tractive effort change in segment IV, as we think, is caused by the decrease in longitudinal stiffness of book block in the end of cylindrical milling cutter interaction with spine. In addition, the decrease in simultaneously used teeth quantity of milling cutter and contact line between teeth and spine has an influence on such result.

In addition, we studied the impact of book block velocity on tractive effort. Appropriate results are shown in Figure 7. Book block velocity has discretely changed and has been 0.3, 0.6, 0.8 and 1.2 m/s.

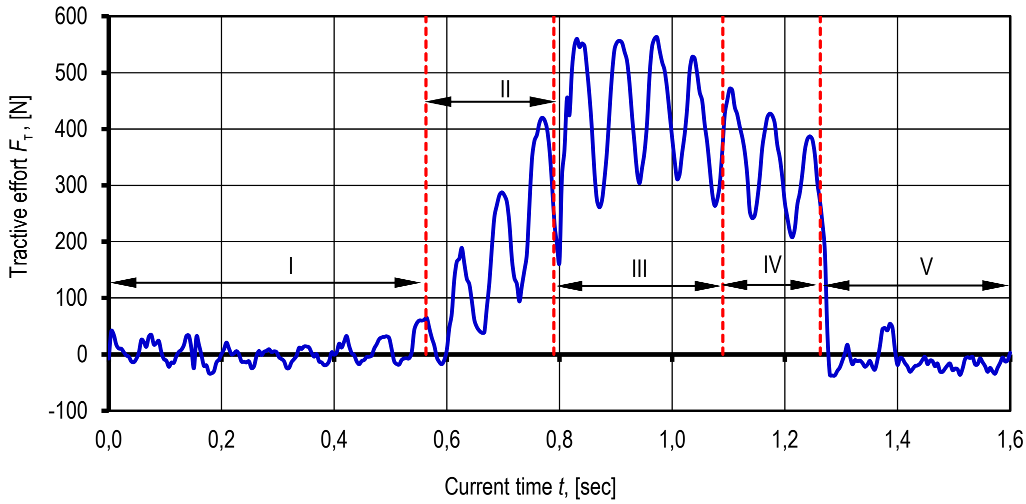

Fig. 6. Diagram of tractive effort dependence on spine processing period

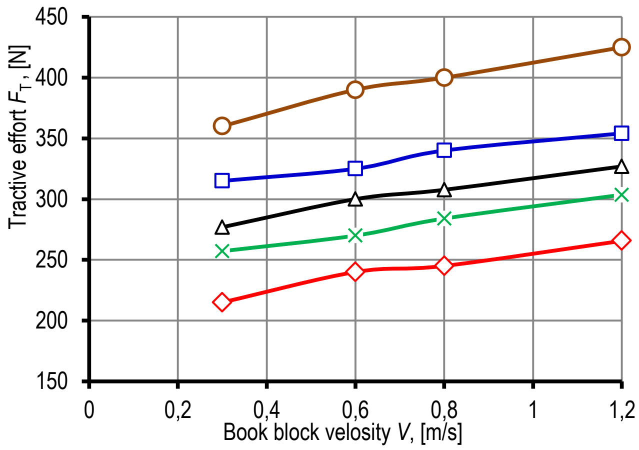

Fig. 7. Diagram of tractive effort dependence on velocity of book block made of paper: ◊ printing (55 g/m^2), × offset (70 g/m^2), ∆ offset (75 g/m^2), □ coated (85 g/m^2), ○ coated (120 g/m^2)

As we can see from the research result, increase in the book block velocity insignificantly increases the tractive effort increase. For example, for coated paper (120 g/m^2), the increase in book block velocity by 4 times from 0.3 to 1.2 m/s increases the tractive effort by 1.25 times from 360 to 450 N. We should also note that an increase of 1 m^2 of paper mass also increases tractive effort because of greater technological loads during processing of 'heavier' type of paper and as consequences higher value of tractive effort.

The results of tractive effort research depend on the setting angle of cylindrical milling cutter, which have been shown in Figure 8. Experimental research has been held for five book blocks made of five paper types. The setting angle of milling cutter has changed discretely and has been 15°, 30°, 45° and 60°. As we can see from the results, increasing the setting angle of milling cutter decreases the tractive effort. Such a tendency is logical and can be explained by the decrease in contact line between milling cutter teeth and book block spine. Because of research, we can state that rational setting angle of cylindrical milling cutter should be 40°–60° because of the decrease in the tractive effort. However, in this case, the defining criteria of book block quality are the stiffness and durability of perfect bound, which was the subject of other studies.

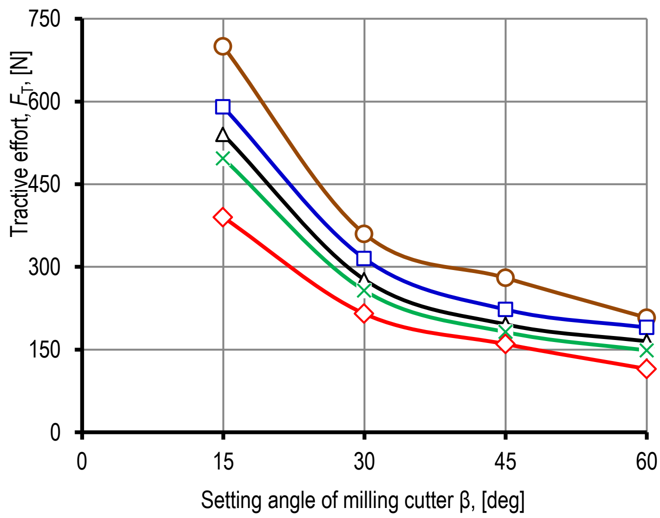

Fig. 8. Diagram of tractive effort dependence on the setting angle of cylindrical milling cutter for paper: ◊ printing (55 g/m^2), × offset (70 g/m^2), ∆ offset (75 g/m^2), □ coated (85 g/m^2), ○ coated (120 g/m^2)

4. CONCLUSION

1. The experimental test bench for research of book blocks spine processing by a cylindrical milling cutter without an electromechanical drive has been designed, manufactured and

mounted on a Trendbinder perfect binding machine. The device's serviceability has been checked in conditions as close as possible to the production.
2. The method of experimental research of tractive effort on a Trendbinder perfect binding machine has been created, which provides the method of strain gauge measurement.
3. The module for wireless data transferring has been designed and manufactured, and special software has been created.
4. The change character of tractive effort of chain conveyor in perfect binding machine has been studied when a machine is idle and during spine processing by cylindrical milling cutter. The tractive effort changes cyclically, which is a consequence of inertia of chain drive and nonuniformity of chain with carrier velocity.
5. Increasing the book blocks transportation velocity by 4 times from 0.3 to 1.2 m/s increases the tractive effort by 1.25 times. The increase in 1 m^2 of paper mass also increases the tractive effort because of the greater resistance to transportation. Increasing the setting angle of milling cutter from 15° to 60° decreases the tractive effort by about 3.5 times. Such a tendency is logical and can be explained by the decrease in contact line between milling cutter teeth and book block spine.

REFERENCES

1. **Ambrosio J., Malça C. Ramalho A.** (2016), Planar roller chain drive dynamics using a cylindrical contact force model, *Mechanics Based Design of Structures and Machines*, 44(1-2), pp. 109–122.
2. **Egorov A., Kozlov K., Belogusev V.** (2015) A method for evaluation of the chain drive efficiency*, Journal of Applied Engineering Science,* 13(4), 277-282
3. **Fuglede N., Thomsen J.J.** (2016 B), Kinematics of roller chain drives – Exact and approximate analysis, *Mechanism and Machine Theory*, 100, 17-32.
4. **Fuglede N., Thomsen J.J.**, (2016 A), Kinematic and dynamic modeling and approximate analysis of a roller chain drive*, Journal of Sound and Vibration*, 366, 447-470.
5. **James C. Conwell, G.E. Johnson** (1996), Experimental investigation of link tension and roller-sprocket impact in roller chain drives, *Mechanism and Machine Theory*, 31(4), 533-544.
6. **Junzhou Huo, Shiqiang Yu, Jing Yang and Tao Li**, (2013), Static and Dynamic Characteristics of the Chain Drive System of a Heavy Duty Apron Feeder, *The Open Mechanical Engineering Journal*, 7, 121-128.
7. **Kipphan, H.** (2001), *Handbook of Print Media: Technologies and Production Methods*, Berlin: Springer.
8. **Knysh O., Rehei I., Ternytskii S., Kandiak N., Behen P.** (2019): Experimental researches of book blocks spine processing by cylindrical milling cutter during perfect binding, *Australian Journal of Mechanical Engineering*, DOI:10.1080/14484846.2019.1625102.
9. **Kozar V.** (2014), Methodology of experimental researches of trimming book magazine blocks flat cuttings tools with a curved blade edge profile, *Printing and Publishing*, 4 (68), 26–31 (In Ukrainian).
10. **Lazutkyna N. (2013),** The study of longitudinal dynamics of the chain conveyor belts, *Modern problems of science and education*, 5, pp.1-9 (In Russian).
11. **Liu, Y.X., Zou, S.L., Tang, T., Zhou, Q.W.** (2012), Study on Simulation of the Chain Transmission Mechanism. *Advanced Materials Research*, 591-593, 797-800.
12. **Perawat T., Patiparn N., Pruet K.** (2018), Wear resistance improvement of the roller chain parts at Thai Metro Industry (1973) Co., Ltd, *Materials Today: Proceedings*, 5(3), Part 2, 9431-9439.
13. **Pereira C., Ambrósio J., Ramalho A.** (2010 A), A methodology for the generation of planar models for multibody chain drives. *Multibody System Dynamics,* 24(3), 303-324.
14. **Pereira C., Ambrósio J., Ramalho A.** (2010 B), Implications of Contact Parameters on the Dynamics of Chain Drives. *Key Engineering Materials*, 572, 367-370.
15. **Pilipenko O., Poluyan A.** (2015), Dynamics of three mass chain drive in metal and polymeric implementation, International scientific and practical conference world Science Proceedings of the conference Innovative technologies in science, I, Rost Publishing, Dubai, 6-9 (In Russian).
16. **Poliudov O. M., Knysh O. B.** (2014) Modern tendencies of improvement of facilities and devices for book spine treatment while perfect binding process, *Scientific Papers*, 3(48), 63-68 (In Ukrainian).
17. **Senkus V., Kolomiiets A., Bosak V**. (2015), Synthesis of chain's speed leveling mechanism for conveyor drive, *Upakovka*, 3, 28-31 (In Ukrainian).
18. **Tokarchuk O.** (2014), Results of experimental researches from determination of hauling effort of workings organs of tube conveyer, *Zbirnyk naukovyh prats (galuzeve mashynobuduvannya, budivnytstvo)*, N1, 52-59 (In Ukrainian).
19. **Troedsson I., Vedmar L.** (2001), A method to determine the dynamic load distribution in a chain drive, *Sage journals*, 215, 569-579.
20. **Udovytskyi O., Soltys I.** (2017), The study of dynamic processes during the transportation by chain conveyor. *Scientific Bulletin of UNFU*, 27(4), 144-147 (In Ukrainian).
21. **Vatuljak, Ju. V.** (2018). *Improving the process of book blocks cutting during their circumferential movement,* PhD diss., Ukrainian academy of printing (In Ukrainian).
22. **Viniarskyi S., Knysh O.** (2003), Studying of the method for the relief development on the book block spine for perfect binding of printed. Printing and Publishing, 40, 8-31 (In Ukrainian).
23. **Xu L, Yang Y, Chang Z, Liu J** (2010) Dynamic modeling of a roller chain drive system considering the flexibility of input shaft. *Chin J Mech Eng,* 23(3), 367-374.

DOI 10.2478/ama-2019-0015 acta mechanica et automatica, vol.13 no.2 (2019)

INVESTIGATIONS OF POLYPROPYLENE FOIL CUTTING PROCESS USING FIBER Nb: YAG AND DIODE Nd:YVO4 LASERS

Leon KUKIEŁKA[*], Radosław PATYK[*], Łukasz BOHDAL[*], Wojciech NAPADŁEK[**], Rafał GRYGLICKI[***], Piotr KASPRZAK[***]

[*]Faculty of Mechanical Engineering, Koszalin University of Technology, ul. Racławicka 15-17, 75-620 Koszalin, Poland
[**]Faculty of Mechanical Engineering, Military University of Technology, ul. gen. Sylwestra Kaliskiego 2, 01-476 Warsaw, Poland
[***]PHU Kontakt Rafał Gryglicki, ul. Kalinowa 31. 75-667 Koszalin, Poland

leon.kukielka@tu.koszalin.pl, radoslaw.patyk@tu.koszalin.pl, lukasz.bohdal@tu.koszalin.pl, wnapadlek@wat.edu.pl, rafal.gryglicki@matsim.pl, piotr.kasprzak@twohorses.pl

received 16 May 2019, revised 18 June 2019, accepted 24 June 2019

Abstract: Lasers are widely used in a variety of manufacturing processes including: depaneling, drilling, cutting, repair, trimming, micromachining. Polypropylene foils are intensively investigated as materials with great number of potential applications. Laser cutting is a major operation used in forming these materials and preparing the final workpieces. At the moment, the main challenge when cutting polypropylene is to obtain high quality products characterized by optimum sheared edge condition, minimum surface damage, freedom from burrs, slivers, edge wave, distortion, residual stresses and to obtain minimum width of HAZ zone. The amount of adjusTab. process parameters and the fact that the influence of these parameters on the process is not fully understood makes it difficult to control the cutting process. In practice, the right setup for the lasers is mostly found by trial and error combined with experience. Therefore, the final product frequently has serious defects. The paper presents the possibility of using fiber and diode lasers for forming of workpieces from polypropylene multilayer foil using cutting technology. The effect of selected process parameters and conditions on quality of sheared edge and material degradation is discussed.

Key words: Laser, Cutting, Polypropylene Foil, HAZ

1. INTRODUCTION

Polypropylene (PP) has been widely used in many industrial branches. This material is characterized by highly adaptable properties, chemical resistance, thermal stability and physiological compatibility. Cutting is a major operation used in forming these materials and preparing final workpieces (Huang et al., 2012; Bohdal, 2016). It has been found that in comparison with mechanical cutting, for example, blanking or guillotining lasers cause less stresses in the material and reduce the cut surface defects, for example, burrs and edge waves. Our preliminary research showed that burr is the main problem in foils' mechanical cutting, which not only affects the geometrical precision of blanked shapes, it also decreases their assembly.

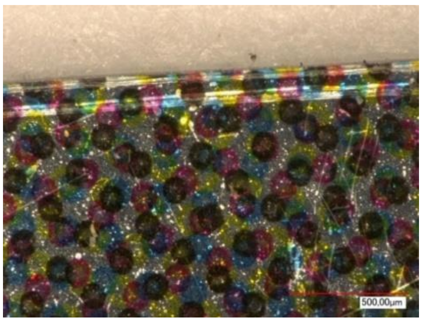

Fig. 1. Rollover formation on cut surface

From technological point of view, it's very problematic to control punch die clearance during blanking or horizontal clearance during shear-slitting operations. The clearance should be minimal and no more than 10% of the thickness of material being cut (Bohdal, 2016). Larger clearance increases the burr height at cut surface. This requires the use of tools with very high dimensional accuracy. Cutting foils increases the possibility of tools' wear (Arroyoa et al., 2010; Langer et al., 2012; Ragusich et al., 2013; Deng et al., 2013). Tool wear causes the rollover formation (Fig. 1) and burr (Fig. 2). While using laser cutting, because of the contact-free material processing, there is no distortion even when thin materials are used. However, laser cutting results in localized melting or chemical degradation, which is a result of hot ablation (Perry et al., 2009; Wan et al., 2009).

Fig. 2. Burr formation on cut surface

Examples of research, experimental results and numerical models of laser cutting processes can be found in the literature. Karnakis et al. (2010) presented the experimental results of micro-

DOI 10.2478/ama-2019-0015

machining of polymers and silicon nitride using reshaped pulsed Gaussian laser beam. Sotnikov et al. (2010) analysed the effect of elliptical beam shapes on cutting performance of silicon using a diode pumped solid state Q-switched UV laser operating at the wavelength of 355 nm. Zhang and Faghri (1999) developed a theoretical model to predict the cavity formation for UV laser micro-machining with nanosecond pulse duration. Wang et al. (2008) used UV laser with 355 nm wave-length to cut the printed circuit boards. Miraouri et al. (2014) analysed high-power CO_2 laser cutting of steel plates. The effect of the input laser cutting parameters on the cut surface quality was analysed. An overall optimization was applied to find out the optimal cutting setting that improve the cut surface quality. It was found that laser beam diameter has a negligible effect on surface roughness, but laser power had a major effect on surface roughness. The cut surface roughness decreases as laser power increases. Caiazzo et al. (2005) examined the application of the CO_2 laser cutting process to three thermoplastic polymers – polyethylene, polypropylene, polycarbonate – in different thickness ranging from t = 2 to 10 mm. The analysis of process parameters such as laser power, cutting speed, type of focusing lens, pressure and flow of the covering gas and material thickness on overall process efficiency and quality of cut surface was investigated. The main aim of work developed by Eltawahni et al. (2010) was to relate the cutting edge quality parameters (responses) namely: upper kerf, lower kerf, ratio of the upper kerf to lower kerf and cut edge roughness to the process parameters considered in this research and to find out the optimal cutting conditions of polyethylene. The process factors implemented in this research were: laser power, cutting speed and focal point position. Mathematical models were developed to establish the relationship between the process parameters and the edge quality parameters. Also, the effects of process parameters on each response were determined. A numerical optimization was performed to find out the optimal process setting at which the quality features are at their desired values. A three dimensional model of laser cutting process of some plastics has been presented by Atanasov and Baeva (1997). With this model, it is possible to determine the maximum cutting speed as a function of substrate thickness or laser power. Work presented by Abrao et al. (2007) evaluated the effect of the processing parameters on the quality of the cut for several engineering plastics. It was evident that the heat-affected zone (HAZ) increases with the increase in laser power, but it decreases with increase in the cutting speed. Uebel and Bliedtner (2014) present different cutting methods and types of laser, which were used in the examinations in order to achieve a distortion-low and high-quality cutting of the materials in the sintered and unsintered state at high process velocities. The test results were analysed using picosecond lasers at different wavelengths (1064 nm, 532 nm and 355 nm). The tests with the sintered materials showed that process quality increases with shorter pulse duration. Additionally, the results can be improved with shorter wavelengths.

There are, however, challenges in laser processing of polypropylene foils, where the goal is to minimise HAZ zone and to use high processing speed. The main problem in practical industry is the amount of adjusTab. laser cutting parameters and the fact that the influence of these parameters on the process is not fully understood. It makes difficult to control the process. In practice, the right setup for the laser parameters is mostly found by trial and error combined with experience. Therefore, the final product frequently has serious defects, for example, sharp edges, rough surfaces along the edges and wide heat affected zone. Among defects, delamination of polypropylene layers appears to be the most critical one (Kurt et al., 2009; Li et al., 2010).

The current work analyses the possibility of using fiber and diode lasers to forming workpieces from multilayer polypropylene foil using cutting technology. The effect of selected process parameters and conditions (for example, shape of cutting line) on quality of sheared edge and material degradation is discussed. The results could be used for proper selection of process conditions.

2. EXPERIMENTAL SETUP

The experimental setup is shown in Figs. 3 and 4. The research is realized using fiber laser Nb:YAG with wave length λ = 1070 nm, frequency f = 25 kHz, constant maximum averaged output power P = 30 W and laser $Nd:YVO_4$ with power P = 5 W, wave length λ = 532 nm and frequency repetition 3 ÷ 50 kHz. A single nanosecond pulse of lasers – carry out about 100 ns. Lasers are integrated with a modern Galvo optical head equipped with a 163 mm lens, head working field min. 100 x 100 mm. The lasers spot size is not more than 60 µm; the base, control automatics, modern software, the column being the 'z' axis is adapted to fix the Galvo head with precise electric control for its movement.

Fig. 3. Experimental setup: fiber Nb:YAG laser

Fig. 4. Experimental setup: diode $Nd:YVO_4$ laser

Polypropylene foils with a thickness of t = 80 µm are used for the tests. Longitudinal and transverse tensile strength tests of the foils are made in accordance with ASTM D882 norm.

According to the standard, five samples with a width of 50 [mm] ± 0.5 [mm] are made for each of the tests. Example of samples for testing tensile strength are shown in Fig. 5.

Fig. 5. Example of samples for determination of tensile strength tests

Fig. 6. Photograph of the test stand for force and displacement measurement: Mecmesin TMS PRO with the FTC force sensor, measuring range 0 ÷ 2500 [N] with an accuracy of 0.1 [N]

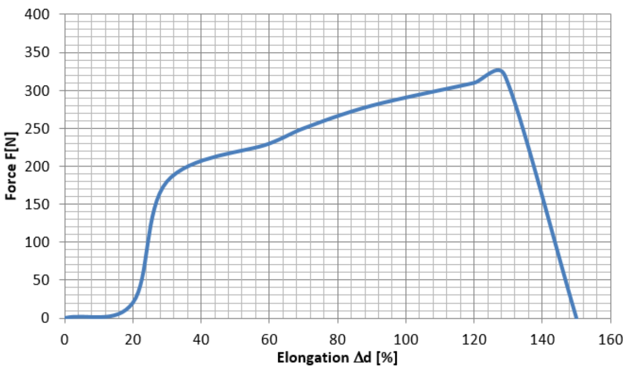

Fig. 7. Graph of changes of tensile force as a function of elongation for the analysed material (t = 80 [μm])

Strength tests are carried out on Mecmesin TMS PRO with a FTC force sensor with a measuring range of 0 ÷ 2500 [N] with an accuracy of 0.1 [N] test stand. The view of the equipment for strength tests is shown in Fig. 6. The stretching process of the samples is carried out with the jaws' moving speed v = 100 [mm/min]. Figs. 7 and 8 show the results of longitudinal elongation of testing material. The tested longitudinal tensile strength carry out σ = 80 (MPa). The tested transverse tensile strength carry out σ = 149 (MPa). The material elongation tested is 129% and the lateral elongation of the material is 44%. These values are important in the production process when the foil tension occurs during its development from the role. The obtained values are sufficient so that production defects resulting from excessive stretching of the film or its tearing during development from the role are not created.

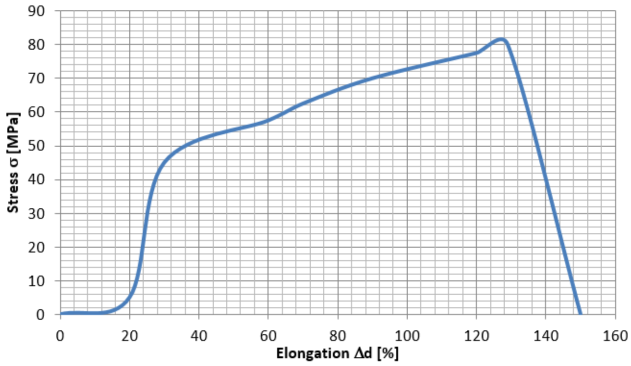

Fig. 8. Graph of changes of tensile stress as a function of elongation for analysed material (t = 80 [μm])

3. EXPERIMENTAL RESULTS

At the first case, the research is realized using the fiber laser Nb:YAG with wave length λ = 1070 nm, frequency f = 25 kHz and constant maximum averaged output power P = 30 W. Foils with a thickness of t = 80 μm are used for the tests. Tests are carried out for five replications for each foil. Example of results are given in Fig. 9. For technological reasons, the tests are carried out for constant parameters of cutting speed v = 3 mm/s and averaged output power P = 30 W. It was not possible to achieve complete separation of the material for multilayer foil. Only the melting and charring of the polypropylene foil in the beam's impact zone is found (Fig. 9a and b). The cutting gap is more regular when cutting along the sheet of film. The change in the direction of the cutting caused the increase of local melts for second foil (Fig. 9b). The gap has narrowed. The depth of gap and width of the HAZ zone increased at this region. The average value of the gap width for foil carry out was S = 120 μm. Developed analysis shows that this type of laser and cutting conditions can be used to cut single-layer foils and realization of other technological processes, for example, drilling contours, incision or micromachining.

At the second case, the research is realized using the diode $Nd:YVO_4$ laser. Foils with a thickness of g = 80 μm are used for the tests. Analysis is carried out for output power P = 5 W different frequency repetition values (f = 3 ÷ 50 kHz) and changed cutting velocities (v = 1 ÷ 3 mm/s). The research is planned using the E-Planner program. Experiment design matrix is given in Tab. 1. From technological point of view it's important to minimalize gap width because it result in material loss (Leone et al., 2013; Kiselev et al., 2011). As a result of hot ablation, HAZ zone is created, which should be minimal at workpiece to reduce chemical degradation of material (Cuong et al., 2010; Zhang et al., 2010). Tests are carried out for five replications for each plan level. The micro-

DOI 10.2478/ama-2019-0015

scope images of samples after cutting are given in Figs. 10 and 11. The influence of analysed parameters on gap width and HAZ zone width along the shearing line is presented in Figs. 12 and 13.

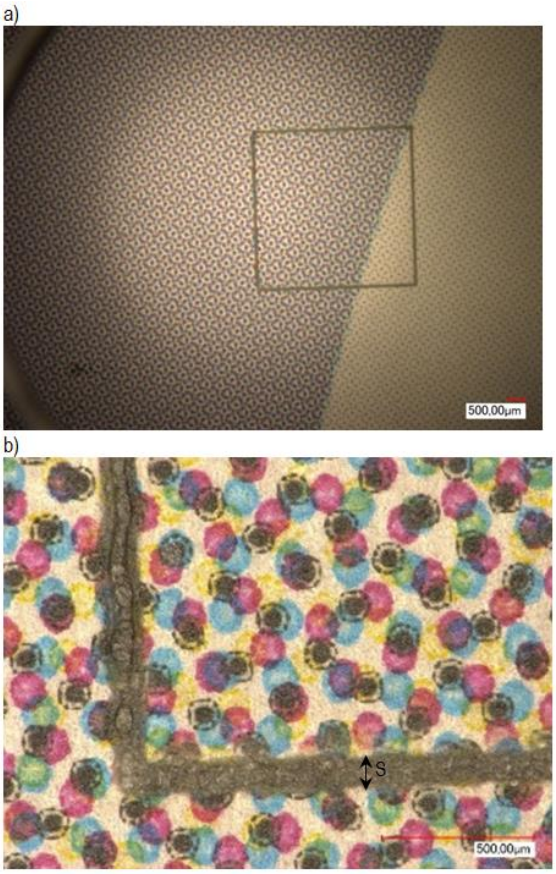

Fig. 9. Example of results obtained using fiber Nb: YAG laser: a) contour of cutting line (Ax100), b) zoom of the cutting line (Ax200)

Tab 1. Five levels compositive rotary plan

Plan level	Coded variables		Real variables	
	$\breve{x}_1$	$\breve{x}_2$	v	f
			(mm/s)	(kHz)
1	-	-	1.29	9.88
2	+	-	2.70	9.88
3	-	+	1.29	43.11
4	+	+	2.70	43.11
5	+α	0	3	26.5
6	-α	0	1	26.5
7	0	+α	2	50
8	0	-α	2	3
9	0	0	2	26.5
10	0	0	2	26.5
11	0	0	2	26.5
12	0	0	2	26.5
13	0	0	2	26.5

Fig. 10. Example of results obtained using diode Nd:YVO₄ laser: v = 1 mm/s, f = 26.5 (kHz)

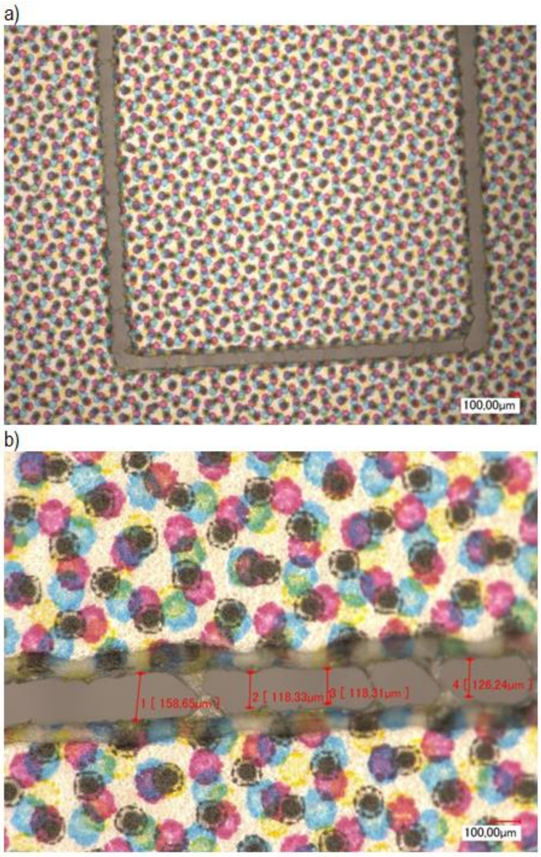

Fig. 11. Example of results obtained using diode Nd:YVO₄ laser: v = 3 mm/s, f = 26,5 (kHz)

DOI 10.2478/ama-2019-0015

A mathematical model in the form of a linear algebraic polynomial with interactions is used to describe the object of the research. For gap width, the regression formula is as follows (R = 0.99):

$$S = 696.605 - 525.407 \cdot \mathrm{v} - 10.796 \cdot \mathrm{f} + 0.021 \cdot \mathrm{v} \cdot \mathrm{f} + 130.250 \cdot \mathrm{v}^2 + 0.209 \cdot \mathrm{f}^2, \quad (1)$$

For HAZ width, the regression formula is as follows (R = 0.87):

$$Hz = 557.128 - 610.332 \cdot \mathrm{v} - 18.754 \cdot \mathrm{f} + 0.106 \cdot \mathrm{v} \cdot \mathrm{f} + 308.952 \cdot \mathrm{v}^2 + 0.711 \cdot \mathrm{f}^2 - 50.291 \cdot \mathrm{v}^3 - 0.008 \cdot \mathrm{f}^3, \quad (2)$$

Fig. 12 shows the effects of the analysed process technological parameters on gap width. The value of gap width depends both on frequency and cutting speed. The minimum gap width was found using parameters from range of: v = 1.6 ÷ 2.4 mm/s and f = 15 ÷ 35 kHz. Selecting values of parameters from outside of this range increases gap width.

It has been observed that the small values of frequency increases the width of HAZ (Fig. 13). The minimum of HAZ can be obtained using middle range of frequencies or high values (f > 40 kHz).

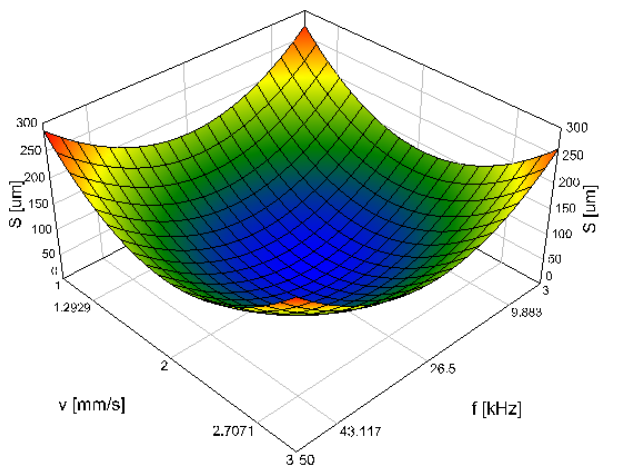

Fig. 12. The influence of frequency f and cutting speed v on gap width S

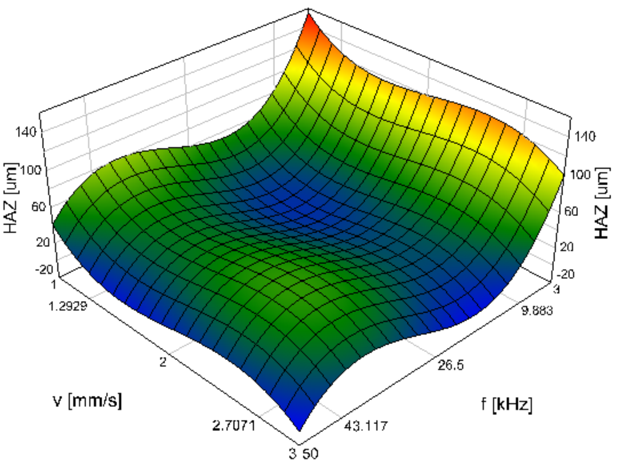

Fig. 13. The influence of frequency f and cutting speed v on HAZ width

Area of acceptable solution is graphically presented in Fig. 14. According to technological criteria S ≤ 50 μm and HAZ H_z ≤ 40 μm. The chart can be used for selection of optimal process parameters in the aspect of maximizing process efficiency and minimizing energy consumption with obtaining high quality of workpieces. It is possible to control the cutting process and minimize the material sheared edge defects.

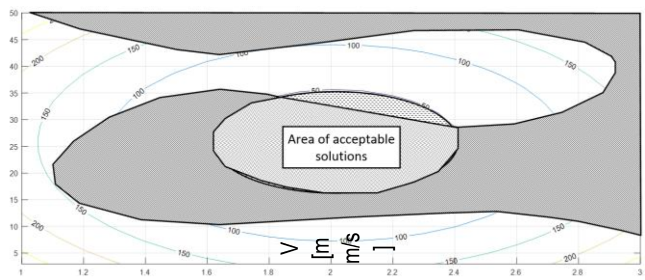

Fig. 14. Chart with area of accepTab. solutions

4. CONCLUSIONS

The paper presents the possibility of using fiber and diode lasers to forming workpieces from polypropylene multilayer foil using cutting technology. The results showed the possibility of using fiber laser in the analysed configuration to cut a single layer foil. It can also be used for other technological processes, for example, incision, drilling or micromachining. Using diode laser, it is possible to obtain high quality of workpieces. Analysed two main process parameters' frequency and cutting speed has significant influence on the final workpiece quality. Proper selection of these parameters is a key factor, which determines the HAZ zone and gap width. Obtained results of cutting multilayer polypropylene foil using diode Nd:YVO4 laser can be used for the selection of optimal process parameters in the aspect of maximizing process efficiency and minimizing energy consumption.

REFERENCES

1. **Abrao AM., Faria PE., Campos Rubio JC., Reis P., Paulo Davim J.,** (2007), Drilling of fiber reinforced plastics: a review. *International Journal of Manufacturing Technology*, 186: 1–7.
2. **Arroyoa J.M, Diniz A.E., Fernandes de Lima M.S.,** (2010), Wear performance of laser precoating treated cemented carbide milling tools, *Wear* 268, 1329–1336.
3. **Atanasov P. A., Baeva M. G.,** (1997), CW CO_2 laser cutting of plastics, *Proceedings SPIE* 3092, 772–775.
4. **Bohdal L.,** (2016), The application of the smoothed particle hydrodynamics (SPH) method to the simulation and analysis of blanking process, *Mechanika*, 22 (5), 380–387.
5. **Caiazzo F., Ciurcio F., Daurelio G., Memola Capece Minutolo F.,** (2005), Laser cutting of different polymeric plastics (PE, PP and PC) by CO_2 laser beam, *Journal of Materials Processing Technology,* 159, 279–285.
6. **Cuong T.V., Pham V.H., Tran Q.T., Hahn S.H., Chung J.S., Shin E.W., Kim E.J.,** (2010), Photoluminescence and Raman studies of graphene thin films prepared by reduction of graphene oxide, *Materials Letters* 64, 399–40.
7. **Deng J., Li S., Xing Y., Li Y.,** (2014), Studies on thermal shock resistance of TiN and TiAlN coatings under pulsed laser irradiation, *Surface Engineering* 30 (3), 195–203.
8. **Eltawahni H. A., Olabi A. G., Benyounis K. Y.,** (2010), Effect of process parameters and optimization of CO_2 laser cutting of ultra high performance polyethylene, *Materials and Design* 31 (8), 4029-4038.

DOI 10.2478/ama-2019-0015

9. **Huang Y.J., Huang Y.P., Chiang P.Y., Liang H.C., Su K.W., Chen Y.-F.** (2012), High-power passively Q-switched Nd:YVO4 UV laser at 355 nm, *Applied Physics B.*, 106, 893–898.
10. **Karnakis D., Fieret J., Rumsby P., Gower M.** (2010), Microhole drilling using reshaped pulsed Gaussian beams *(private correspondence).*
11. **Kiselev A. M., Ponomarev Yu. N., Stepanov A. N., Tikhomirov A. B., Tikhomirov B. A.,** (2011), Nonlinear absorption of femtosecond laser pulses (800 nm) by atmospheric air and water vapour, *Quantum Electronics* 41 (11), 976–980.
12. **Kurt M., Kaynak Y., Bagei E., Demirer H., Kurt M.,** (2009), Dimensional analyses and surface quality of laser cutting process for engineering plastics, *International Journal of Manufacturing Technology*, 41, 259–267.
13. **Langer M., Rechner R., Thieme M., Jansen I., Beyer E.,** (2012), Surface analytical characterisation of Nd:YAG-laser pre-treated Al Mg3 as a preparation for bonding, *Solid State Sciences* 14(7):926–35.
14. **Leone C., Papa I., Tagliaferri F., Lopresto V.,** (2013), Investigation of CFRP laser milling using a 30W Q-switched Yb:YAG fiber laser: Effect of process parameters on removal mechanisms and HAZ formation. *Composites Part A: Applied Science and Manufacturing* 55, 129–42.
15. **Li Z.L., Zheng H.Y., Lim G.C., Chu P.L., Li L.,** (2010), Study on UV laser machining quality of carbon fiber reinforced composites. *Composites: Part A* 41, 1403–1408.
16. **Miraouri I., Boujelbene M., Bayraktar E.** (2014), Analysis of roughness and heat affected zone of steel plates obtained by laser cutting, *Advanced Materials Research*, 974,169–173.
17. **Perry T.L., Werschmoeller D., Li X.C., Pfefferkorn F.E., Duffie N.A.,** (2009), Pulsed laser polishing of micro-milled Ti6Al4V samples. *Journal of Manufacturing Processes* 11(2):74–81.
18. **Ragusich A., Taillon G., Meunier M., Martinu L., Klemberg-Sapieha J.E.,** (2013), Selective pulsed laser stripping of TiAlN erosion-resistant coatings: effect of wavelength and pulse duration, *Surface Coating Technology* 232, 758–766.
19. **Sotnikov A., Laux H., Stritzker B.,** (2010), Experimental and Numerical Optimization of Beam Shapes for Short-Pulse Ultraviolet Laser Cutting Processing, *Physics Procedia* 5, 137–146.
20. **Uebel M., Bliedtner J.,** (2014), Laser precision cutting of high-melting metal foils, *Procedia Engineering* 69, 99–103.
21. **Wan D.P., Liang X.C., Meng F.M., Hu D.J., Wang Y.M., Chen N.K, Shao T.M.,** (2009), Automatic compensation of laser beam focusing parameters for flying optics. *Optics and Laser Technology* 41(4):499–503.
22. **Wang X.C., Li Z.L., Chen T., Lok B.K., Low D.K.Y.** (2008), 355nm DPSS UV laser cutting of FR4 and BT/epoxy-based PCB substrates, *Opt. Lasers Eng.* 46, 404-409.
23. **Zhang Y., Faghri A.,** (1999) Int. J. Heat Mass Transfer 42, 1775.
24. **Zhang Y.-L., Guo L., Wei S., He Y., Xia H., Chen Q., Sun H.-B., Xiao F.-S.,** (2010), Direct imprinting of microcircuits on graphene oxides film by femtosecond laser reduction, *Nano Today* 5, 15–20.

Acknowledgements: This work was financially supported by the National Centre for Research and Development Operational Programme Intelligent Development no. agreement POIR.01.01.01-00-0933/17-00.

European Funds Smart Growth · Republic of Poland · The National Centre for Research and Development · European Union European Regional Development Fund

INVESTIGATION OF MECHANOCHEMICAL LEACHING OF NON-FERROUS METALS

Vladimir GOLIK,[*] Vladimir MORKUN,[**] Natalia MORKUN,[**] Vitaliy TRON[**]

[*]Mining Department, North-Caucasian State Technological University, Cosmonaut Nikolayev St. 44, Vladikavkaz, Russia
[**]Automation, Computer Science and Technologies Department, Kryvyi Rih National University,
Vitalii Matusevich St., 11, Kryvyi Rih, Ukraine

v.i.golik@mail.ru, morkunv@gmail.com, nmorkun@gmail.com, vtron@ukr.net

received 17 December 2018, revised 21 June 2019, accepted 25 June 2019

Abstract: The research deals with metal extraction from off-grade ores and concentration tailings. There are provided results of simulating parameters of reagent leaching of metals in the disintegrator according to the metal recovery ratio. The research substantiates the method of waste-free processing of chemically recovered ores. Recovery of metals into solution is the same both under multiple leaching of tailings or ore in the disintegrator and agitation leaching of tailings or ore previously activated in the disintegrator with leaching solutions. The time of agitation leaching is more by two orders of magnitude than that of the disintegrator processing. Recovery of metals into solution is most affected by the content of sodium chloride in the solution. Then, in decreasing order, go the content of sulfuric acid in the solution, the disintegrator rotor rpm and L:S ratio.

Key words: Experiment, simulation, activation, concentration tailings, disintegrator, leaching

1. INTRODUCTION

Mineral mining for industrial branches is characterized by large-scale operations, application of powerful equipment, the extent of impacts on the environment and involvement of off-grade materials into production accompanied by increased wastes after processing (Liu et al., 2012; Sinclair and Thompson, 2015; Dmitrak and Kamnev, 2016). The threat of environment pollution can be decreased by non-waste utilization of processing tailings. Known concentration processes do not meet this requirement. They can be updated due to introduction of chemical and hydrometallurgical concentration processes (De Oliveira et al., 2014; Lyashenko et al., 2015; Golik et al., 2015c). In 1950s, a new technology called substance activation by high energy won the recognition. The energy acting with the velocity of 250 m/sec, the substance properties change and it is able to react with other substances (Khint, 1981).

Scientific papers dealing with geotechnological processes in concentration are topical. Yet, leaching by itself does not make extraction non-waste. Therefore, development of technologies combining chemical and mechanical processes is particularly promising (Golik et al., 2015b; Jordens et al., 2013; Gazaleyeva et al., 2017). The process of metal extraction from off-grade mineral materials can be facilitated by changing properties of substances in the disintegrator when metals are extracted, while crystals are destroyed under the action of reagents. The research aims to experimentally substantiate this concept (Morkun and Tron, 2014; Golik et al., 2015a; Golik et al., 2015e; Golik, 2013).

2. LITERATURE ANALYSIS AND PROBLEM STATEMENT

Methods of ore mineral concentration differ in the kinetics of recovery in apparatuses that realize physical principles of disintegration. The ore recovery degree during concentration in different apparatuses changes from 54% to 80%.

The study (Zhang et al., 2019) provides an approach to improve the recycling of zinc and iron and effectively reduce environmental risks from electric arc furnace dust. In this article, a hydrothermal reduction method was proposed to recover Zn selectively from electric arc furnace dust. The total Zn leaching efficiency was calculated to be 89.7%, producing Zn-impregnated leach solution and a leach residue rich in Fe. However, this process also has its shortcomings owning to larger liquid-solid ratio in the leaching process.

In the work by Xie et al. (2019), the feasible method for the extraction of lead from lead-containing zinc leaching residues was proposed. The effects of reaction time, reaction temperature, calcium chloride concentration, liquid-solid ratio, and pH were studied. It was shown that the calcium chloride concentration and the liquid-solid ratio have a significant influence on lead leaching rate and the optimized technological conditions were obtained.

The research by Wang et al. (2018) presented the impacts of mechanochemical activation on the physiochemical properties of lithium cobalt oxide powders of cathode materials from spent lithium-ion batteries, and analysed the relevant effects of these changes on the leaching efficiency of lithium and cobalt and the leaching kinetics of powders. The results revealed the superiority of mechanochemical activation in the following levels of changes in the powders. The physical properties included a decrease in the average particle size, an increase in the specific surface area, and the appearance of a mesoporous structure change.

In the research by Cetintas et al. (2018), the method for nickel recovery from lateritic ore was proposed. The method consisted of mechanochemical conversion in the presence of a reagent, ammonium carbonate or sodium hydroxide, then followed by an acid leaching. The study presents the recovery of nickel from lateritic ore at low temperature and lower acid consumption to overcome the disadvantages of traditional metallurgical processes such as

DOI 10.2478/ama-2019-0016

high temperature, high acid concentration, high cost and material requirements. The optimization conditions for both mechanochemical conversion and atmospheric leaching processes were evaluated by response surface methodology to clearly demonstrate the advantages of the proposed method over conventional methods.

The research by Fan et al. (2018) gave the results of the selective extraction of Fe and Li from spent batteries via an environmentally friendly mechanochemical process with oxalic acid. With the use of a mechanochemical treatment and water leaching, the Li extraction efficiency can be improved to 99%. To investigate the reaction mechanism and determine the optimum reaction conditions, various parameters, including rotation speed, milling time, and ball-to-powder mass ratio were investigated.

In the work of Minagawa et al. (2018), the influence of planetary ball milling and vertical stirred ball milling on the leaching of a copper ore containing copper sulphate and covellite was investigated. A mixed experimental-simulation approach to correlate the kinetic parameters of leaching to the collision energy during grinding was used. The leaching of the ore occurred through three subsequent steps. It was confirmed that the rate constants for the leaching of covellite increased due to an occurred mechanochemical reaction.

In the research by Yang et al., 2017, mechanochemical activation was developed to selectively recycling Fe and Li from cathode scrap of spent batteries. By mechanochemical activation pre-treatment and the diluted leaching solution, the leaching efficiency of Fe and Li can be significantly improved, respectively. Through process and the mechanochemical activation mechanisms, the effects of various parameters during Fe and Li recovery were comprehensively investigated, including activation time, cathode powder to additive mass ratio, acid concentration, the liquid-to-solid ratio, and leaching time.

The work by Granata et al. (2018) addressed the mechanochemical activation of chalcopyrite by vertically stirred ball milling to enhance copper dissolution in leaching. The contribution of each activation mechanism to leaching enhancement was assessed by two-stage leaching. The increase of copper extraction in the first stage leaching confirmed the increase of soluble copper due to mechanochemical oxidation. Second stage leaching highlighted a larger dissolution of copper from chalcopyrite and enhanced kinetics upon activation.

The general drawback of the known technologies of processing tailings utilization is incomplete metal extraction resulting in accumulated secondary tailings in the vicinity of mining enterprises (Golik et al., 2015d; Ghorbani et al., 2016; Wang et al., 2015).

3. RESEARCH AIM AND TASKS

This research is aimed at investigating a mechanism and parameters of leaching off-grade metallic ores by experimental substantiation of metal recovery by leaching in the disintegrator and simulation of the process parameters providing the evidence of non-waste processing of chemically recovered ores.

To achieve this aim, indices of ore concentration technologies should be systematized, the theory and practice of recovery activation should be analysed and experimental leaching should be performed.

4. MATERIALS AND RESEARCH METHODS

To balance metal losses in ore concentration, magnetic, gravity and electrochemical separation methods are used, making it possible to obtain marketable products from concentration tailings.

The technology developed by the Institute of Ore Deposit Geology, Petrography, Mineralogy and Geochemistry of the Russian Academy of Sciences is intermediate between pyro- and hydrometallurgy as ore is broken down at 550°C at the normal air pressure with subsequent leaching. Specific low-temperature (100–550°C) interaction of processed ores and water chlorides is used. In this thermal interval under the normal air pressure, some minerals are destroyed and oxidized. The process is accompanied by transformation of metals into the forms dissolved in subsequent acid leaching.

The disintegrator consists of rotors and a basket (Fig. 1, 2).

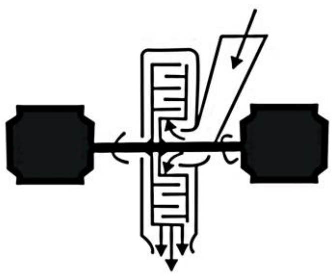

Fig. 1. The fundamental scheme of the disintegrator

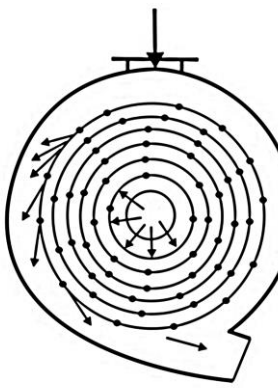

Fig. 2. Direction of forces in the working body of the disintegrator

The dashers are located between rotor disks so that each row of dashers of one rotor is located between two rows of dashers of the other. Materials are fed to the central part of the rotor and on the way to the periphery, they are beaten with the rotation velocity of over 500 rpm.

In mechanical ore processing, energy is accumulated and part of this energy is accumulated on the newly created surfaces and spent on chemical processes. In processing polycrystalline raw materials, they are destroyed on the boundary of phase separation as well. Processes of phase separation from ores in the disintegrator are significantly simplified and the end product yield increases. For the first time, the industrial disintegrator was used for 5 years at Shokpak deposit (Kazakhstan).

The industrial plant ДУ-65 was equipped with 200 and 250 kW engines, self-bushing rotors with a protective layer in the stowing complex net (Fig. 3).

The disintegrator produced up to 55% of the active class and combined with the vibration mill its yield increased up to 70%. The disintegrator was located in a three-level building with the foundation of 5×7 m. The disintegrator technology provided activity increase up to 40%. In disintegration products, the fraction of particles larger than 125–400 mkm is comparatively small and the fraction is less than 5 mkm. The values of specific slag surfaces of single and secondary grinding in the disintegrator differ by a factor of 1.4, while the content of fractions of less than 63 mm is much higher in case of secondary grinding.

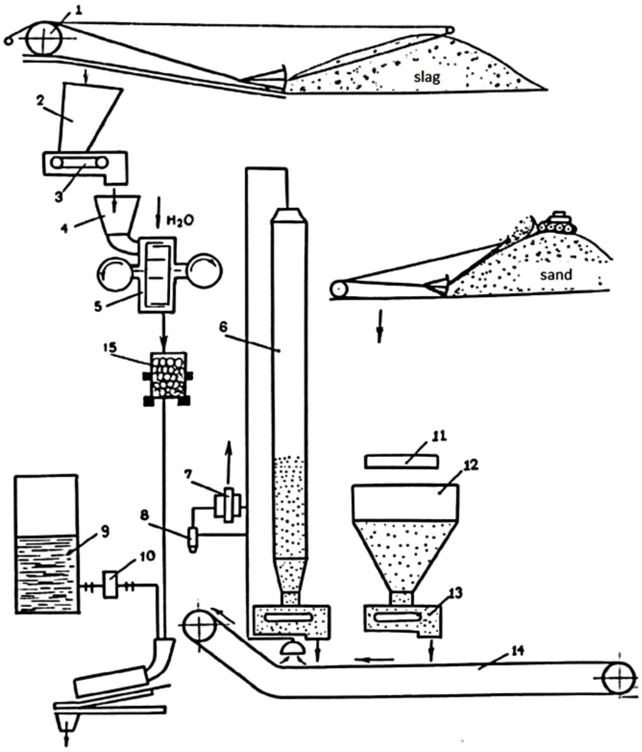

Fig. 3. The disintegrator in the net of the stowing complex: 1 – a scraper hoist; 2 – a storage bin; 3 – a metering unit; 4 – a feeder; 5 – a disintegrator; 6 – a silo tower; 7 – a fan; 8 – a water block; 10 – a pump; 11 – a screen; 12 – a sand bin; 13 – a metering unit; 14 – a conveyor; 15 – a vibration mill

Fig. 4. The assembled view of the disintegrator DES-11

It is explained by the fact that on the way from the basket centre to their periphery, ore particles are repeatedly accelerated and decelerated for milliseconds.

Metals were recovered experimentally in the disintegrator DES-11 (Fig. 4). The maximum capacity of the disintegrator in grinding materials of 2...3 g/sm^3, with the rotor rotation of 12,000 rpm is 1–10 kg/h, the maximum initial size of particles of the processes material is 2.5 mm, the maximum humidity of the ground material is 2%.

The research stages included: investigating concentration tailings; leaching tailings in percolators; leaching tailings in the disintegrator. 0.05 t of floatation tailings of Misur plant was processed. Tailings were screened (the cell size of 2.0 mm) and fed to the basket with the reagent solution. The efficiency of metal recovery was investigated through comparing leaching variants (***Błąd! Nie można odnaleźć źródła odwołania.***).

Tab. 1. Results of the disintegrator testing

Indices	Testing stage			
	0	1	2	3
1. Tailings processed, t	0.04	0.09	0.03	0.04
2. Reduced mass of rotors due to wear, kg	7	0	0.1	0.5
3. Net metal consumption for wear, kg/t	0.01	0.01	0.01	0.01
4. Time for tailings processing, min	25	5	05	45
5. Plant capacity, t/h	0.01	0.04	0.03	0
6. No-load capacity of the external rotor, kW	0.4	0.4	0.4	0.4
7. No-load capacity of the internal rotor, kW	0.2	0.2	0.2	0.2
8. Processing capacity of the external rotor, kW	0.05	0.05	0.50	0.50
9. Processing capacity of the internal rotor, kW	0.7	0.7	0.9	0.8
10. Gross energy consumption of the external rotor, kW h/t	0.07	0.1	0.1	0.1
11. Gross energy consumption of the internal rotor, kW h/t	0.03	0.02	0.02	0.02
12. Gross energy consumption, kW h/t	0.5	0.3	0.2	0.3
13. Net energy consumption of the external rotor, kW h/t	0.20	0.16	0.16	0.20
14. Net energy consumption of the internal rotor, kW h/t	0.05	0.03	0.03	0.04
15.Net energy consumption, kW h/t	0.75	0.69	0.69	0.74

Ores of Sadon deposits were concentrated in heavy slurries. Tailings make 25–50% of the initial feed rate.

The ratio of components is following: coarse grained granites make 40%; porfirites make 30%, sandstones make 20%; vein materials make 8%; ore minerals make 2%. The content of base metals in tailings is following: pyrite – 1.4%; sphalerite – 0.6%; galena – 0.06%; chalcopyrite – 0.05%.

5. INVESTIGATION RESULTS

There were five stages of experiments: agitation leaching of tailings or ore in the percolator; agitation percolator leaching of tailings or ore previously activated in the disintegrator in the dry condition; leaching of tailings or ore by reagents in the disintegrator chamber; agitation leaching of tailings or ore previously activated in the disintegrator chamber with reagents during a single

DOI 10.2478/ama-2019-0016

stage; leaching of tailings or ore previously activated in the disintegrator chamber with reagents during several stages.

The applied factors regulated during experiments include:

- the content of sulfuric acid and sodium chloride (changes depending on the level: X_1-1 - 2, 0 - 6 and 1–10 g/l, X_2 -1 - 20, 0–90 and 1–160 g/l);
- the ratio of L:S (liquid and solid phases) (changes according to the level: X_3 - 1- 4, 0 – 7 and 1–10),
- the time period of agitation leaching, X_4, (changes according to the level: X_4 -1 -0.25, 0–0.5, 1–1 hour, except for the experiments of the 3rd and 5th stages);
- the disintegrator rotors rpm, X_5, (changes according to the level: X_5 -1 -50, 0–125, 1–200 Hz, except for the experiments of the 1st stage),
- the number of leaching cycles, X_6, (changes according to the level: X_6 -1 -3, 0–5, 1–7) of tailings or ores in the disintegrator (only for the experiments of the 5th stage).

Leaching parameters include: the 0.08 active class yield, the chemical composition of the ores under study, the metal content in the solution, mg/l, metal extraction into the solution, %. The value of the indices in Sadon ores leaching made: the active class yield of 44.4%, the chemical composition, %: Al_2O_3 – 20.8; Si – 50. 29; S – 4.9; Cl – 0.06; Ag – 0.1; K_2O – 5,4; CaO – 2.5; TiO_2 – 0.79; Mn – 0.26; Fe – 7.5; Cu – 0.2; Zn – 3.9; Pb – 1.6.

To estimate the metal leaching technologies, the parameters of conventional (Table 2–4) and innovative leaching (Table 5–11), experimental data are determined and depicted graphically (Fig. 5–10).

Tab. 2. Results of agitation leaching of ore

#	Reagent content, g/l		L:S ratio	Time of leaching, h	Recovery into solution, ε, %	
	H_2SO_4	NaCl			Zn	Pb
1	2	20	4	0.25	26.63	0.25
2	10	20	4	0.25	38.25	0.50
3	2	160	4	0.25	12.50	8.50
4	10	160	4	0.25	18.25	11.75
5	2	20	10	0.25	28.75	2.50
6	10	20	10	0.25	57.81	0.50
7	2	160	10	0.25	22.19	13.13
8	10	160	10	0.25	25.63	15.00
9	2	20	4	1	23.75	0.25
10	10	20	4	1	38.00	0.50
11	2	160	4	1	13.38	7.50
12	10	160	4	1	21.75	14.75
13	2	20	10	1	56.56	1.88
14	10	20	10	1	57.50	1.25
15	2	160	10	1	23.75	14.38
16	10	160	10	1	20.31	11.88
17	2	90	7	0.625	28.00	12.25
18	10	90	7	0.625	57.19	14.88
19	6	20	7	0.625	60.59	0.88
20	6	160	7	0.625	30.41	25.00
21	6	90	4	0.625	29.25	8.50
22	6	90	10	0.625	30.00	17.50
23	6	90	7	0.25	29.31	13.56
24	6	90	7	1	29.97	14. 88

Tab. 3. Regression analysis of experimental data

Regression equation	Significance indices
ε_{Zn}=39.02 +5.51X_1-11.09X_2 +5.6X_3+1.43X_4 +3.58X_1^2+6.48X_2^2-9.39X_3^2 -9.38X_4^2- 2.61X_1X_2 - 0.62X_1X_3 -1.86X_1X_4 -3.0X_2X_3-1.48X_2X_4 +1.41X_3X_4	R^2 = 0.8873; S_{ad} = 62.01; F = 31.96
ε_{Pb}=15.73 +0.58X_1+6.3X_2+1.42X_3 – 2.17X_1^2 - 2.79X_2^2-2.73X_3^2-1.51X_4^2 ++0.75X_1X_2 -0.89X_1X_3 +0.45X_2X_3-0.23X_3X_4	R^2 = 0.9023; S_{ad} = 9.37; F = 25.89

Note: dimensionless variables are determined from the expressions:

$$X_1 = \frac{C_{H_2SO_4}-6}{4};\ X_2 = \frac{C_{NaCl}-90}{70};\quad X_3 = \frac{(L:S)-7}{3};\ X_4 = \frac{t-0,625}{0,375}; \tag{1}$$

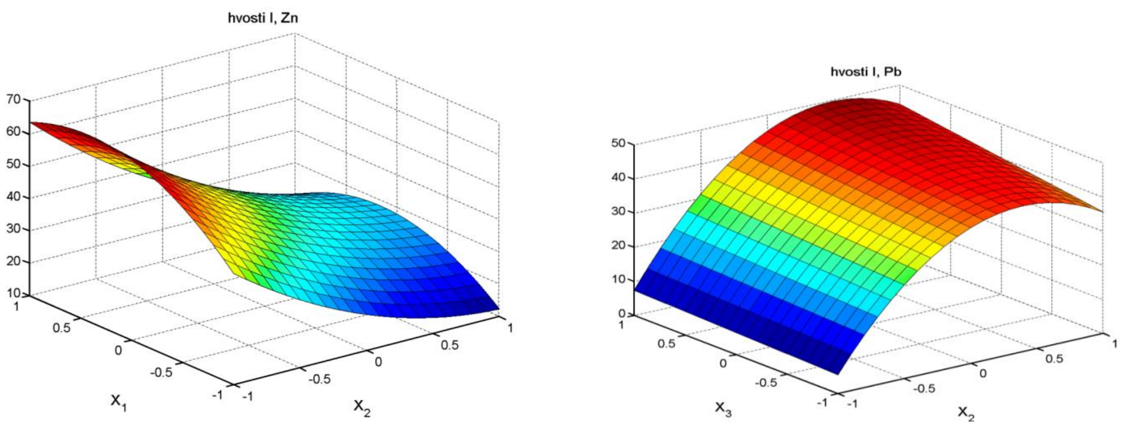

Fig. 5. Results of agitation leaching of ore: a) zinc; b) lead

sciendo
DOI 10.2478/ama-2019-0016 acta mechanica et automatica, vol.13 no.2 (2019)

Tab. 4. Results of agitation leaching of tailings

#	Reagent content, g/l		L:S ratio	Time of leach-ing, h	Recovery into solution, ε, %	
	H_2SO_4	NaCl			Zn	Pb
1	2	20	4	0.25	41.26	1.43
2	10	20	4	0.25	57.76	0.48
3	2	160	4	0.25	18.11	36.19
4	10	160	4	0.25	24.00	38.10
5	2	20	10	0.25	48.42	3.57
6	10	20	10	0.25	82.11	4.76
7	2	160	10	0.25	12.63	30.95
8	10	160	10	0.25	17.89	35.71
9	2	20	4	1	44.58	17.14
10	10	20	4	1	70.26	1.43
11	2	160	4	1	10.95	24.76
12	10	160	4	1	28.21	37.14
13	2	20	10	1	49.47	3.57
14	10	20	10	1	50.53	1.79
15	2	160	10	1	15.79	46.43
16	10	160	10	1	18.95	44.05
17	2	90	7	0.625	21.37	35.83
18	10	90	7	0.625	34.63	41.67
19	6	20	7	0.625	67.79	1.67
20	6	160	7	0.625	25.79	45.00
21	6	90	4	0.625	40.84	21.29
22	6	90	10	0.625	36.84	58.33
23	6	90	7	0.25	40.53	49.17
24	6	90	7	1	42.74	40.83

Tab. 5. Regression analysis of experimental data

Regression equation	Significance indices
$\varepsilon_{Zn}=39.35 +6.76X_1-18.88X_2 -0.62X_4 - 11.6X_1^2+7.19X_2^2+2.03X_4^2 -$ $-2.84X_1X_2 -1.39X_1X_3 -0.89X_1X_4 -2.04X_2X_3+1.00X_2X_4 -2.45X_3X_4$	R^2 = 0.9393; S_{ad} = 46.93; F = 68.59
$\varepsilon_{Pb}=42.43 +16.8X_2+2.68X_3 +0.93X_4 - 3.89X_1^2 - 19.31X_2^2+2.36X_4^2 +$ $+2.12X_1X_2 -0.9X_1X_4 +1.73X_2X_3+1.04X_3X_4$	R^2 = 0.8888; S_{ad} = 71.17; F = 30.19

Note: dimensionless variables are determined from the expressions:

$$X_1 = \frac{C_{H_2SO_4}-6}{4};\ X_2 = \frac{C_{NaCl}-90}{70};\ X_3 = \frac{(L:S)-7}{3};\ X_4 = \frac{t-0,625}{0,375}; \qquad (2)$$

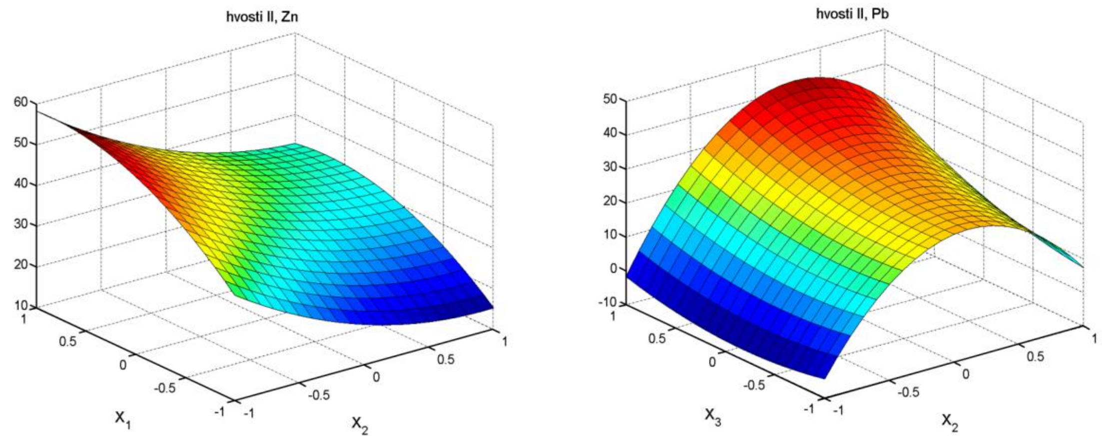

Fig. 6. Results of agitation leaching of ore: a) zinc; b) lead

Tab. 7. Results of agitation leaching of activated ore

#	Reagent content, g/l		Time of leach-ing, h	Rotor rpm, Hz	Recovery into solution, ε, %	
	H_2SO_4	NaCl			Zn	Pb
1	2	20	0.25	50	14.63	0.25
2	10	20	0.25	50	11.63	7.75
3	2	160	0.25	50	16.50	11.25
4	10	160	0.25	50	12.13	11.13
5	2	20	0.25	50	35.00	1.19
6	10	20	0.25	50	35.31	1.44
7	2	160	0.25	50	12.19	11.25
8	10	160	0.25	50	13.44	11.88
9	2	20	1	200	21.50	0.35
10	10	20	1	200	36.63	0.50
11	2	160	1	200	7.38	5.00
12	10	160	1	200	18.63	13.50
13	2	20	1	200	30.63	1.88
14	10	20	1	200	39.38	1.44
15	2	160	1	200	15.63	11.88
16	10	160	1	200	21.56	12.5
17	2	90	0.625	125	12.25	6.56
18	10	90	0.625	125	27.34	16.63
19	6	20	0.625	125	41.34	1.31
20	6	160	0.625	125	18.81	11.88
21	6	90	0.25	125	15.63	7.5

DOI 10.2478/ama-2019-0016

#	Reagent content, g/l		Time of leaching, h	Rotor rpm, Hz	Recovery into solution, ε, %	
	H_2SO_4	NaCl			Zn	Pb
22	6	90	1	125	38.13	26.25
23	6	90	0.625	50	24.28	14.00
24	6	90	0.625	200	25.81	20.56

Tab. 6. Regression analysis of experimental data

Regression equation	Significance indices
ε_{Zn}=26.82+2.8X_1-7.21X_2+4.81X_3+2.34X_4–6.99X_1^2+3.29X_2^2- 1.74X_4^2- –0.45X_1X_2 +2.93X_1X_4 -2.98X_2X_3 -1.41X_2X_4 - 1.12X_3X_4	R^2 = 0.8582; S_{ad} = 31.92; F = 35.03
ε_{Pb}=11.16 +1.51X_1+4.68X_2+ 0.53X_3 - 0.81X_4+0.50X_1^2-4.50X_2^2- -0.72X_3^2 -0.94X_1X_3+0.60X_2X_3+0.24X_2X_4 +0.81X_3X_4	R^2 = 0.8754; S_{ad} = 6.87; F = 23.92

Note: dimensionless variables are determined from the expressions:

$$X_1 = \frac{C_{H_2SO_4}-6}{4};\ X_2 = \frac{C_{NaCl}-90}{70};\quad X_3 = \frac{t-0{,}625}{0{,}375};\ X_4 = \frac{f-125}{75}; \tag{3}$$

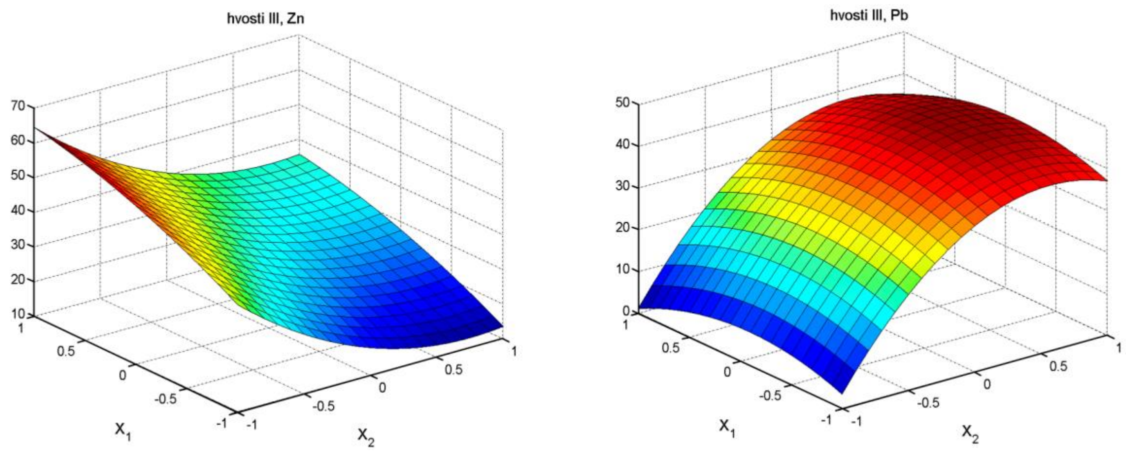

Fig. 7. Results of agitation leaching of ore: a) zinc; b) lead

Tab. 8. Results of agitation leaching of activated tailings

#	Reagent content, g/l		Time of leaching, h	Rotor rpm, Hz	Recovery into solution, ε, %	
	H_2SO_4	NaCl			Zn	Pb
1	2	20	0.25	50	19.37	0.81
2	10	20	0.25	50	56.00	0.95
3	2	160	0.25	50	6.74	17.62
4	10	160	0.25	50	28.21	2.38
5	2	20	0.25	50	50.53	3.21
6	10	20	0.25	50	61.05	2.62
7	2	160	0.25	50	4.63	35.71
8	10	160	0.25	50	13.68	38.10
9	2	20	1	200	28.63	1.43
10	10	20	1	200	66.11	0.86
11	2	160	1	200	1.01	3.33
12	10	160	1	200	27.79	37.14
13	2	20	1	200	50.53	2.98
14	10	20	1	200	51.58	6.67
15	2	160	1	200	6.74	36.90
16	10	160	1	200	15.79	38.10
17	2	90	0.625	125	16.21	30.00
18	10	90	0.625	125	43.47	25.00
19	6	20	0.625	125	60.42	2.83
20	6	160	0.625	125	23.58	4.42
21	6	90	0.25	125	36.11	28.33
22	6	90	1	125	34.63	39.17
23	6	90	0.625	50	36.84	33.33
24	6	90	0.625	200	28.00	45.00

Tab. 9. Results of agitation leaching of activated tailings

Regression equation	Significance indices
ε_{Zn}=36.37+9.96X_1-11.56X_2+1.07X_3–6.53X_1^2+5.63X_2^2-1.00X_3^2- 3.95X_4^2- –1.21X_1X_2 -5.79X_1X_3 -4.16X_2X_3 - 0.74X_2X_4 -1.15X_3X_4	R^2 = 0.9688; S_{ad} = 24.88; F = 102.17
ε_{Pb}=29.91 +1.1X_1+10.63X_2+ 6.15X_3 +2.09X_4–2.41X_1^2-26.29X_2^2+3.84X_3^2+ +9.25X_4^2 +1.21X_1X_2 - 0.72X_1X_3+3.21X_1X_4+4.81X_2X_3+ +1.08X_2X_4 -1.00X_3X_4	R^2 = 0.8789; S_{ad} = 86.00; F = 10.52

Note: dimensionless variables are determined from the expressions:

$$X_1 = \frac{C_{H_2SO_4}-6}{4};\ X_2 = \frac{C_{NaCl}-90}{70};\quad X_3 = \frac{t-0{,}625}{0{,}375};\ X_4 = \frac{f-125}{75}; \tag{4}$$

DOI 10.2478/ama-2019-0016 acta mechanica et automatica, vol.13 no.2 (2019)

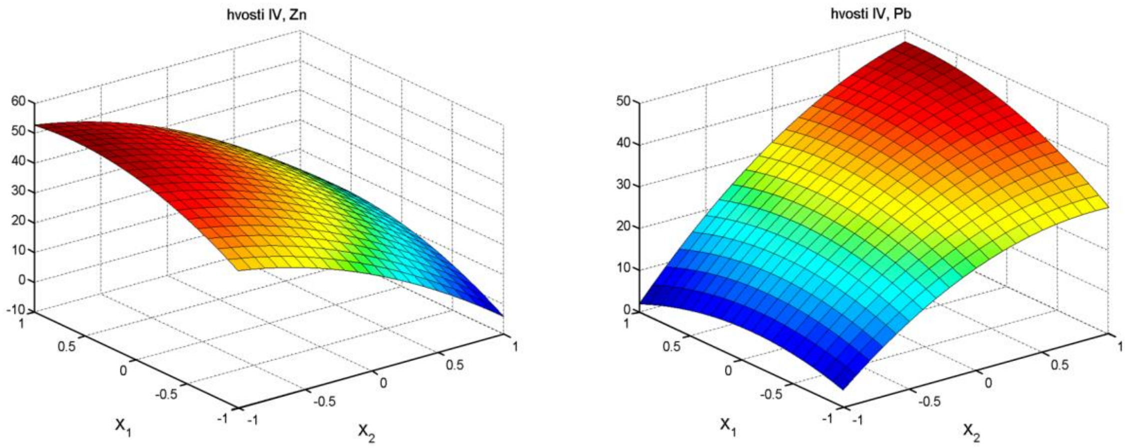

Fig. 8. Results of agitation leaching of activated tailings: a) zinc; b) lead

Tab. 10. Results of leaching ore in the disintegrator

#	Reagent content, g/l		L:S ratio	Rotor rpm, Hz	Recovery into solution, ε, %	
	H_2SO_4	NaCl			Zn	Pb
1	2	20	4	50	10.88	0.63
2	10	20	4	50	41.63	0.50
3	2	160	4	50	13.75	7.25
4	10	160	4	50	20.25	10.00
5	2	20	10	50	36.87	2.50
6	10	20	10	50	38.75	1.06
7	2	160	10	50	15.31	1.00
8	10	160	10	50	17.50	1.00
9	2	20	4	200	24.88	0.33
10	10	20	4	200	43.50	0.35
11	2	160	4	200	14.75	7.50
12	10	160	4	200	22.88	11.75
13	2	20	10	200	37.19	2.50
14	10	20	10	200	45.31	1.38
15	2	160	10	200	14.06	11.25
16	10	160	10	200	21.56	11.88
17	2	90	7	125	19.03	9.63
18	10	90	7	125	23.84	10.94
19	6	20	7	125	35.88	1.69
20	6	160	7	125	17.06	10.94
21	6	90	4	125	10.63	8.00
22	6	90	10	125	22.50	12.50
23	6	90	7	50	21.66	10.50
24	6	90	7	200	23.19	11.81

Tab. 11. Regression analysis of experimental data

Regression equation	Significance indices
ε_{Zn}=20.40 +4.92X_1-8.82X_2 +2.55X_3+1.71X_4 +1.03X_1^2+6.57X_2^2–3.84X_4^2+2.02X_2^4-2.19 X_1X_2-2.77X_1X_3-2.53X_2X_3-1.02X_2X_4-0.61X_3X_4	R^2 = 0.9348; S_{ad} = 17.71; F = 69.49
ε_{Pb}=11.10+0.35X_1+3.46 X_2+1.35X_4 – 0.79X_1^2 - 5.061X_2^2-0.82X_3^2+ +0.64X_1X_2-0.55X_1X_3+0.16X_1X_4 - 1.06X_2X_3+1.45X_2X_4+1.24X_3X_4	R^2 = 0,9254; S_{ad} = 3.69; F = 29.06

Note: dimensionless variables are determined from the expressions:

$$X_1 = \frac{C_{H_2SO_4}-6}{4};\ X_2 = \frac{C_{NaCl}-90}{70};\ X_3 = \frac{(L:S)-7}{3};\ X_4 = \frac{f-125}{75}; \tag{5}$$

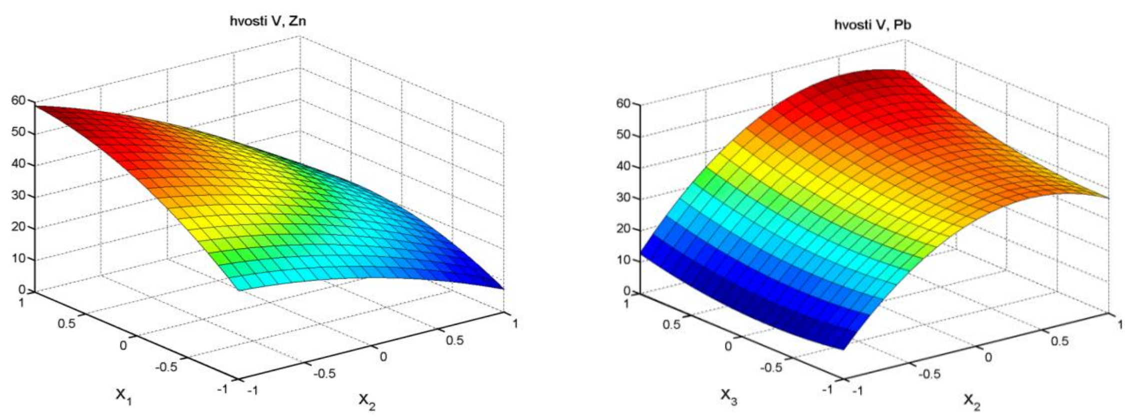

Fig. 9. Results of leaching ore in the disintegrator: a) zinc; b) lead

DOI 10.2478/ama-2019-0016

On the next stage, parameters of reagent leaching of tailings in the disintegrator are investigated (Table 12 and 13, Fig. 10).

Tab. 12. Results of leaching tailings in the disintegrator

#	Reagent content, g/l		L:S ratio	Rotor rpm, Hz	Recovery into solution, ε, %	
	H_2SO_4	NaCl			Zn	Pb
1	2	20	4	50	26.95	0.33
2	10	20	4	50	78.74	0.95
3	2	160	4	50	10.95	27.14
4	10	160	4	50	27.37	40.50
5	2	20	10	50	47.37	4.76
6	10	20	10	50	54.74	1.79
7	2	160	10	50	6.32	40.48
8	10	160	10	50	15.79	35.71
9	2	20	4	200	32.42	0.71
10	10	20	4	200	61.47	1.43
11	2	160	4	200	13.47	27.14
12	10	160	4	200	27.37	40.00
13	2	20	10	200	42.11	5.95
14	10	20	10	200	52.63	1.55
15	2	160	10	200	12.63	44.05
16	10	160	10	200	65.26	18.38
17	2	90	7	125	22.11	39.17
18	10	90	7	125	36.11	28.33
19	6	20	7	125	58.95	1.67
20	6	160	7	125	23.58	47.50
21	6	90	4	125	35.37	34.29
22	6	90	10	125	29.47	42.86
23	6	90	7	50	32.42	38.33
24	6	90	7	200	26.53	40.83

Tab. 13. Regression analysis of experimental data

Regression equation	Significance indices
$\varepsilon_{Zn}=32.15+11.4X_1-14.04X_2+0.68X_3+1.85X_4-2.90X_1^2+9.25X_2^2-2.53X_4^2-0.39X_1X_2-1.95X_1X_3+1.32X_1X_4+1.47X_2X_3+4.84X_2X_4+3.61X_3X_4$	$R^2 = 0.8277$; $S_{ad} = 143.62$; $F = 18.06$
$\varepsilon_{Pb}=39.44-1.17X_1+16.76X_2+1.28X_3-0.55X_4-5.64X_1^2-14.81X_2^2-0.86X_3^2-4.09X_1X_3-1.42X_1X_4-0.42X_2X_3-1.00X_2X_4-0.82X_3X_4$	$R^2 = 0.9483$; $S_{ad} = 35.09$; $F = 44.58$

Note: dimensionless variables are determined from the expressions:

$$X_1 = \frac{C_{H_2SO_4}-6}{4};\ X_2 = \frac{C_{NaCl}-90}{70};\ X_3 = \frac{(L:S)-7}{3};\ X_4 = \frac{f-125}{75}; \quad (6)$$

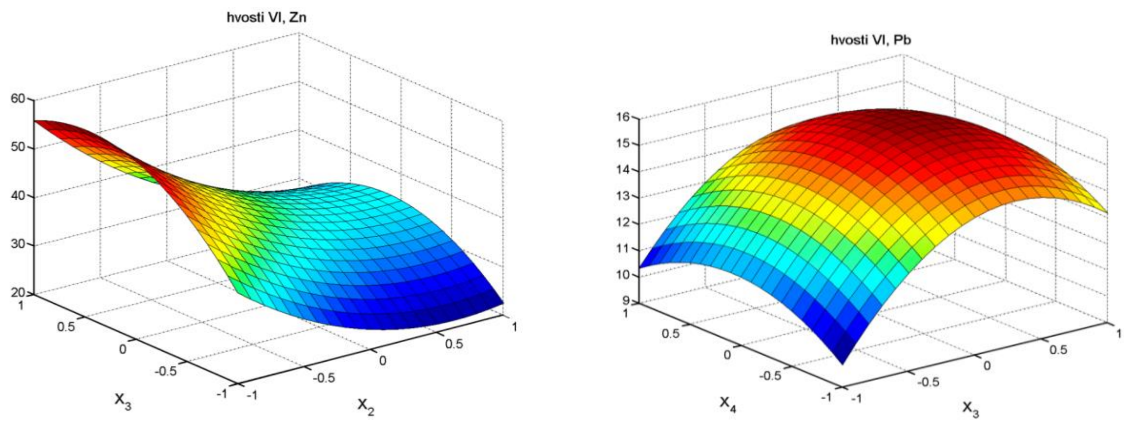

Fig. 10. Results of leaching tailings in the disintegrator: a) zinc; b) lead

Recovery of metals into solution in the disintegrator is equal during the time period by two orders of magnitude less than under agitation leaching.

6. DISCUSSION OF MATERIALS

To interpret the results of reaching, the method of linear multiple regression analysis is used. One parameter is variable, the rest are averaged in the intervals for Sadon ores: the content of H_2SO_4, g/dm^3, 6; the content of NaCl, g/ dm^3, 90; L:S ratio = 7; the leaching time T, h, 0.625; the rotor rpm, Hz = 125.

Recovery of metals into solution depending on the sulfuric acid concentration is interpreted by the graph in Fig. 11.

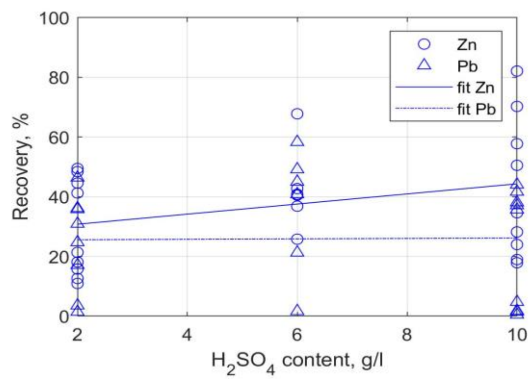

Fig. 11. Parameters of leaching metals by sulfuric acid

DOI 10.2478/ama-2019-0016 acta mechanica et automatica, vol.13 no.2 (2019)

You can see a sharp difference in leaching zinc (25–28%) and lead (25–80%) under equal concentration of the acid.

The parameters of recovery of metals by sodium chloride are interpreted by the graph in Fig. 12.

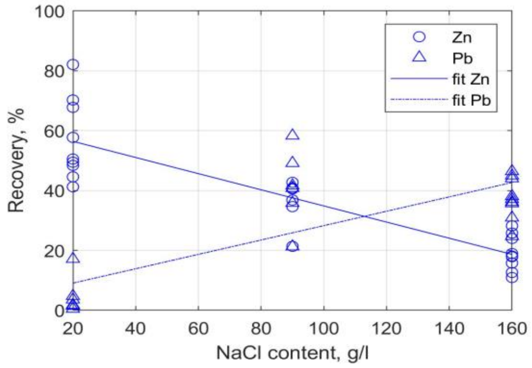

Fig. 12. Parameters of recovery of metals by sodium chloride

Recovery of lead and zinc into solution by sodium chloride is characterized by asymmetry of graphs with intersection in the range of values of 120 g/dm³.

The parameters of recovery of metals depending on L:S ratio are interpreted by the graph in Fig. 13.

The L:S ratio influences metal recovery into solution in a dramatically different way. While this index remains almost the same for zinc, it increases greatly for lead.

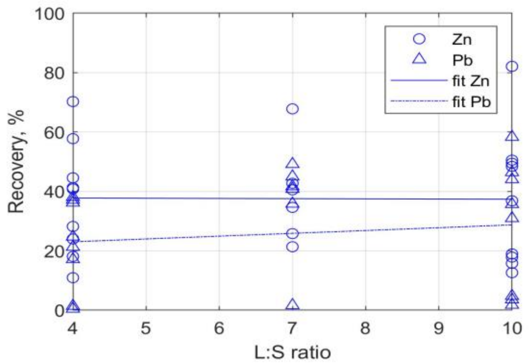

Fig. 13. Parameters of recovery of metals depending on the L:S ratio

The parameters of recovery of metals depending on time of leaching are interpreted by the graph in Fig. 14.

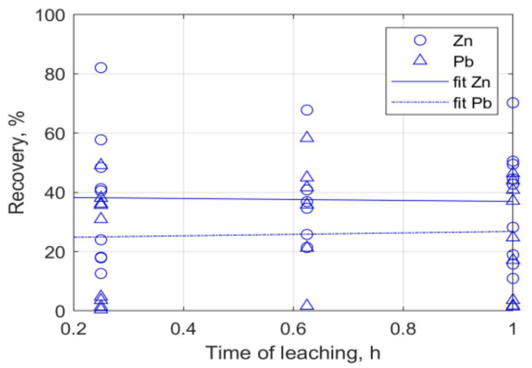

Fig. 14. Parameters of recovery of metals depending on time

While in the case of lead recovery, intensity increases with time, it reduces significantly for zinc.

The parameters of recovery of metals by sulfuric acid in the disintegrator are interpreted by the graph in Fig. 15.

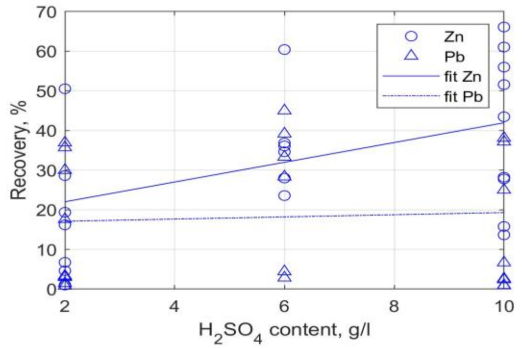

Fig. 15. Parameters of recovery of metals by sulfuric acid in the disintegrator

Orientation graphs of recovery coincide if the activity of zinc is much greater. The parameters of recovery into solution by sodium chloride in the disintegrator are interpreted by the graph in Fig. 16. Recovery of lead and zinc into solution by sodium chloride is characterized by asymmetry of graphs with intersection in the range of values of 140 g/dm³.

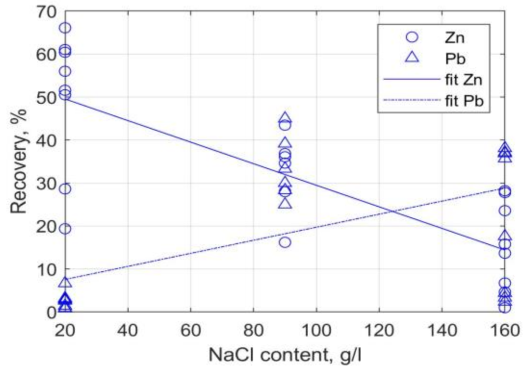

Fig. 16. Parameters of recovery of metals by sodium chloride in the disintegrator

The parameters of recovery of metals depending on the L:S ratio are interpreted by the graph in Fig. 17.

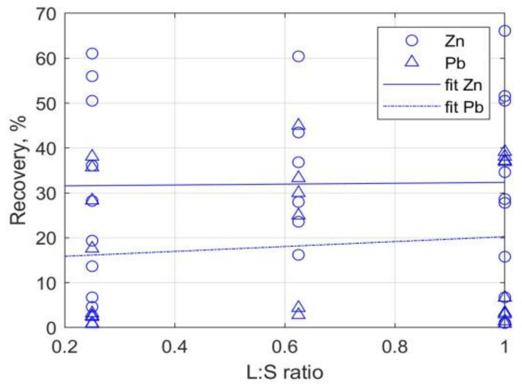

Fig. 17. Parameters of recovery of metals depending on the L:S ratio

DOI 10.2478/ama-2019-0016

Orientation of the parameters of recovery of metals depending on the L:S ratio is different with lead being more active (Fig. 18).

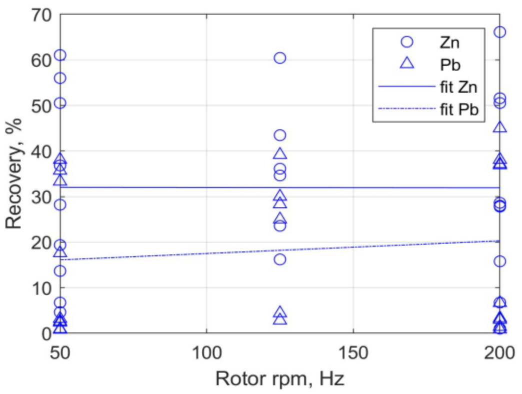

Fig. 18. Parameters of recovery of metals depending on the rotation velocity

The parameters of recovery of metals depending on the rotation are of the same orientation, while activity increases with the same pace.

Activation of materials in the disintegrator with subsequent leaching outside it increases metal recovery in comparison with conventional leaching:

- zinc leaching from concentration tailings by the factor of 1.36 and lead leaching by the factor of 1.13;
- zinc leaching from off-balanced ore by the factor of 1.63, and zinc leaching by the factor of 2.09.

The time period of leaching with simultaneous disintegration makes the first seconds. At the same time, the duration of agitation leaching changes from 15 to 60 minutes, that is, by two orders of magnitude higher.

The obtained results correspond to papers on mining modernization as for the environment and resource saving issues (Jarvie-Eggart, 2015; Sekisov et al., 2016; Komashchenko et al., 2016; Morozov and Yakovlev, 2016).

7. CONCLUSIONS

Recovery of metals into solution is close to the maximum and coincides:

- under agitation leaching of tailings and ore (Series 1);
- under agitation leaching of tailings or ore previously activated in the disintegrator with the leaching solution (Series 4).

Under agitation leaching of tailings or ore previously activated in the dry condition (Series 2) or under leaching of tailings or ore previously passed through the disintegrator once (Series 3), much fewer metals recover into solution.

Recovery of metals into solution is the same both under multiple leaching of tailings or ore in the disintegrator and agitation leaching of tailings or ore previously activated in the disintegrator with leaching solutions. The time of agitation leaching is more by two orders of magnitude than that of the disintegrator processing.

Recovery of metals into solution is most affected by the content of sodium chloride in the solution. Then, in decreasing order go the content of sulfuric acid in the solution, the disintegrator rotor rpm and L:S ratio. Zinc is easier to leach than lead.

The obtained regression equations adequately describe the experimental data with the significance level of 0.05 as the calculating values of the Fischer coefficient exceed their table values for each regression equation.

The content of lead and zinc in the solution almost coincides: under agitation leaching of tailings and ore (Series 1); under agitation leaching of tailings or ore previously activated in the disintegrator with solutions (Series 4). Under agitation leaching of tailings or ore previously activated in the dry condition (Series 2) or under leaching of tailings or ore in the disintegrator (Series 3), recovery of metals into solution is much less than in Series 5 and that confirms the expedience of changing the disintegrator design in order to increase the time period of activation in the disintegrator.

REFERENCES

1. **Cetintas, S., Yildiz, U., Bingol, D.** (2018), A novel reagent-assisted mechanochemical method for nickel recovery from lateritic ore, *Journal of Cleaner Production*, 199, 616–632.
2. **De Oliveira D.M., Sobral L.G.S., Olson G.J., Olson S.B.** (2014), Acid leaching of a copper ore by sulphur-oxidizing microorganisms, *Hydrometallurgy*, 147-148, 223–227.
3. **Dmitrak Yu.V., Kamnev Ye.N.** (2016), The leading design and scientific-research institute of industrial technology – the way 65 years long (in Russian), *Mining Journal*, 3, 6–12.
4. **Fan, E., Li, L., Zhang, X., Bian, Y., Xue, Q., Wu, J., Wu, F., Chen, R.** (2018), Selective Recovery of Li and Fe from Spent Lithium-Ion Batteries by an Environmentally Friendly Mechanochemical Approach, *ACS Sustainable Chemistry & Engineering*. 6 (8), 11029–110315.
5. **Gazaleyeva G.I., Mamonov S.B., Bratygin Ye.V., Klyushnikov A.M.** (2017), Problems and innovative solutions in technogenic materials concentration (in Russian), *GIAB*, 1, 257–272.
6. **Ghorbani Y., Franzidis J.P., Petersen J.** (2016), Heap leaching technology – current State, innovations, and future directions: a review, *Mineral Processing and Extractive Metallurgy Review*, 37(2), 73–119.
7. **Golik V., Komaschenko V., Morkun V., Khasheva Z.** (2015d),The effectiveness of combining the stages of ore fields development, *Metallurgical and Mining Industry*, 5, 401–405.
8. **Golik V., Komashchenko V., Morkun V.** (2015b), Innovative technologies of metal extraction from the ore processing mill tailings and their integrated use, *Metallurgical and Mining Industry*, 3, 49–52.
9. **Golik V., Komashchenko V., Morkun V.** (2015c), Feasibility of using the mill tailings for preparation of self-hardening mixtures, *Metallurgical and Mining Industry*, 3, 38–41.
10. **Golik V., Komashchenko V., Morkun V.** (2015a), Geomechanical terms of use of the mill tailings for preparation, *Metallurgical and Mining Industry*, 4, 321–324.
11. **Golik V.I.** (2013), Conceptual approaches to creating low- and non-waste mining based on combination of physical-technical and physical-chemical geotechnologies (in Russian), *Mining Journal*, 5, 93–97.
12. **Golik, V.I., Stradanchenko, S.G., Maslennikov, S.A.** (2015e), Experimental study of non-waste recycling tailings of ferruginous quartzites, *International Journal of Applied Engineering Research*, 10 (15), 35410–35416.
13. **Granata, G., Takahashi, K., Kato, T., Tokoro, C.** (2018), Mechanochemical activation of chalcopyrite: Relationship between activation mechanism and leaching enhancement, *Minerals Engineering*. 131, 280–285.
14. **Jarvie-Eggart M.E.** (2015), *Responsible Mining: Case Studies in Managing Social and Environmental Risks in the Developed World.*

Englewood, Colorado: Society for Mining, Metallurgy and Exploration.
15. **Jordens A., Cheng Y.P., Waters K.E.** (2013), A review of the beneficiation of rare earth element bearing minerals, *Minerals Engineering*, 41, 97–114.
16. **Khint Y.** (1981), *Uda-technology. Special design-technological bureau Disintegrator* (in Russian), Tallinn: Valgus.
17. **Komashchenko V.I., Vasilyev P.V., Maslennikov S.A.** (2016), Reliable raw material base of underground mining of KMA deposits (in Russian), Izvestiya TulGU. Earth Sciences, 2, 95–101.
18. **Liu J., Han Y., Li Y., Zhang S.** (2012), Study on mechanism and technology of deep reduction for iron ore leaching, The 26th International Mineral Processing Congress, *IMPC 2012: Innovative Processing for Sustainable Growth*, New Delhi, India. 2335–2343.
19. **Lyashenko V.I., Franchuk V.P., Kislyi B.P.** (2015), Modernization of the technical and technological complex of uranium mining (in Russian), *Mining Journal*, 1, 26–32.
20. **Minagawa, M., Hisatomi, S., Kato, T., Granata, G., Tokoro, C.** (2018), Enhancement of copper dissolution by mechanochemical activation of copper ores: Correlation between leaching experiments and DEM simulations, *Advanced Powder Technology*, 29 (3), 471–478.
21. **Morkun, V., Tron, V.** (2014), Ore preparation energy-efficient automated control multi-criteria formation with considering of ecological and economic factors, *Metallurgical and Mining Industry*, 5, 8–10.
22. **Morozov, A.A, Yakovlev, M.V.** (2016), Processing of off-balance uranium ores formed in mining Streltsovo ore deposit (in Russian), *GIAB*, 12, 174–181.
23. **Sekisov A.G., Shevchenko Yu.S., Lavrov A.Yu.** (2016), Prospects of mine leaching in mining gold ore deposits (in Russian), *FTPRRMPI*, 1, 110–116.
24. **Sinclair L., Thompson J.** (2015), In situ leaching of copper: Challenges and future prospects, *Hydrometallurgy*, 157, 306–324.
25. **Wang H., He Y., Duan C., Zhao Y., Tao Y., Ye C.** (2015), Development of Mineral Processing Engineering Education in China University of Mining and Technology, *Advances in Computer Science and Engineering*, 141, 77–83.
26. **Wang, M., Tan, Q., Li, J.** (2018), Unveiling the role and mechanism of mechanochemical activation on lithium cobalt oxide powders from spent lithium-ion batteries, *Environmental Science & Technology*, 52(22), 13136–13143.
27. **Xie, H., Zhang, L., Li, H., Koppala, S., Yin, S., Li, S., Yang, K., Zhu, F.** (2019), Efficient recycling of Pb from zinc leaching residues by using the hydrometallurgical method, *Materials research express*, 6(7), DOI: 10.1088/2053-1591/ab11b9.
28. **Yang, Y., Zheng, X., Cao, H., Zhao, C., Lin, X., Ning, P., Zhang, Y., Jin, W., Sun, Z.** (2017), A Closed-Loop Process for Selective Metal Recovery from Spent Lithium Iron Phosphate Batteries through Mechanochemical Activation, *ACS Sustainable Chemistry & Engineering*, 5 (11). 9972–9980.
29. **Zhang, D., Ling, H.; Yang, T., Liu, W.; Chen, L.** (2019), Selective leaching of zinc from electric arc furnace dust by a hydrothermal reduction method in a sodium hydroxide system, *Journal of Cleaner Production*, 224, 536–544.

DOI 10.2478/ama-2019-0017

SURFACE LOCALIZED HEAT TRANSFER IN PERIODIC COMPOSITES

Dorota KULA,* Ewaryst WIERZBICKI*

*Faculty of Civil Engineering and Environmental Sciences, Department of Civil Engineering, Warsaw University of Life Sciences, ul. Nowoursynowska 166, 02-787 Warszawa, Poland

kuladorota@wp.pl, el_el@o2.pl

received 18 April 2019, revised 23 June 2019, accepted 26 June 2019

Abstract: A characteristic feature of the description of physical phenomena formulated by an appropriate boundary or initial-boundary value problem and occurring in microstructured materials is the investigation of the unknown field in the form of decomposition referred to as micro-macro hypothesis. The first term of this decomposition is usually the integral average of the unknown physical field. The second term is a certain disturbance imposed on the first term and is represented in the form of a finite or infinite number of singleton fluctuations. Mentioned expansion is usually referred to as a two-scale expansion of the unknown physical field. In the paper, we purpose to apply two-scale expansion in the form of a certain Fourier series as a result of an applying Surface Localization of the unknown field. The considerations are illustrated by two examples, which results in analytical approximated solutions to the Effective Heat Conduction Problem for periodic composites, including the full dependence on the microstructure length parameter.

Key words: Heat transfer, periodic composites, homogenized model

1. INTRODUCTION

The procedure that is proposed in this paper can be treated as a certain variant of the Tolerance Averaging Technique (*TAT*) (Woźniak and Wierzbicki, 2000; Jędrysiak, 2010; Michalak, 2010; Ostrowski, 2017) or as an alternative purpose to the forming of two-scale expansions (Ariault, 1983; Bensoussan et al., 2011), proposed as a micro-macro representation of the unknown physical fields (Woźniak and Wierzbicki, 2000; Jędrysiak, 2010; Michalak, 2010; Ostrowski, 2017). Obtained in the subsequent considerations equivalent reformulation of Heat Transfer Equation (*HTE*) uses Fourier expansion as a representation of the temperature field and consists of: (1) a single equation for average temperature as for the first term of the mentioned expansion, (2) infinite number of equations for Fourier coefficients (amplitudes), and 3) finite number of tolerance amplitudes. Fourier basis taken into account in the proposed approach includes the possible changes of the composite periodicity along directions perpendicular to the periodicity directions. Hence, we can also deal with the FGM-type periodicity (Woźniak et al., 2002), similar to the twin but approximately original tolerance description of composite behaviours developed in Woźniak et. al. (2002), and continuators (Woźniak and Wierzbicki, 2000; Ostrowski, 2017). The sum of Fourier fluctuating terms (without the first term equal to the average temperature) can be interpreted as the analytical formula for the error made in using the approximate solutions of *HTE* proposed in *TAT* approach.

The starting point of considerations is the known parabolic heat transfer equation:

$$\nabla^T(K\nabla\theta) - c\dot{\theta} = b \tag{1}$$

in which, the region $\Omega \subset R^D$, $2 \le D \le 3$, occupied by the composite is restricted to the form:

$$\Omega = \Omega_d \times \Omega_{D-d} \tag{2}$$

in which, 1° $\Omega_d = (0, L)$, $\Omega_{D-d} = (0,\delta_1)\times(0,\delta_2)$ while $(d,D) = (1,3)$, 2° $\Omega_d = (0,L_1)\times(0,L_2)$, $\Omega_{D-d} = (0,\delta)$ while $(d,D) = (2,3)$, and 3° $\Omega_d = (0,L)$, $\Omega_{D-d} = (0,\delta)$ while $(d,D) = (1,2)$ for $L_1, L_2, L, \delta_1, \delta_2, \delta > 0$. In (2), $\theta = \theta(y,z,t)$, $y \in \Omega_d \subset R^d$, $z \in \Omega_{D-d} \subset R^{D-d}$, $t \ge 0$, denotes the temperature field, c is a specific heat and k is the heat conductivity constant matrix. Moreover, $\nabla \equiv \nabla_d + \nabla_{D-d}$ for $\nabla_d \equiv [\partial/\partial y^1, \dots, \partial/\partial y^d, 0, \dots, 0]^T$ with zeros placed in the last $D-d$ positions and $\nabla_{D-d} \equiv [0, \dots, 0, \partial/\partial z^1, \dots, \partial/\partial z^{D-d}]^T$ with zeros placed in the first d positions. Both fields $c = c(\cdot)$ and $k = k(\cdot)$ take S values c^1, ..., c^S and k^1, ..., k^S, respectively, do not depend on the temperature field θ and are restricted to Ω_d of a certain periodic field defined in R^d. Hence, considerations of the paper are restricted to Δ-periodic composites. Diameter $diam(\Delta)$ of repetitive cell is not necessarily small where compared to the characteristic length dimension L of the region Ω. With dimensionless scale parameter $\lambda = diam(\Delta)/L$, we will control the analysed equations in the subsequent considerations. The Δ- periodicity of the composite means that there exists σ-tuple $(\mathbf{v}^1, \dots, \mathbf{v}^d)$ of independent vectors $\mathbf{v}^1, \dots, \mathbf{v}^d \in R^d$ determining d directions of periodicity such that: (*i*) points $x + k_1\mathbf{v}_1 + \dots + k_d\mathbf{v}_d$, $-0.5 < k_1$, $k_d < 0.5$, cover for the interior of the cell $\Delta(x)$, (*ii*) $\Delta = \Delta(x_0)$ for fixed $x_0 \in R^3$ and (*iii*) $c(x+\mathbf{v}) = c(x)$, $K(x+\mathbf{v}) = K(x)$ for an arbitrary $\mathbf{v} \in \{\mathbf{v}_1, \dots, \mathbf{v}_d\}$, $x \in R^3$. The averaging $\langle f\rangle(x)$, $x \equiv (y,z)$, of an arbitrary integrable field f is defined by :

$$\langle f\rangle(x) = \frac{1}{|\Delta|}\int_\Delta f(\xi)d\xi \tag{3}$$

and is a constant field provided that f is Δ-periodic.

2. REFORMULATION PROCEDURE

The investigations are based on the two fundamental assumptions. The first modelling assumption is a certain extension of the micro-macro hypothesis introduced framework of the tolerance averaging technique (Ariault, 1983; Bensoussan et al., 2011; Woźniak and Wierzbicki, 2000; Jędrysiak, 2010; Michalak, 2010; Ostrowski, 2017). In accordance with that hypothesis, the temperature field θ can be approximated with an acceptable accuracy by formula:

$$\theta_M(z) = \vartheta(z) + h^A(x)\psi_A(z) \tag{4}$$

in which, the slowly varying fields $\vartheta(\cdot)$ and $\psi_A(\cdot)$ are referred to as tolerance averaging of temperature field and amplitude fluctuations fields, respectively. Here and in the sequel, the summation convention holds with respect to indices $A = 1, \dots, N$. Symbols h^A, $A = 1, \dots, N$, used in (5) denote tolerance shape functions that should be periodic and satisfy conditions:

$$h^A \in o(\lambda), \lambda\nabla_y h^A \in o(\lambda), \langle ch^A\rangle = 0, \langle Kh^A\rangle = 0 \tag{5}$$

Usually, RHS of (4) is called Micro-Macro Decomposition of the temperature field. For particulars, the reader is referred to (Bensoussan et al., 2011; Woźniak and Wierzbicki, 2000; Jędrysiak, 2010). We interpret in (5), $\theta_{long} = \vartheta$ and $\theta_{short} = h^A(x)\psi_A(z)$. The tolerance-micro macro hypothesis can be formulated in the form:

Micro-Macro Hypothesis. The residual part of the temperature field θ_{res} being the difference between the temperature field θ and its tolerance part θ_M given by (4) can be treated as zero, $\theta_{res} \equiv \theta - \theta_M \approx 0$, that is, it vanish with an acceptable 'tolerance approximation'. The tolerance temperature part θ_M is debarked from the temperature field θ by the micro-macro hypothesis as an approximation of this field leading to the equation for the average temperature controlled by the finite number of fluctuation amplitudes $\psi_A(\cdot)$. We intend to supplement this micro-macro approximation to the complete temperature field θ interpreting decomposition:

$$\theta \equiv \theta_M + \theta_{res} \tag{6}$$

as a temperature field representation in with θ_{res} adding as the error made, while micro-macro decomposition (6) is used as tolerance approximation of the temperature field.

Taking into account the intention of adapting the idea implemented in the theory of signals, where we are dealing with the 'overlap' of many signals controlled by various parameters, we will try to impose onto decomposition (6) the interpretation dictated by the modified micro-macro hypothesis.

Modified Micro-Macro Hypothesis. The composite temperature field θ awards LS-decomposition onto the sum:

$$\theta \equiv \theta_L + \theta_S \tag{7}$$

of the long-wave part θ_L (L-part) and short-wave part θ_S (S-part), both sufficiently regular, which determine the disappearing heat flux vector component by:

$$(q_S)_n \equiv k(\nabla\theta_S)_n = 0 \tag{8}$$

normal to Γ, and hence, corresponding to:

$$\theta_{\acute{S}}(y,z,t) \equiv \theta(y,z,t) - \theta_L(y,z,t) = a_p(z,t)\varphi^p(y,z) \tag{9}$$

as a certain orthogonal Fourier expansion representation of θ_S independent on thermal, material and geometrical composite properties. In restriction (8), allowing the use of the Fourier series in the unit vector field $n = n(x)$ is normal to discontinuity surfaces Γ in regular points x placed on Γ. Moreover, in (9), summation convention holds with respect to positive integer p. Moreover, decomposition (6) has been implemented in various ways. Modified micro-macro hypothesis will be supplemented with two remarks.

Remark. 1. If the orthogonality of Δ-periodic Fourier basis $\varphi^p(x)$, $p = 1,2, \dots$, is related to the scalar product $f_1 \circ f_2 = \langle f_1 f_2\rangle = \sum_{s=1}^{S} \eta_s \langle f_1 f_2\rangle_s$ using the `averaged values $\langle f_1 f_2\rangle_s$ taken over materially homogeneous parts Δ_s of the repetitive cell $\Delta \subset R^d$, then Fourier basis $\varphi^p(x)$ can be treated as independent on the material structure of the composite.

Remark. 2. Tolerance temperature approximation (4) is a certain temperature *L*-part θ_L provided that corresponding L-part $(q_M)_n \equiv n^T K\nabla\theta_M$ of heat flux normal component $(q)_n \equiv n^T K\nabla\theta$ is continuous on Γ. In this case, expansion (9) is equal to the error made under using $\theta_L = \theta_M$ as an approximation of θ. Moreover, the expansion:

$$\theta = \vartheta + \lambda[g^A\psi_A + a_p(z,t)\phi^p(y,z)] \tag{10}$$

is a certain temperature representation formed for $h^A(x,t) \equiv \lambda g^A(\lambda^{-1}x)$ and $\varphi^p(x,t) \equiv \lambda\phi^p(\lambda^{-1}x)$ and for:

$$\vartheta = a_0 + \theta_{res} - \lambda g^A\psi_A \tag{10}$$

together with two additional conditions for:

$$\begin{aligned}&\langle c\phi^p\rangle = 0, \langle k\phi^p\rangle = 0, p = 1,2, \dots,\\ &\langle cg^A\rangle = 0, \langle kg^A\rangle = 0, A = 1,2, \dots, N.\end{aligned} \tag{11}$$

formulated under *Remark* 1.

We are to superimpose on the LS-decomposition a special interpretation in the framework, of which the composite behaviours being a direct consequence of the occurrence of the material discontinuity surfaces is described exclusively by the second term θ_S of $\theta \equiv \theta_L + \theta_S$ in (7) debarked from θ as supported on the ε-ribbon surrounding surfaces of material discontinuities of a composite, while the part θ_L of $\theta \equiv \theta_L + \theta_S$ does not notice the presence of a heterogeneous composite structure. Hence, the mentioned decomposition includes the natural decomposition of θ on a long-wave and a short-wave parts taken with respect to λ and localized inside and outside of the thin ε-ribbon surrounding surfaces of material discontinuities of a composite, respectively. Thus, decomposition $\theta \equiv \theta_L + \theta_S$ provides the ability to perform tolerance modeling procedure with respect to the field $u = \langle\vartheta\rangle$ as the average temperature field, and to the fields $\psi_A(\cdot)$ and $a_p(\cdot)$ as fluctuation amplitudes referred to as the tolerance and Fourier amplitudes, respectively, and also in relation to the new parameter ε as well as with respect to the small parameter λ. The aim of the paper is to overview the two-scale expansion (10) under its ε-asymptotic with respect to $\varepsilon \to 0$. As a result, we are to obtain an equivalent reformulation of *HTE* and then discuss the possibility to develope on this way the Effective Heat Conduction Equation in the form of a single equation for average temperature.

In order to realize the aim of the paper, we are to show that the following hypothesis holds.

Locality Hypothesis. The *L*-part θ_L of the temperature field can be supported on the ε-ribbon $o_\varepsilon(\Gamma)$ surrounding the discontinuity surfaces Γ, that is, $\theta_L(y,z,t) \neq 0$ for $(y,z) \in o_\varepsilon(\Gamma)$ and $\theta_L(y,z,t) = 0$ for $(y,z) \in \Omega \backslash o_\varepsilon(\Gamma)$ with the additional restriction $\nabla\theta_L(y,z,t) = 0$ satisfied for $(y,z) \in \Gamma \cup \partial o_\varepsilon(\Gamma)$ while.

DOI 10.2478/ama-2019-0017

Locality hypothesis means that limit passage:

$$\theta_L = (\theta_L)_\varepsilon \to u \tag{12}$$

can be properly realized under $\varepsilon \to 0$. Formulating conditions sufficient for the average temperature u to coincide with its integral counterpart $u = \langle\theta\rangle$ is an open mathematical problem. This remark can be treated as a certain comment to the suggestions to compare effective modulus obtained as results of various methods of temperature averaging.

3. SURFACE LOCALIZATION PROCEDURE

Both L-part and *S*-part of the temperature θ depend on the parameter ε. In formal representation of the temperature *L*-part in the form of micro-macro decomposition, we are to adjust as the form of difference $\langle\theta_L\rangle(y,z,t) - \theta_L(y,z,t)$ to understanding its limit passage behaviour while $\varepsilon \to 0$. To this end, denoted by $\pi_\Gamma(y,z)$, the orthogonal projection of (y,z) onto Γ (well defined if (y,z) is placed sufficiently close to Γ). Let symbols n_A, $A = 1,\dots,S$, form the sequence of unit vector fields normal to $\partial\Delta_A \subset \Gamma$ and directed to the interior of Δ_A. Hence, $n_A(y,z) = -n_B(y,z)$ for $(y,z) \in \partial\Delta_A \cap \partial\Delta_B$ provided that Δ_A meets Δ_B along the fragment $\partial\Delta_A \cap \partial\Delta_B$ of Γ. Denoted by $\pi_S \subset \{(A,B): A,B = 1,\dots,S, A \neq B\}$, the set of all pairs (A,B) for which regions Δ_A and Δ_B are in contact with the surface panel $\partial\Delta_A \cap \partial\Delta_B \neq \emptyset$. Bearing in mind that $\langle\theta_L\rangle = \langle\theta\rangle$ is a differentiable function of ε, we arrive at:

$$\theta(y,z,t) = \langle\theta_L\rangle(z,t) + \frac{d\langle\theta_L\rangle}{d\varepsilon}\varepsilon + \theta_S + o(\varepsilon) \tag{13}$$

for sufficiently small $\varepsilon > 0$. Using decomposition $\frac{\partial}{\partial n_A} = v_A^y\nabla_y + v_A^z\nabla_z$ with respect to the orthogonal directions of y and z variables and $n_A = v_A^y n_y^A + v_A^z n_z^A$ as well as denotations:

$$\begin{aligned}
&\psi_{(A,B)}^{(y)}(y,z,t) \equiv \langle(\nabla_y\theta_L)_A\rangle_{\partial\Delta_A\cap\partial\Delta_B}(y,z,t),\\
&\psi_{(A,B)}^{(y)}(y,z,t) \equiv \langle(\nabla_z\theta_L)_A\rangle_{\partial\Delta_A\cap\partial\Delta_B}(y,z,t),
\end{aligned} \tag{14}$$

for tolerance amplitudes and:

$$\begin{aligned}
&h_{(y)}^{(A,B)}(y,z)\\
&= -\eta_A(y,z)v_A^y(\pi_\Gamma(y,z))\frac{[\![k]\!]_{(A,B)}}{k_B}\frac{|\partial\Delta_A\cap\partial\Delta_B|}{|\partial\Delta_A|},\\
&h_{(z)}^{(A,B)}(y,z)\\
&= -\eta_A(y,z)v_A^z(\pi_\Gamma(y,z))\frac{[\![k]\!]_{(A,B)}}{k_B}\frac{|\partial\Delta_A\cap\partial\Delta_B|}{|\partial\Delta_A|},
\end{aligned} \tag{15}$$

for tolerance shape functions in which $[\![k]\!]_{(A,B)} \equiv k_A - k_B$, we arrive at:

$$\begin{aligned}
&\langle\theta_L\rangle(z,t) - \theta_L(y,z,t) =\\
&= \textstyle\sum_{A,B\in\pi_S}[h_{(y)}^{(A,B)}(y,z,t)\psi_{(A,B)}^{(y)}(z,t) +\\
&+h_{(y)}^{(A,B)}(y,z,t)\psi_{(A,B)}^{(y)}(z,t)] + o(\varepsilon)
\end{aligned} \tag{16}$$

Hence (15) becomes Δ-periodic functions and (16) loses dependence of $\psi_{(A,B)}^{(y)}$ and $\psi_{(A,B)}^{(y)}$ on y-variable, while $\varepsilon \to 0$. Moreover, $v_A^z = 0$ for homogeneous periodicity. Cell distribution will be restricted to that introduced by the following:

Cell distribution hypothesis. For any periodic composite there exists cell distribution $\Delta(y,z)$, $(y,z) \in \Omega$, for which saturations η_A do not depend on y-variable.

Under rescaling:

$$g_{(\gamma)}^{\omega}(y,z) \equiv \lambda h_{(\gamma)}^{\omega}(\lambda^{-1}y,z) \quad for \quad \gamma = y,z \tag{17}$$

condition $\lim_{\varepsilon\searrow 0}\langle v_A^y(\pi_\Gamma(y,z))\rangle = 0$ reduces expansion (16) to:

$$\begin{aligned}
&\theta(y,z,t) = \langle\theta_L\rangle(z,t) + \lambda[g_{(z)}^{\omega}(y,z)\psi_\omega^{(z)}(z,t) +\\
&+a_p(z,t)\phi^p(y,z)] + o(\varepsilon)
\end{aligned} \tag{18}$$

In (18) summation over $\omega \equiv (A,B) \in \pi_S$ and over positive integer p holds. Bearing in mind that:

$$\vartheta = a_0 + \theta_{res} - \lambda g^A\psi_A \tag{19}$$

together with two additional conditions:

$$\begin{aligned}
&\langle c\phi^p\rangle = 0, \langle k\phi^p\rangle = 0, p = 1,2,\dots,\\
&\langle cg^A\rangle = 0, \langle kg^A\rangle = 0, A = 1,2,\dots,N.
\end{aligned} \tag{20}$$

we conclude that limit passage:

$$\theta_L = (\theta_L)_\varepsilon \to u \tag{21}$$

is properly realized under $\varepsilon \to 0$. Denote by H quadratic matrix with components $\langle k\nabla^T{}_y g_{(y)}^v, k\nabla_y g_{(z)}^\mu\rangle$. By applying orthogonalization procedure, one can arrive at the Surface Localized Heat Transfer Model equations (Kula, 2015; Kula and Wierzbicki, 2015, Woźniak et al., 2002; Wodzyński et al., 2018):

$$\begin{aligned}
&\langle c\rangle\dot{u} - \nabla^T(\mathbb{k}_{surf}[\nabla u] + [k]_{surf}{}^p a_p) = -\langle b\rangle\\
&\lambda^2(\langle\phi^p c\phi^q\rangle\dot{a}_q - \nabla_z{}^T\langle\phi^p c\phi^q\rangle\nabla_z a_q) +\\
&+2\lambda s^{pq}\nabla_z a_q + \{k\}_{surf}{}^{pq}a_p = L_a^\lambda[u]
\end{aligned} \tag{22}$$

In (22):

$$\begin{aligned}
&\mathbb{k}_{surf} = \langle k\rangle - \langle k\nabla^T{}_y g_{(y)}^v, k\nabla_y g_{(z)}^v\rangle(H^{-1})_{v\mu}\begin{bmatrix}\langle\nabla_y{}^T g_{(y)}^\mu k\rangle\\ \langle\nabla_y{}^T g_{(z)}^\mu k\rangle\end{bmatrix},\\
&[k]_{surf} = k\langle\nabla^T\phi^p\rangle -\\
&-\langle k\nabla^T{}_y g_{(y)}^v, k\nabla_y g_{(z)}^v\rangle(H^{-1})_{v\mu}\begin{bmatrix}\langle\nabla_y{}^T g_{(y)}^\mu k\nabla_z\phi^q\rangle\\ \langle\nabla_y{}^T g_{(z)}^\mu k\nabla_z\phi^q\rangle\end{bmatrix},\\
&2s^{pq} = \langle\nabla_y{}^T\phi^p k\phi^q\rangle - \langle\nabla^T\phi^q k\phi^p\rangle,\\
&\{k\}^{pq} = \langle\nabla_y{}^T\phi^p k\nabla\phi^q\rangle,
\end{aligned} \tag{23}$$

are used as additional denotations. Matrix coefficient $\mathbb{k}_{surf} = \mathbb{k}_{surf}(z)$ is referred to as Surface Localized part of Effective Conductivity Matrix. The homogenized part:

$$\begin{aligned}
&\lambda^2(\langle\phi^p c\phi^q\rangle\dot{a}_q - \nabla_z{}^T\langle\phi^p c\phi^q\rangle\nabla_z a_q) +\\
&+2\lambda s_{surf}{}^{pq}\nabla_z a_q + \{k\}_{surf}{}^{pq}a_p = 0
\end{aligned} \tag{24}$$

of $(22)_2$ describing uninhibited by external influences represented by the RHS part $L_a^\lambda[u]$ of (22) is usually considered as a model of the Boundary Effect Equation. The investigation of the reduction of Fourier amplitudes a_p from $(22)_2$ leads to the single equation for average temperature u referred to as the Effective Conductivity Equation. Imitating the appropriate procedure, the Effective Conductivity Equation without scale effect can be easily realized in the form:

$$\langle c\dot{u}\rangle - \nabla^T(\mathbb{k}_0[\nabla_z u] + \langle\phi^p\nabla_z{}^T(k\nabla_z u)\rangle) = -\langle b\rangle \tag{25}$$

from the asymptotic case of model equations:

$$\langle c\dot{u}\rangle - \nabla^T(\mathbb{k}_0{}^{eff}[\nabla_z u] + [k]_{surf}{}^p a_p) = -\langle b\rangle$$
$$\{k\}_{surf}{}^{pq} a_p = L_a^0[\nabla_z u] \tag{26}$$

for $\lambda \searrow 0$ and for $\mathbb{k}_0{}^{eff}$ given by:

$$\mathbb{k}_0{}^{eff}[\nabla_z u] = \mathbb{k}_{surf}[\nabla_z u] - [k]_{surf}{}^p \cdot$$
$$\cdot (\{k\}_{surf}{}^{-1})^{pq}\big(\langle \nabla_y{}^T \phi^q k\rangle \nabla_z u + \langle \phi^q \nabla_z{}^T (k\nabla_z u)\rangle\big) \tag{27}$$

As the benchmark problem, we are to propose a procedure of eliminating Fourier amplitudes from (22)2, which results the derivation of Effective Conductivity single equation for average temperature. The investigation will be restricted to the special case for $D = 2$ and $d = 1$.

4. PASSAGE TO THE EFFECTIVE CONDUCTIVITY

Let $\mathrm{D} = 2$, $\sigma = 1$. Hence, k is a symmetric 2×2 positive matrix and let $k = [k_{yy}, k_{yz}; k_{zy}, k_{zz}]$, $k_{yz} = k_{zy}$, and hence, we deal with two-dimensional periodic layer. Moreover, denote:

$$(L_a^\lambda[\tfrac{du}{dz}])^p \equiv \langle \tfrac{d\Phi^p}{dy} k_{yz} + \tfrac{d\Phi^p}{dz} k_{zz}\rangle \tfrac{du}{dz} - \lambda\langle \varphi^p b\rangle \tag{28}$$

We are to take a stationary case:

$$\tfrac{d}{dz}(\mathbb{k}_{surf}\tfrac{du}{dz} + [k]^p a_p) = \langle b\rangle$$
$$\langle \phi^p c \phi^q\rangle \tfrac{d^2 a_p}{dz^2} - 2\lambda s^{pq}\tfrac{da_q}{dz} - \{k\}^{pq} a_p = -L_a^\lambda[u] \tag{29}$$

of (22) being in this case the second order ordinary differential equations. Let $A_k{}^{pq} = \langle \phi^p c\phi^q\rangle$ be elements of quadratic matrix A. Moreover, let:

$$\Delta = s_{surf}{}^2 + A\{k\}_{surf},\ r_\pm = -A_k{}^{-1}(\sqrt{\Delta} \pm s_{surf}),$$
$$R \equiv r_+ - r_-, \tag{30}$$

where: square root is used here for positive quadratic matrix Δ and is equal to the unique positive matrix $\sqrt{\Delta}$ for which $\sqrt{\Delta}^2 = \Delta$ while $\frac{s_{surf}}{A_k} = s_{surf}\cdot A_k{}^{-1} = A_k{}^{-1}\cdot s_{surf}$ for any matrices alternating in multiplication. Similarly, $\frac{\sqrt{\Delta}}{A_k} = \sqrt{\Delta}\cdot A_k{}^{-1} = A_k{}^{-1}\cdot\sqrt{\Delta}$ for positive matrices Δ and R. Moreover, let

$$\ker_R(\omega) = R^{-1}\cdot \mathrm{sh}R\omega, \mathrm{coker}_R(\omega) = \mathrm{ch}R\omega \tag{31}$$

for $\omega \in \{(z-\delta)/\delta, z/\delta\}$, and consider $a \equiv [a_1, a_2, \ldots]^T = \sigma^h + \sigma^s$ as a solution to (29)2 (with respect to Fourier amplitudes a_p) satisfying $a(0) = a_0$ and $a(\frac{\delta}{\lambda}) = a_\delta$ as attached boundary conditions. Integral:

$$\tfrac{1}{2}\lambda A_k \sigma^s(z) = I_0 \equiv \int_0^z \ker(\tfrac{z-\xi}{\lambda}) L_a^\lambda[u](\xi)\, d\xi \tag{32}$$

is considered as a formula for an arbitrary but fixed solution σ^s of (29)2 and:

$$\sigma^h(\tfrac{z}{\lambda}) = \frac{\sinh R\frac{z}{\lambda}}{\sinh R\frac{\delta}{\lambda}}[a^\delta - \sigma^s(\tfrac{\delta}{\lambda})] - \frac{\sinh R\frac{z-\delta}{\lambda}}{\sinh R\frac{\delta}{\lambda}} a^0 \tag{33}$$

is a solution to homogeneous part:

$$\lambda^2\langle \phi^p c\phi^q\rangle \frac{d^2 a_p^h}{dz^2} - 2\lambda s^{pq}\frac{da_p^h}{dz} - \{k\}^{pq} a_p^h = 0 \tag{34}$$

of (29)2 satisfying $a_p^h(0) = a_0 - \sigma^s(0)$ and $a_p^h(\delta/\lambda) = a_\delta - \sigma^s(\delta/\lambda)$. Double integration:

$$I_0 = \int_0^z \ker(\tfrac{z-\xi}{\lambda}) L_a^\lambda[u](\xi)\, d\xi = \lambda R^{-1}\{L_a^\lambda[u](z) -$$
$$-\mathrm{coker}_R(\tfrac{z}{\lambda}) L_a^\lambda[u](0)\} - \lambda R^{-1}\cdot\{\ker_R(\xi)\frac{dL_a^\lambda[u](0)}{dz} +$$
$$+\int_0^z \ker_R(\tfrac{z-\xi}{\lambda})\frac{d^2L_a^\lambda[u](\xi)}{dz^2} d\xi\} \tag{35}$$

realized under denotations:

$$X_{2k}(z,\xi) \equiv \ker_R(\tfrac{z-\xi}{\lambda})\frac{d^{2k}L_a^\lambda[u]}{dz^{2k}}(\xi)$$
$$Y_{2k}(z,\xi) \equiv \mathrm{coker}_R(\tfrac{z-\xi}{\lambda})\frac{d^{2k}L_a^\lambda[u]}{dz^{2k}}(\xi) \tag{36}$$

results formula:

$$\sigma^s(z) = \frac{A_k}{2}\cdot\sum_{k=0}^n \lambda^{2k}(R^{-1})^{2k-1}\{Y_{2k}(z,z) - Y_{2k}(z,0) -$$
$$-(\lambda R^{-1})[-X_{2k+1}(z,z) + X_{2k+1}(z,0)]\} +$$
$$-(-\lambda)^{2n+1}\frac{A_k}{2}\cdot(R^{-1})^{2k}\int_0^z X_{2k+2}(z,\xi)d\xi \tag{37}$$

Let $[k]^T \equiv [[k]^1, [k]^2, \ldots]$. Coefficients:

$$\mathbb{k}_{2k}(z) \equiv [k]^T\tfrac{A_K}{2}\cdot(R^{-1})^{2k-1}[k] =$$
$$-[k]^T\tfrac{A_K}{2}\cdot(R^{-1})^{2k-1}[Y_{2p}(z,z) - \lambda R^{-1}X_{2p+1}(z,z)] =$$
$$= [k]^T\{-\tfrac{A_K}{2}\cdot(R^{-1})^{2p-1}\cdot\mathrm{coker}_R(\tfrac{z-\xi}{\lambda})\frac{d^{2k}L_a^\lambda[u]}{dz^{2k}}(\xi) +$$
$$+\lambda R^{-1}\cdot\ker_R(\tfrac{z-\xi}{\lambda})\frac{d^{2k}L_a^\lambda[u]}{dz^{2k}}(\xi)\}|_{\xi=z}$$
$$\langle b\rangle_{2k}(z) \equiv -[k]^T\tfrac{A_K}{2}\cdot(R^{-1})^{2k-1}[Y_{2k}(z,0) -$$
$$-\lambda R^{-1}X_{2k+1}(z,0)] =$$
$$= [k]^T\{-\tfrac{A_K}{2}\cdot(R^{-1})^{2k-1}\cdot\mathrm{coker}_R(\tfrac{z-\xi}{\lambda})\frac{d^{2k}L_a^\lambda[u]}{dz^{2k}}(\xi) +$$
$$+\lambda R^{-1}\cdot\ker_R(\tfrac{z-\xi}{\lambda})\frac{d^{2k}L_a^\lambda[u]}{dz^{2k}}(\xi)\}|_{\xi=0} \tag{38}$$

are amplitudes of corrections:

$$\mathbb{k}^s(z) = \textstyle\sum_{k=1}^{+\infty}(-1)^{k-1}\lambda^{2k}\mathbb{k}_{2k}(z)$$
$$\langle b\rangle^s(z) \equiv \textstyle\sum_{k=1}^{+\infty}(-1)^{k-1}\lambda^{2k}\langle b\rangle_{2k}(z) \tag{39}$$

imposed on Effective Conductivity $\mathbb{k}^{eff}(z)$ and the average sources $\langle \mathrm{b}\rangle$ in formulas $\mathbb{k}_\lambda^{\mathrm{eff}}(z) \equiv \mathbb{k}^{\mathrm{eff}}(z) + \mathbb{k}^s(z)$ as well as $\langle b\rangle_\lambda^{eff} \equiv \langle b\rangle + \mathbb{k}^s(0) - \sigma^{hom}(z)$ for Effective Conductivity and Effective Sources, respectively, depends of λ. Formula:

$$res_{2n+1}[u](z) =$$
$$(-1)^{n+1}\lambda^{2n+1}\tfrac{A_k}{2}\cdot(R^{-1})^{2n}\int_0^z X_{2n+2}(z,\xi)d\xi \tag{40}$$

represents error made while $\mathbb{k}^s(z)$, $\mathbb{k}^s(0)$ are replaced by:

$$\mathbb{k}_{(2N)}{}^s(z) = \textstyle\sum_{n=1}^{2N}(-1)^{n-1}\lambda^{2k}\mathbb{k}_{2k}(z)$$
$$\langle b\rangle_{(2N)}{}^s(z) \equiv \textstyle\sum_{n=1}^{2N}(-1)^{n-1}\lambda^{2k}\langle b\rangle_{2k}(z) \tag{41}$$

of (39). Modulus of (39) can be formally estimated by the supremum of modulus of the RHS side of (40) proportional to λ^{2n+1}. That is why, $\lambda < 1$ is a sufficient condition for convergence of RHS of (40) to zero, while $n \to \infty$. Finally, we obtain:

$$\frac{d}{dz}(\mathbb{k}_\lambda^{eff}(z)\frac{du}{dz}) = \langle b\rangle_\lambda^{eff} \tag{42}$$

instead of (29).

DOI 10.2478/ama-2019-0017

5. FURTHER APPROXIMATIONS OF THE EFFECTIVE CONDUCTIVITY EQUATION

Effective Conductivity problem will be examined as a boundary value problem for $2N$-th order ordinary differential equation:

$$\frac{d}{dz}\{\mathbb{k}^{eff}(z)\frac{du}{dz}+\sum_{n=1}^{N}(-1)^{n+1}\lambda^{2n}\mathbb{k}_{2n}(z)\frac{d^{2n-1}u}{dz^{2n-1}}\} = \\ =\langle b\rangle^{eff}+\sum_{n=0}^{+\infty}(-1)^{n+1}\lambda^{2n}\langle b\rangle_{2n}(z) \tag{43}$$

in which:

$$\mathbb{k}_{(2N)}{}^{s}(z)=\sum_{n=1}^{2N}(-1)^{n-1}\lambda^{2n}\mathbb{k}_{2n}(z)\frac{d^{2n}u}{dz^{2n}} \tag{44}$$

The following uniqueness conditions:

$$\frac{d^{n-1}u}{dz^{n-1}}(0)=u_0^{n-1}, n=1,\dots,N, \tag{45}$$

will be attached. Formulated Cauchy problem is considered as $2N$th order approximation of Effective Conductivity problem.

Asymptotic approximation is considered as $N=0$. Now, mentioned Cauchy problem simplifies to:

$$\begin{cases}\frac{du}{dz}\{\mathbb{k}^{eff}(z)\frac{du}{dz}\}=\langle b\rangle^{eff}\\ u(0)=u_0,\quad u(\delta)=u_\delta\end{cases} \tag{46}$$

leads to the solution:

$$u=u_0+\int_0^z\frac{\mathrm{Q}(\xi)}{\mathbb{k}^{eff}(\xi)}d\xi, \mathrm{Q}=\mathrm{Q}_0+\int_0^z\langle b\rangle^{eff}(\xi)d\xi \tag{47}$$

for the average heat flux Q. For homogeneous periodicity, (47) reduces to the form:

$$u(z)=u_0+\frac{1}{\mathbb{k}^{eff}}(\mathrm{Q}_0+z\langle b\rangle^{eff}), \\ \mathrm{Q}_0=\mathbb{k}^{eff}(u_\delta-u_0)-\delta\langle b\rangle^{eff} \tag{48}$$

Approximate solutions to the considered Cauchy problem can be interpreted as subsequent overlaps on the unscaled average temperature approximation (48) valid for $N=0$. Denote:

$$f(z)\equiv\delta(0)+\int_{\varsigma=0}^{\varsigma=z}d\varsigma\frac{1}{\mathbb{k}^{eff}(\varsigma)}[\beta_0+\int_{\xi=0}^{\xi=\varsigma}\langle b\rangle_\lambda{}^{eff}(\xi)d\xi] \tag{49}$$

For:

$$\beta_0\equiv\mathbb{k}^{eff}(0)\frac{du(0)}{dz}+\sum_{n=0}^{N}(-1)^n\lambda^{2n+2}\mathbb{k}_{2n}(0)\frac{d^{2n+1}u(0)}{dz^{2n+1}}, \\ \delta_0\equiv u(0)+\sum_{n=0}^{N}(-1)^n\lambda^{2n+2}\frac{\mathbb{k}_{2n+2}(0)}{\mathbb{k}^{eff}(0)}\frac{d^{2n}u(0)}{dz^{2n}} \tag{50}$$

Double integration of (43) leads from (43) to the $2N$th order ordinary differential equation:

$$-u+\sum_{n=1}^{N}(-1)^n\lambda^{2n}\frac{\mathbb{k}_{2n+2}(z)}{\mathbb{k}^{eff}(z)}\frac{d^{2n}u}{dz^{2n}}=f(z) \tag{51}$$

with:

$$-1+\sum_{n=1}^{N}(-1)^n\lambda^{2n}\frac{\mathbb{k}_{2n+2}(z)}{\mathbb{k}^{eff}(z)}r^{2n}=f(z) \tag{52}$$

as a characteristic equation.

4th order approximation will be considered as $N=2$. In this case and for homogeneous periodicity related approximate solution to the Effective Conductivity Problem can be written as:

$$\begin{aligned}u(z)=&-\frac{k_{eff}}{\lambda^4k_6}[u(0)zf_s^+(z)*f_s^-(z)+\\&+u'(0)z^2f_s^+(z)*f_s^-(z)]+\\&-\frac{k_4}{\lambda^2k_6}[u(0)(f_c^+(z)*f_s^-(z)+\kappa f_s^+(z)*f_s^-(z))+\\&+u'(0)f_s^+(z)*f_s^-(z)+\\&+u^{(2)}(0)zf_s^+(z)*f_s^-(z)+u^{(3)}(0)z^2f_s^+(z)*f_s^-(z)]-\\&-[(A_{ch}(f_c^+(z)+f_c^-(z))+\\&+B_{sh}(f_s^+(z)-f_s^-(z)))u(0)+\\&+u^{(1)}(0)(f_c^+(z)*f_c^-(z)+\kappa^2f_s^+(z)*f_s^-(z))\\&+u^{(2)}(0)(f_c^+(z)*f_s^-(z)-\kappa f_s^+(z)*f_s^-(z))+\\&+u^{(3)}(0)f_s^+(z)*f_s^-(z)+\\&+u^{(4)}(0)zf_s^+(z)*f_s^-(z)+u^{(5)}(0)z^2f_s^+(z)*f_s^-(z)]-\\&-\frac{\langle b\rangle(z)}{\lambda^4k_6}f_s^+(z)*f_s^-(z)\end{aligned} \tag{53}$$

in which the convolution integral $f_1(z)*f_2(z)$ is used for:

$$f_c^+(z)=e^{\kappa\frac{z-\delta}{\lambda}}\cos\omega\frac{z}{\lambda}, f_s^+(z)=e^{\kappa\frac{z-\delta}{\lambda}}\sin\omega\frac{z}{\lambda}, \\ f_c^-(z)=e^{-\kappa\frac{z-\delta}{\lambda}}\cos\omega\frac{z}{\lambda}, f_s^-(z)=e^{-\kappa\frac{z-\delta}{\lambda}}\sin\omega\frac{z}{\lambda}. \tag{54}$$

and for not vanishing roots $\pm\kappa\pm\mathrm{i}\,\omega$, $i^2=-1$, $\kappa,\omega>0$, of algebraic equation (52) for $N=2$. Constant coefficients A_{ch} and B_{sh} in (53) should satisfy:

$$\begin{bmatrix}\frac{\omega+2\kappa}{(\omega+2\kappa)^2+\omega^2}+\frac{1}{2\omega} & \frac{1}{(\omega+2\kappa)^2+\omega^2}-\frac{1}{2\omega^2}\\ \frac{1}{2\omega}+\frac{\omega+2\kappa}{(\omega-2\kappa)^2+\omega^2} & \frac{1}{2\omega^2}-\frac{1}{(\omega-2\kappa)^2+\omega^2}\end{bmatrix}\cdot \\ \cdot\begin{bmatrix}A_{ch}\\ B_{sh}\end{bmatrix}=\begin{bmatrix}\frac{\omega+2\kappa}{(\omega+2\kappa)^2+\omega^2}+\frac{1}{2\omega}\\ \frac{1}{2\omega}+\frac{\omega+2\kappa}{(\omega-2\kappa)^2+\omega^2}\end{bmatrix} \tag{55}$$

Hence, (53) are the basic formulas constituting the departure point for the prediction of the control form of the average temperature of the microstructural parameter. We intend to formulate an appropriate hypothesis for the case determined by $D=2$ and $d=1$ considered in this section.

6. FINAL HYPOTHESIS

In order to arrive at the main thesis of the paper, we will now generalize the results of the last section, resulting in the predicted distribution of the average temperature as a solution to the Effective Heat Conductivity problem controlled by the microstructural parameter λ. We formulate the following hypothesis:

Final Hypothesis. The sequence of subsequent solutions of $2N$th approximations of the Effective Conductivity problem can be written as a sum of terms of the form (54), where κ and ω run over all pairs corresponding to the collection of not vanishing roots $\pm\kappa\pm\omega\mathrm{i}$ of characteristic equation (52). Coefficients of this sum are uniquely determined by the initial values $u^{(n)}(0)$, $n=0,1,2,3,\dots$.

However, limit formulas of this approximated solutions to the Effective Conductivity equation, developed while $\lambda\to0$, exist in a weak sense. It is also worth emphasizing that the interpretation of the first component of the Fourier expansion (19) as the average temperature is obtained as the integration effect of the infinite function series and thus uses as the assumption that the various limit operations which are applied are alternating.

REFERENCES

1. **Ariault J.L.** (1983), Effective macroscopic description for heat conduction in periodic composites, *International Journal of Heat and Mass Transfer*, 26(6), 861–869.
2. **Bensoussan A., Lions J.-L., Papanicolaou G.** (2011), Asymptotic Analysis for Periodic Structures, American Math. Soc., ISBN-10: 0-8218-5324-4 ISBN-13: 978-0-8218-5324-5.3
3. **Jędrysiak J.** (2010), *Thermomechanics of laminates, plates and shells with functionally graded properties* (in Polish), Technical University of Łódź Press.
4. **Kula D.** (2015), On the existence of the sinusoidal–type temperature fluctuations independently suppressed by the periodic two – phased conducting layer, *Acta Scientarum Polonorum, Ser, Arch.*, 63(1), 77–92.
5. **Kula D., Wierzbicki E.** (2015), On the Fourier series implementation issue tolerance modelling thermal conductivity of periodic composites, *Engineering Transaction*, 63(1), 77–92.
6. **Michalak B.** (2010), *Thermomechanics of solids with a certain nonhomogeneous microstructure: tolerance approximation technique* (in Polish), Technical University of Łódź Press.
7. **Ostrowski P.: (2017),** *Tolerance modelling of Thermomechanics in microstructured media*, Technical University of Łódź Press.
8. **Wodzyński Ł., Kula D., Wierzbicki E.** (2018). Effective macroscopic description for heat conduction in periodic composites, *Proceedings of the 22nd International Conference on Computer Methods in Mechanics*: Lublin, Poland, 13–16 September 2017, eds. Jerzy Podgórski, Ewa Blazik Borowa, Jarosław Bęc, Tadeusz Burczyński, Mieczysław Kuczma, Jarosław Latalski, Jerzy Warmiński. - AIP Publishing, 1–8.
9. **Woźniak Cz., Wierzbicki E.:** (2000), *Averaging techniques In thermomechanics of composite solids, Tolerance averaging versus homogenization*, Technical University of Częstochowa Press.
10. **Woźniak M., Wierzbicki E., Woźniak Cz.** (2002), A macroscopic model of the diffusion and heat transfer processes in a periodically micro-stratified solid layer, *Acta Mechanica*, 157, 175–185.

DOI 10.2478/ama-2019-0018

ROBOTIC SWARM SELF-ORGANISATION CONTROL

Zenon HENDZEL[*], Jakub WIECH[*]

[*]Faculty of Mechanical Engineering and Aeronautics, Department of Applied Mechanics and Robotics, Rzeszow University of Technology, al. Powstańców Warszawy 12, 35-959 Rzeszów, Poland

zenhen@prz.edu.pl, j.wiech@prz.edu.pl

received 26 June 2018, revised 25 June 2019, accepted 28 June 2019

Abstract: This article proposes a new swarm control method using distributed proportional-derivative (PD) control for self-organisation of swarm of nonholonomic robots. Kinematics control with distributed proportional-derivative (DPD) controller enables generation of desired robot trajectory achieving collective behaviour of a robotic swarm such as aggregation and pattern formation. Proposed method is a generalisation of virtual spring-damper control used in swarm self-organisation. The article includes the control algorithm synthesis using the Lyapunov control theory and numeric simulations results.

Keywords: swarm robotics self-organization, PD controller, nonholonomic robots

1. INTRODUCTION

The problem of swarm self-organisation is one of the several elementary collective behaviours observed in nature. The examples of swarming behaviours are line formations in ant colonies, bird flocks, fish schools and so on. These basic formations enable animals to enhance foraging success or give better protection from predators. In case of robotic swarms, formation control enables achieving collective goals in orderly manner, very often more efficiently than without behaviours of this type. Area coverage, oil plume removal, swarm transport and object manipulation are some of the examples in which swarm formation control is widely used (Brambilla et al., 2013).

The self-organisation process allows for pattern creation from randomly distributed robots. The robots can establish formation using only local information about their neighbouring robots or using a global reference if it is required by the control algorithm. By self-organisation, we mean the emergence of order in a robotic swarm as the result of local interactions amongst robots constituting the swarm. Existing methods of swarm formation control are either bio-inspired, based on physics phenomena, or derived from control theory. Bio-mimicking methods were the first to emerge, for example, Reynolds study of flocks, herds and schools (Reynolds, 1987) or starlings flocking analysis by Hildenbrandt et al. (2010). Rauch et al. (1995) studied class of models for pattern formation based on the behaviours of social insects. Similar works are presented in Christensen et al.(2009), Hsieh(2008) and Trianni (2008). Physics-inspired methods are also popular, thanks to the well-described mathematical equations that are the basis for developing a control algorithm. For example, by imagining the robots being connected to each other by virtual spring and damper, forcing them to move, the swarm will eventually aggregate to one point or, with careful adjustment of virtual parameters, the swarm will establish a formation (Balkacem and Foudil, 2016; Urcola et al., 2008; Shucker and Bennett, 2005; Spears et al., 2004; Wiech et al., 2018). Another approach is to develop the control algorithm using stability and optimisation theory (Cheah et al., 2009). The works of Gazi and Passino (2003, 2004) and Gazi (2005) based on artificial potential functions allow for formation control, foraging, swarm tracking and so on. In the following work, a swarm self-organisation control algorithm was formulated, inspired by virtual spring damper method with stability proof using the Lyapunov techniques.

2. DESIRED ROBOT TRAJECTORY GENERATION

The kinematics control with distributed proportional-derivative (DPD) controller will be used for desired trajectory generation for each member of a swarm. In case of mentioned physics-based method (Fig. 1), the robots were connected by virtual spring dampers, which resulted in formation creation. The net virtual force exerted on a robot lead the robot to a point in space R_z, which can be described as a local stability point. The position of R_z is a function of time, and it is related to springs deformations between the robot and its neighbours. As generalisation of said method, we present an approach different from the virtual spring dampers.

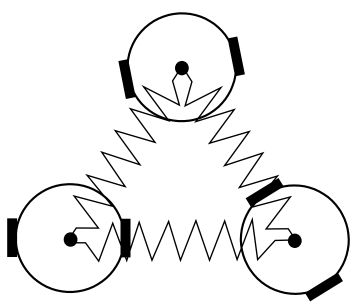

Fig. 1. Virtual physics based method

2.1. Geometric relations

The robot R and its neighbouring robots $R_{s1}, R_{s2}, \dots, R_{si}$ are minimising the distance differences $e_1, e_2, \dots, e_i$ between current distances between robots $l_1, l_2, \dots, l_i$ and the desired distance δ. For this purpose, the differences $e_1, e_2, \dots, e_i$ were substituted with the distance error e_δ pictured in Figure 2.

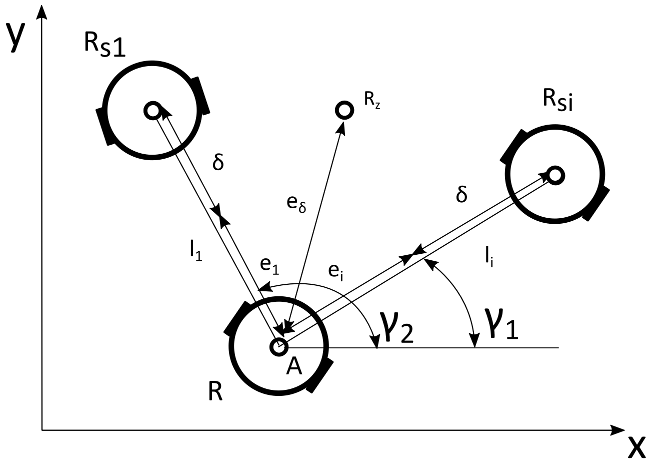

Fig. 2. Distances in the swarm

The value of the distance error e_δ is defined as follows:

$$e_\delta = \sqrt{\sum_{i=1}^{n} {e_{yi}}^2 + \sum_{i=1}^{n} {e_{xi}}^2}, \tag{1}$$

where $e_{xi} = e_i \cos\gamma_i$ and $e_{yi} = e_i \sin\gamma_i$

The distance difference e_i is described using equations:

$$e_i = l_i - \delta, \tag{2}$$

$$e_i = \sqrt{{e_{yi}}^2 + {e_{xi}}^2}. \tag{3}$$

All robots are equipped with distance sensors with limited range. Sensor range determines how many robots are detected. In order to detect only the nearest neighbours, the sensing range, SR, has to meet the inequality:

$$\delta\sqrt{3} > SR > \delta. \tag{4}$$

If we set the range SR = 1.2δ, the swarm will form the equilateral triangle formation. Geometric interpretation of SR value is depicted in Figure 3.

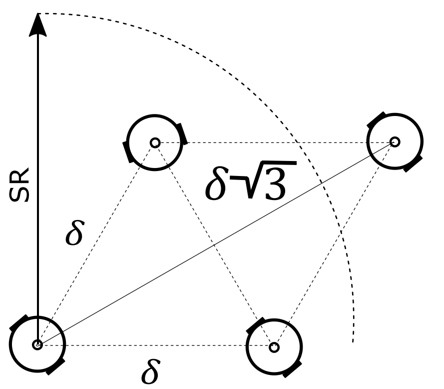

Fig. 3. Robot sensor range for sensing only nearest neighbours

2.2. Stability analysis of the algorithm generating the desired trajectory

Each member of the swarm calculates the distance error e_δ and an angle ψ between robot heading and e_δ based on the position of its neighbouring robots (Fig. 4). In the following equations, the index *i* was omitted.

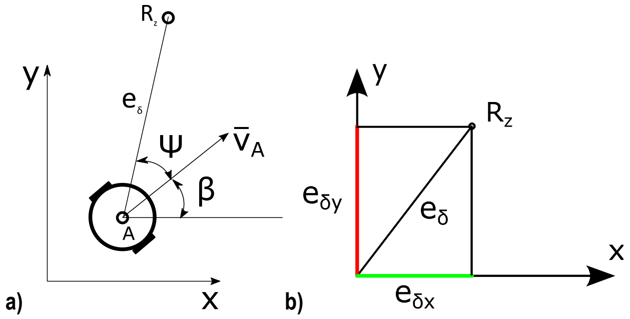

Fig. 4.(a) Robot R in relation to point R_z and (b) projections of e_δ

The value of e_δ is defined using equation (1), whereas ψ is calculated using the following formula:

$$\psi = arctg\left(\frac{e_{\delta y}}{e_{\delta x}}\right) - \beta, \tag{5}$$

where $e_{\delta x}$ and $e_{\delta y}$ are the projections of e_δ on the axes x and y (Fig. 4b).

The kinematics equations of the mobile robot in relation to the goal position R_z in polar coordinate system are

$$\begin{aligned} \dot{e}_\delta &= -v_A \cos\psi, \\ \dot{\psi} &= v_A \frac{\sin\psi}{e_\delta} - \dot{\beta}. \end{aligned} \tag{6}$$

Error vector $\boldsymbol{q_p}$ in polar coordinates is defined as

$$\boldsymbol{q_p} = [e_\delta, \psi]. \tag{7}$$

Differentiating the error vector yields the following equations:

$$\begin{aligned} \dot{e}_\delta &= -u_v \cos\psi, \\ \dot{\psi} &= u_v \frac{\sin\psi}{e_\delta} - u_\beta, \end{aligned} \tag{8}$$

where u_v and u_β are the generated velocities v_A and $\dot{\beta}$, respectively.

To determine the control law $\boldsymbol{u_B} = [u_v, u_\beta]^T$ allowing the calculation of robot motion parameters v_A and $\dot{\beta}$, the Lyapunov stability theory was used. We consider the following positive definite function:

$$V = V_1 + V_2 = \tfrac{1}{2}{e_\delta}^2 + \tfrac{1}{2}\psi^2. \tag{9}$$

By differentiating the function V, we obtain

$$\dot{V}_1 = e_\delta \dot{e}_\delta = -e_\delta u_v \cos\psi, \tag{10}$$

$$\dot{V}_2 = \psi\dot{\psi} = \psi\left(\frac{u_v \sin\psi}{e_\delta} - u_\beta\right). \tag{11}$$

Using the DPD controller in the form

$$u_{DPD} = k_{DP} e_\delta + k_{DD} \dot{e}_\delta, \tag{12}$$

where k_{DP} and k_{DD} are the proportional and derivative distributed controller gain coefficients, respectively.

DOI 10.2478/ama-2019-0018

The linear velocity control u_v is defined as

$$u_v = u_{DPD} \cos\psi. \tag{13}$$

From equations (8), (12) and (13), we have

$$u_v = \frac{k_{DP} e_\delta \cos\psi}{1 + k_{DD} \cos^2\psi}. \tag{14}$$

Whilst the angular velocity control u_β is calculated from the equation

$$u_\beta = u_{DPD} \frac{\cos\psi \sin\psi}{e_\delta} + \lambda\psi, \tag{15}$$

where λ is the angular proportional gain coefficient.

With equations (8), (12) and (15), u_β is described as

$$u_\beta = \frac{k_{DP} \cos\psi \sin\psi}{1 + k_{DD} \cos^2\psi} + \lambda\psi. \tag{16}$$

Using equations (10),(11), (15) and (16), we can determine the sign of $\dot{V}$:

$$\dot{V}_1 = -e_\delta u_v \cos\psi = -\frac{kD_P {e_\delta}^2 \cos^2\psi}{1 + k_{DD} \cos^2\psi}, \tag{17}$$

$$\dot{V}_2 = \psi\left(\frac{u_v \sin\psi}{e_\delta} - u_\beta\right) = \psi\left(\frac{k_{DP} \cos\psi \sin\psi}{1 + kD_D \cos^2\psi} - \frac{k_{DP} \cos\psi \sin\psi}{1 + k_{DD} \cos^2\psi} - \lambda\psi\right) = -\lambda\psi^2, \tag{18}$$

$$\dot{V} = \dot{V}_1 + \dot{V}_2 = -\frac{k_{DP} {e_\delta}^2 \cos^2\psi}{1 + k_{DD} \cos^2\psi} - \lambda\psi^2 < 0 \ \forall\, k_{DD} > 0, k_{DP} > 0, \lambda > 0. \tag{19}$$

Thus the derivative of the proposed function (9) satisfies the inequality $\dot{V} < 0$, which means that the function V is the Lyapunov function, and we can conclude the asymptotic stability of the equilibrium point $q_p = [0,0]$.

2.3. Robot control algotrithm

We consider a swarm of N two-wheel mobile robots (Fig.4a) whose dynamics of the *i*th robot can be described as (Giergiel and Żylski, 2005)

$$M\ddot{q} + C(\dot{q})\dot{q} + F(\dot{q}) = \tau, \tag{20}$$

where $q = [\alpha_1, \alpha_2]^T$ is the vector of generalised coordinates (rotation angles of both wheels), M is the inertia matrix, $C(\dot{q})\dot{q}$ is the vector of Coriolis and centripetal forces, $F(\dot{q})$ is the wheels friction vector, $\tau = [\tau_1, \tau_2]^T$ denotes the control inputs and τ_1, τ_2 are driving torques.

The desired angular kinematic parameters $\dot{q}_d$= $[\dot{\alpha}_{1d}, \dot{\alpha}_{2d}]^T$of a robot are calculated from the following equations (Giergiel and Żylski, 2005):

$$\dot{\alpha}_{1d} = \frac{u_v}{r} + u_\beta \frac{l}{r}, \dot{\alpha}_{2d} = \frac{u_v}{r} - u_\beta \frac{l}{r}, \tag{21}$$

where $\dot{\alpha}_{1d}$ and $\dot{\alpha}_{2d}$ are the desired wheels angular velocities, respectively; r is the wheel radius; l is the half of the length of the drive axle (Fig. 5); u_v is the linear velocity of the point A; and u_β is the angular velocity of the robot frame.

Desired trajectory generation schematics is shown in Figure 6.

For tracking the desired trajectory generated by the DPD controller by a point A_i of the *i*th robot, the following proportional-derivative (PD) controller is used [9,12]:

$$u = k_P e_t + k_D \dot{e}_t, \tag{22}$$

where k_P is the proportional tracking controller gain, k_D is the derivative tracking controller gain, $e_t = q_d - q$ is the trajectory tracking error and $\dot{e}_t = -\dot{q}$ is the derivative of the trajectory tracking error.

Control schematics of trajectory tracking is shown in Figure 7.

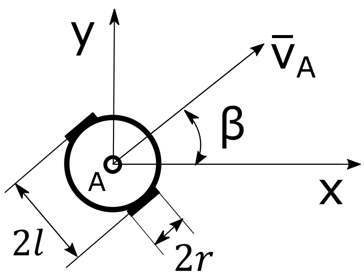

Fig. 5. Scheme of a two-wheeled robot

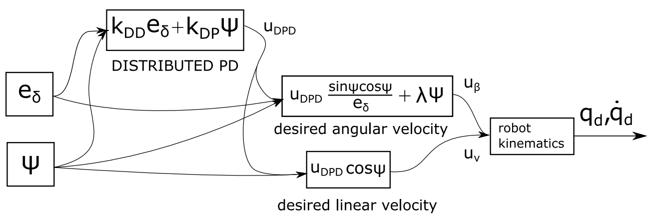

Fig. 6. Scheme of desired trajectory generation

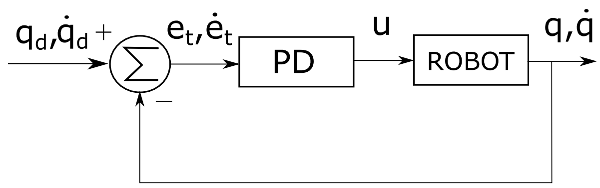

Fig. 7. Scheme of desired trajectory tracking

2.4. Stability analysis of robot trajectory tracking algorithm

To prove the stability of trajectory tracking, the introduction of-servomotor equation is necessary. The servomotor dynamics is described by the equation (Spong and Vidyasagar, 1989)

$$J_k \ddot{\Theta}_k + (B_k + K_D K_M / R)\dot{\Theta}_k = K_M / R V_k - r_k \tau_k, \tag{23}$$

where *k* = 1,2, J_k is the sum of the actuator and gear inertias, Θ_k is the rotor position [rad], B_k is the viscous friction coefficient, K_D is the back emf constant, K_M is the torque constant, R is the armature resistance, V_k is the armature voltage and r_k is the gear ratio.

Using the relation between the rotor position and wheel position $\Theta_k = \alpha_k / r_k$, the equation (23) will become

$$\frac{1}{{r_k}^2} J_k \ddot{\alpha}_k + \frac{1}{{r_k}^2}(B_k + K_D K_M / R)\dot{\alpha}_k = \frac{K_M}{r_k R} V_k - \tau_k. \tag{24}$$

Substituting $B_k + \frac{K_D K_M}{R} = B$ and $\frac{1}{{r_k}^2} J_k = J$, we have

$$J\ddot{\alpha}_k + B\dot{\alpha}_k = \frac{K_M}{r_k R} V_k - \tau_k. \tag{25}$$

Combining equations (23) and (20), the robot dynamics with servomotor dynamics in matrix notation will be of the form

$$[M+J]\ddot{q}+[C(\dot{q})+B]\dot{q}+F(\dot{q})=u, \tag{26}$$

where $u=[u_1,u_2]^T$ and $u_k=\frac{K_M}{r_kR}V_k$ for k=1,2,.

For control signal u, we propose PD controller described by equation (22) that can be rewritten as

$$u=k_Pe_t-k_D\dot{q}. \tag{27}$$

We consider the following positive definite function:

$$V=\frac{1}{2}\dot{q}^T[M+J]\dot{q}+\frac{1}{2}e_t{}^Tk_Pe_t. \tag{28}$$

The derivative of function V is

$$\dot{V}=\dot{q}^T[M+J]\ddot{q}-\dot{q}^Tk_Pe_t. \tag{29}$$

From equations (26) and (29), we have

$$\dot{V}=\dot{q}^T[u-B\dot{q}-F(\dot{q})-k_Pe_t]\ddot{q}-\dot{q}^TC(\dot{q})\dot{q}. \tag{30}$$

From robot dynamics, we know that the matrix $C(\dot{q})$ is a skew symmetric. Substituting equation (27) into equation (30), we will have

$$\dot{V}=-\dot{q}^T[k_D+B+F(\dot{q})]\dot{q}. \tag{31}$$

To prove stability, we use LaSalle's theorem [18]. Suppose $\dot{V}\equiv 0$. Then equation (31) implies that $\dot{q}\equiv 0$ and, hence, $\ddot{q}\equiv 0$. From equations (26) and (27), we have

$$[M+J]\ddot{q}+[C(\dot{q})+B]\dot{q}+F(\dot{q})=k_Pe_t-k_D\dot{q}. \tag{32}$$

Substituting $\dot{q}\equiv 0$ and $\ddot{q}\equiv 0$ and knowing that $F(0)=0$, we obtain

$$0=-k_Pe_t, \tag{33}$$

which implies that $e_t=0$. LaSalle's theorem then implies that the equilibrium is asymptotically stable.

3. SIMULATIONS

As per the performance evaluation, two simulations were performed with swarm having 21 constituting robots. The robots were initially randomly distributed with random headings (triangles in swarm centre). The final positions and heading of robots are depicted by equally distributed triangles with δ = 1.5m. The control algorithm parameters were set experimentally as follows: k_{DP} = 2.4, k_{DD} = 1.3, λ = 10, $k_P=\begin{bmatrix}3 & 0\\0 & 3\end{bmatrix}$, $k_D=\begin{bmatrix}0.2 & 0\\0 & 0.2\end{bmatrix}$.

3.1. Swarm formation

The desired distance δ between robots was set to 1.5m, which leads to dispersion of robots and establishing a formation. The formation is shown in Figure 8; the change in velocity and the distance of robot no. 5 is depicted in Figure 9.

The simulation shows that the swarm self-organise into formation consisting mostly of equilateral triangles of length equal 1.5m. In Figure 8, we can see that some of the distances between robots on the outer edge of the formation are smaller than 1.5m, which could be avoided by setting different values for k_{DP} and k_{DD}.

The maximum velocity v_A the robot can reach is 0.3 m/s. The velocity change at the robot acceleration faze was approximated by a smooth ramp seen in Figure 9a. The distance difference e_δ reaches 0 after 12s, whereas heading difference ψ reaches 0 in finite time.

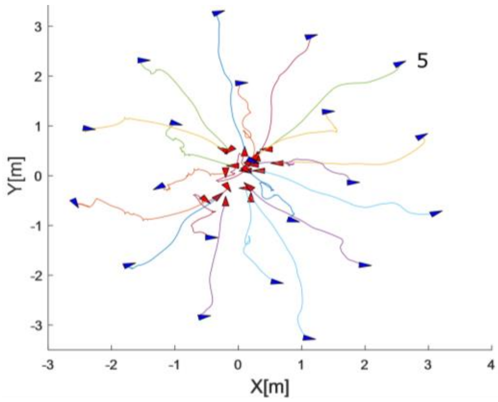

Fig. 8. Self-organisation of 21 robot swarm: trajectories and final formation: robots initial positions depicted in red and final positions in blue

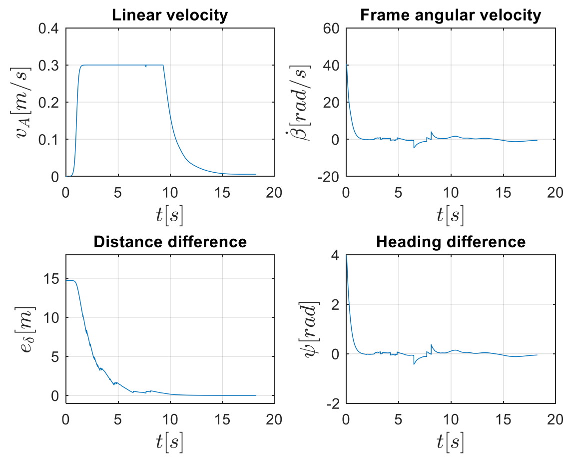

Fig. 9. Simulation results for robot no. 5: (a) linear velocity v_A, (b) frame angular velocity $\dot{\beta}$, (c) distance difference e_δ and (d) heading difference ψ

3.2. Swarm aggregation

Swarm aggregation can be achieved by setting the desired distance δ to 0. All robots would converge to single point. Real robots are constrained by their size; to avoid collisions, the desired distance δ was set to 0.15m, which is equal to the robot diameter (Fig. 10). The velocities and distance differences are shown in Figure 11.

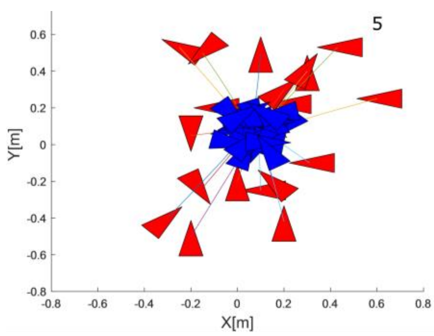

Fig. 10. Swarm aggregation: robots initial positions depicted in red and the final positions in blue

DOI 10.2478/ama-2019-0018

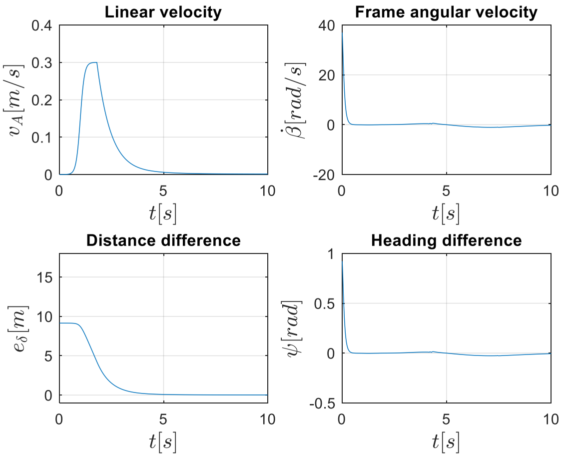

Fig. 11. Simulation results for robot no. 5 in swarm aggregation process: (a) linear velocity v_A, (b) frame angular velocity $\dot{\beta}$, (c) distance difference e_δ and (d) heading difference ψ

4. SUMMARY

In this article, the method of self-organisation of nonholonomic robotic swarm using DPD controller was presented. Numerical simulations show that using this method, a robotic swarm is able to achieve equilateral triangle formation as well as reach the desired neighbourhood of the aggregation point.

Owing to high amplitudes of robots acceleration, it was necessary to introduce a smooth velocity ramp and a proximity zone in which the robot will stop, if it is reached. The proximity zone is a zone of small radius from the equilibrium point, introduced because of the requirement $e_\delta \neq 0$ from equation (6).

The shape of the formation depends on the correctly set DPD parameters as well as the parameters of PD controller used for trajectory tracking. The lower the tracking error is, the faster and more accurate is the swarm self-organisation. It could be beneficial to substitute the PD controller with more precise control method such as adaptive neural control or neural dynamic programming.

It is of interest in future works to address the problem of generating the optimal desired robot trajectories and finding the optimal values of control parameters. Moreover, future works will address swarm leader following and obstacle avoidance.

REFERENCES

1. **Balkacem K., Foudil, C.** (2016), *A virtual viscoelastic based aggregation model for self-organization of swarm robots system*, TAROS 2016: Towards Autonomous Robotic Systems, 202–213, .
2. **Brambilla M. Ferrante E., Birattari M., Dorigo M**. (2013), Swarm robotics: a review from the swarm engineering perspective, *Swarm Intel*l., 7(1), 1-41.
3. **Cheah C.C., Hou S.P., Slotine J.J.** (2009), Region-based shape control for a swarm of robots, *Automatica*, 45(10), 2406-2411.
4. **Christensen A.L., O'Grady R., Dorigo M.** (2009), From fireflies to fault-tolerant swarms of robots, *IEEE Transactions on Evolutionary Computation*, 13(4), 754-766.
5. **Gazi V.** (2005), Swarm aggregations using artificial potentials and sliding-mode control, *IEEE Transactions on Robotics*, 21(6), 1208-1214.
6. **Gazi V., Passino K.M.** (2003), Stability analysis of swarms, *IEEE Transactions on Automatic Control*, 48(4), 692-697.
7. **Gazi V., Passino K.M.** (2004), A class of attractions/repulsion functions for stable swarm aggregations, *International Journal of Control*, 77(18), 1567-1579.
8. **Giergiel J., Żylski, W.** (2005), Description of motion of a mobile robot by Maggie's equations, *J. Theor. Appl. Mech.*, 43(3), 511-521.
9. **Hendzel Z.** (2007), An adaptive critic neural Network for motion control of Wheeler mobile robot, *Nonlinear Dynamics*, 50, 849-855.
10. **Hildenbrandt H., Carere C., Hemelrijk C.K.** (2010) Self-organized aerial displays of thousands of starlings: a model,*Behavioral Ecology*, 21(6), 1349-1359,.
11. **Hsieh M.A., Halasz A., Bergman S., Kumar V.** (2008), Biologically inspired redistribution of a swarm of robots among multiple sites, *Swarm Intelligence*, 2(2-4), 121-141.
12. **Lewis F.L., Jagannathan S., Yesildirek A.** (1999), *Control of Robot Manipulators and Nonlinear Systems*, Tylor & Frnacjis, London.
13. **Rauch E., Millonas M.M., Chialvo D.R.** (1995), Pattern formation and functionality in swarm models**,** *Physics Letters A*, 207(3-4), 185-193.
14. **Reynolds C.W.** (1987) Flocks, herds and schools: A distributed behavioral model, *ACM SIGGRAPH Computer Graphics*, 21(4), 25-34, New York.
15. **Shucker B., Bennett J.K.** (2005),*Virtual spring mesh algorithms for control of distributed robotic macrosensors*, University of Colorado at Bulder, Technical Report CU-CS-996-05.
16. **Spears W.M., Spears D.F., Hamann J.C., Heil R.** (2004), Distributed, physics-based control of swarms of vehicles, *Autonomous Robots*, 17(2-3), 137-162.
17. **Spong M.W., Vidyasagar M.** (1989), *Robot dynamics and control*, John Wiley & Sons.
18. **Trianni V.** (2008), Evolutionary Swarm Robotics: Evolving Self-organising Behaviours in Groups of Autonomous Robots, *Studies in Computational Intelligence*, 108. Springer, Berlin.
19. **Urcola P., Riazuelo L., Lazaro M.T., Montano L.** (2008), Cooperative navigation using environment compliant robot formations, *IEEE/RSJ International Conference on Intelligent Robots and Systems*, 2789-2794.
20. **Wiech J., Eremeyev V.A., Giorgio I.** (2018), Virtual spring damper method for nonholonomic robotic swarm self-organization and leader following, *Continuum Mechanics and Thermodynamics*, 1-12, Springer, 2018

DOI 10.2478/ama-2019-0019 acta mechanica et automatica, vol.13 no.2 (2019)

ABILITY OF ENERGY HARVESTING MR DAMPER TO ACT AS A VELOCITY SENSOR IN VIBRATION CONTROL SYSTEMS

Maciej ROSÓŁ,[*] Bogdan SAPIŃSKI[**]

[*]Faculty of Electrical Engineering Automatics Computer Science and Biomedical Engineering, Department of Automatic Control and Robotics, AGH University of Science and Technology, Al. Mickiewicza 30, 30-059 Kraków, Poland
[**]Faculty of Mechanical Engineering and Robotics, Department of Process Control, AGH University of Science and Technology, Al. Mickiewicza 30, 30-059 Kraków, Poland

mr@agh.edu.pl, deep@agh.edu.pl

received 12 April 2019, revised 26 June 2019, accepted 28 June 2019

Abstract: The study investigates the self-sensing ability in an energy harvesting magnetorheological damper (EHMRD). The device consists of a conventional linear MR damper and an electromagnetic harvester. The objective of the work is to demonstrate that the EHMRD with specific self-powered feature can also serve as a velocity sensor. Main components of the device and design structure are summarized and its operation principle is highlighted. The diagram of the experimental set-up incorporating the measurement and processing unit is provided, the experimental procedure is outlined and data processing is discussed. The self-sensing function is proposed whereby the relative velocity of the EHMRD can be reconstructed from the electromotive force (emf) induced in the harvester coil. To demonstrate the adequacy of the self-sensing action (i.e., the induced emf should agree well with the relative velocity), the proposed self-sensing function is implemented and tested in the embedded system that will be a target control platform. Finally, the test results of the system utilizing a switching control algorithm are provided to demonstrate the potentials of the EHMRD acting as a velocity sensor and to confirm its applicability in semi-active vibration control systems.

Key words: MR damper, energy harvester, self-sensing function, electromotive force, embedded system, algorithm

1. INTRODUCTION

It is a well-established fact that vibrating objects such as machines, equipment, vehicles, engineering structures and so on generate mechanical energy that might be used as an energy source. This energy, otherwise wasted, could be converted into usable electrical energy to power sensors or/and actuators, thus eliminating the need of external energy power sources, making the systems self-powered. Inspired by this concept, researches have already achieved the most promising results in the energy harvesting area.

Most studies on EHMRDs have focused on their self-powered ability whilst less attention has been given to their self-sensing feature. According to the authors, this aspect seems of great importance too, meriting full attention and extensive research efforts. The present study investigates this specific feature in the engineered MR damper integrated with an electromagnetic energy harvester (Sapiński, 2014). Formerly, this damper was tested in a semi-active vibration control system employed in a 1 DOF mechanical structure configuration but research efforts at that time focused mainly on the self-powering feature of the device (Sapinski and Rosół, 2016).

The last decade has witnessed a major interest in EHMRDs. A growing number of research reports have been published, summarizing the developments and achievements in this area. It is worthwhile to mention that several solutions have already been patented. Recent advancements in the area of EHMRDs have been summarized in the work by Ahamed et al. (2016). This comprehensive review shows that the concept of MR dampers with power generation still remains a challenging problem. Moreover, extensive research efforts have been made to implement EHMRDs in automobiles, railway vehicles and so on, and to evaluate their performance. A thorough review of recent research reports on the subject is presented below.

Choi and Werely (2009) investigated the feasibility and efficiency of a self-powered MR damper using a spring-mass electromagnetic energy harvester. Zhu et al. (2012) investigated the feasibility of linear motion electromagnetic devices for civil infrastructure to be used for vibration damping and energy harvesting. Jung et al. (2010a) demonstrated that an electromagnetic energy harvester incorporated in the MR damper-based system may act as a velocity-sign sensor. Also, Jung et al. (2010b) showed that such a harvester could act as a relative velocity sensor in typical control strategies for MR damper-based systems. Wang et al. (2010) proposed an integrated relative displacement self-sensing MR damper to realize the integrated relative displacement sensing and controllable damping. Wang and Bai (2013) developed this idea and fabricated and tested such an MR damper prototype. Peng et al. (2011) formulated the concept and proposed the optimization of the self-sensing MR damper that superposes the information of the damper's motion to the emf signal, which can be further modulated via the feedback strategy. Chen and Liao (2012) investigated a newly developed MR damper prototype with self-powered and self-sensing abilities. Liao and Chen (2010) accordingly filed the patent application for the conceptual design of the device. Zhu et al. (2012) studied the self-powered and sensor-based MR damper systems, which could be particularly useful in large-scale civil structures where the power supply is impractical. Li et al. (2013a) presented an innovative concept of a

DOI 10.2478/ama-2019-0019

so-called mechanical motion rectifier, which converts bidirectional motion into unidirectional motion. Li et al. (2013b) developed a retrofittable design of a shock absorber based on permanent magnets and rack-pinion mechanism. Ni et al. (2015) developed and identified inverse dynamics of a self-sensing MR damper that may be applicable for structural control applications. Chen et al. (2015) presented a self-sensing MR damper with an embedded piezoelectric force sensor and demonstrated its reliable force sensing and controllable damping capabilities by the use of NARX modelling and neural network techniques. Hu et al. (2015) developed a novel MR damper with a self-induced ability integrated with a linear variable differential sensor based on the electromagnetic induction mechanism and evaluated its static and dynamic behaviour through experimental testing. Also, Hu et al. (2015) proposed a self-sensing MR damper with an electromagnetic induction mechanism, which has both good self-sensing ability and controllable damping capability. Xinchun et al. (2015) proposed an MR damper with a self-powered ability equipped with vibration energy harvesting mechanism based on ball-screw and a rotary permanent magnet dc generator, and indicated the feasibility of this configuration. Xinchun et al. (2017) developed the MR damper with velocity self-sensing mechanism based on the optical tracking technology and numerical circuit technology, and demonstrated its high accuracy monitoring capability and sufficient ability to control the MR damper. Ahamed et al. (2016) proposed an MR damper with the energy harvesting component, and through the tests, revealed the maximum induced output voltage.

The objective of the present study is to demonstrate that the engineered EHMRD that exhibits self-powered ability can also act as a velocity sensor in vibration control systems. The work is organized in the following manner. Section 2 outlines the structure of the EHMRD. Section 3 provides the harvester configuration, basic geometry and electrical parameters, and highlights its operating principles. Section 4 summarizes the experimental set-up description, the measurement and processing unit, the experimental and data analysis procedures. In Section 5, the main focus is on the self-sensing function, its identification and verification. This function has been implemented in the STM32F407 processor embedded system and the application with switching control algorithm is shown to confirm the harvester performance as a velocity sensor. Final conclusions are provided in Section 6.

2. STRUCTURE OF THE EHMRD

The cut-off view of the EHMRD is shown in Fig. 1. The device is symmetrical and incorporates two major components: the harvester and the MR damper. A piston rod (1) made of ferromagnetic steel moves inside a brass lid (2). Rubber seals (3) prevent MR fluid leaking. The rod is bolted to the piston (4). In the piston, there is the MR damper control coil (5) power-supplied via a wire (6) in the rod. The piston moves inside the damper housing (7) made of ferromagnetic steel and connected to the harvester housing (8) made of aluminium, via a brass connector (9). The piston is connected to the harvester via a rod (10) made of non-magnetic steel. On the rod in the harvester are three arrays of ring-shaped neodymium magnets, magnetized axially (11), separated from one another by spacers (12) made of ferromagnetic steel. The diameter of the magnets is identical to that of the spacers. Magnets and the rod move inside the immobile housing (13) made of ferromagnetic steel. The harvester's coil (14), wound on the carcass and placed inside the housing, has two-sections with copper foil. The sections are connected such that induced emfs should sum up. The middle point along the height of the sections coincides with the point half-way between the magnet arrays. The aluminium lid (15) locks the harvester coil housing in place. Linear guiding of the damper rod and harvester is affected through the use of slip sleeves (16). A holder (17) is bolted to the lid in the damper, enabling its assembly in various configurations.

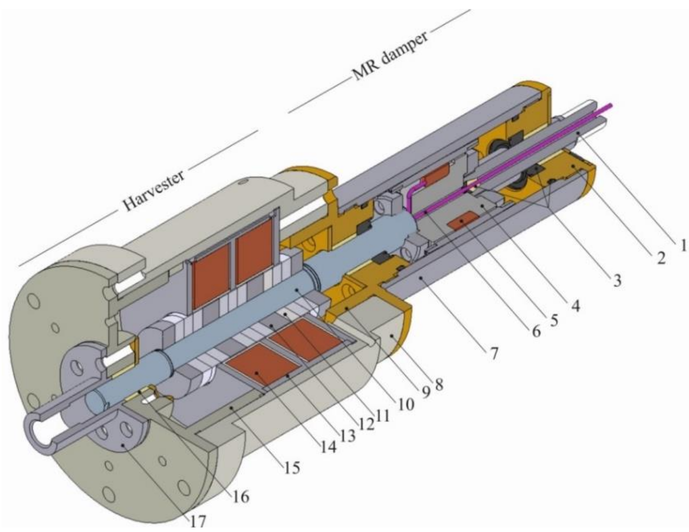

Fig. 1. EHMRD; cut-off view

3. CONFIGURATION AND OPERATING PRINCIPLE OF THE HARVESTER

This configuration of the harvester has evolved as the results of extensive research efforts collated in Sapiński (2008; 2010, 2013). These studies summarized the numerical calculations, design considerations, fabrication and experimental testing procedures, and engineering of the electromagnetic harvester for a linear MR damper. The present harvester configuration is shown in Fig. 2a. Dimensions of its main components are as follows:

DOI 10.2478/ama-2019-0019

magnets (h_m = 5 mm, d_{mi} = 20 mm, d_{me} = 80 mm), coil (H_c = 54 mm, d_{ci} = 86 mm, d_{ce} = 127.6 mm), spacers (H_g = 20 mm), carcass (H_{ca} = 58 mm, g_{ca} = 2 mm), coil housing (H_h = 86 mm, w_h = 3 mm). The copper foil used in the harvester coil is 50 mm in width and 0.05 mm in thickness, with one-sided insulation 54 mm wide and 0.03 mm thick. The winding sections have identical height and the number of turns is 273. The height of an air slit between the carcass and the system of magnets is 1 mm.

Fig. 2b illustrates the magnetic flux distribution calculated with respect to the centre of the harvester coil winding sections (Coil H1 and Coil H2). It is apparent that the harvester coil's housing and a portion of the magnets is permeated by the magnetic flux linkage encompassing the coil turns. The magnet systems assembly and coil assembly of the harvester are shown in Figs. 2c, d.

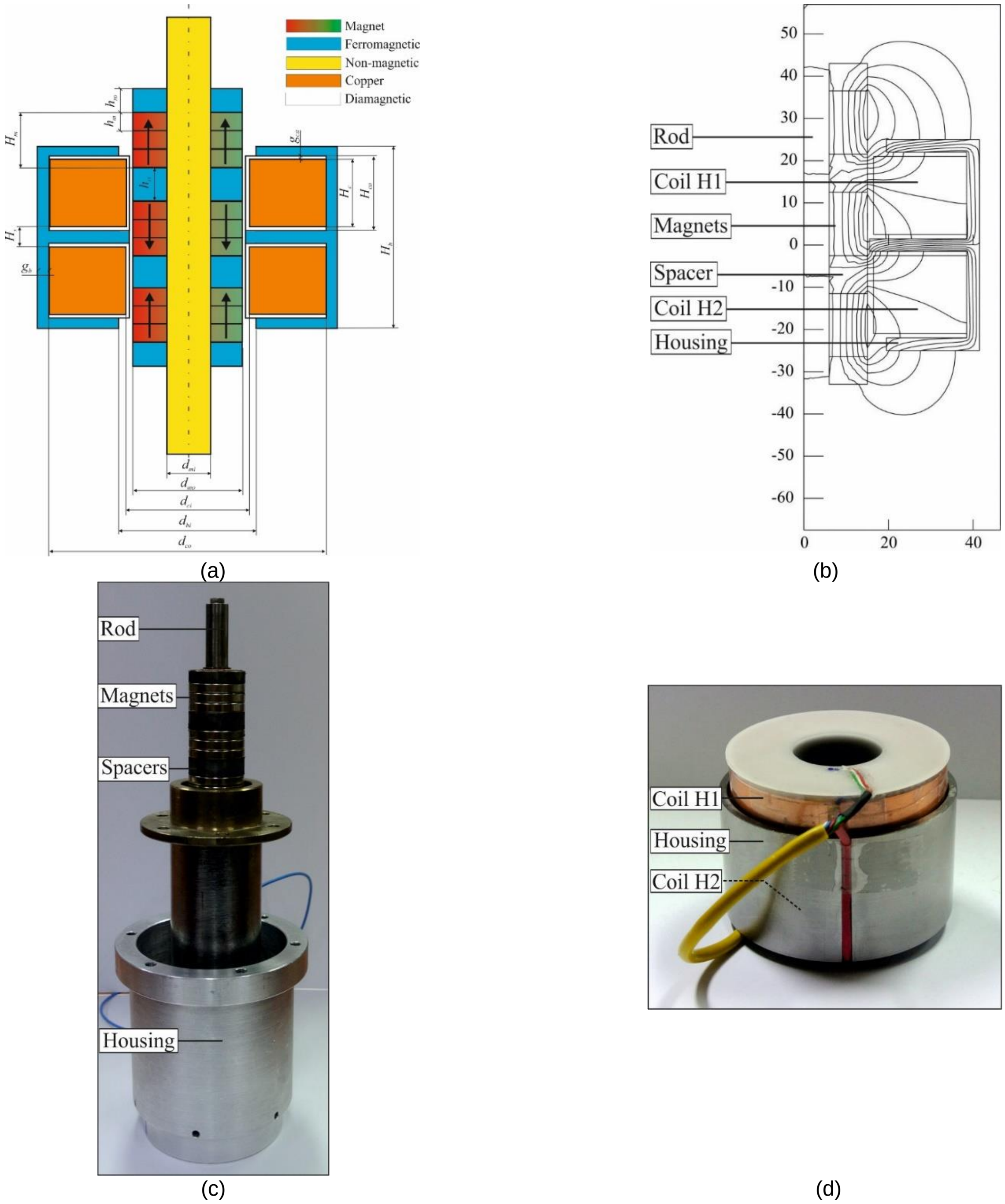

Fig. 2. Harvester: (a) schematic diagram, (b) magnetic flux density map, (c) magnet systems assembly, (d) coil assembly

The operating principle of the harvester unit relies on Faraday's law, which states that relative motion of stationary magnets with respect to the coil will induce an emf. This emf is proportional to the velocity across the device, and hence, it may serve as a velocity sensor. The concept of using the harvesting component to reconstruct the velocity signal and to supply the MR damper is illustrated in an equivalent circuit in Fig. 3. For simplicity, let us assume that all circuit components are linear. When the switch contact is in the 'close' position, Coil H1 (resistance R_1 and inductance L_1 in series) acts as a measuring coil since it will have

DOI 10.2478/ama-2019-0019

the induced emf e. When the switch contact is in the 'open' position, Coil H2 (resistance R_2 and inductance L_2 in series) acts as the coil supplying the MR damper (resistance R_d and inductance L_d in series). Depending on the switch position, the EHMRD operates either under idle run (as a sensor) or under the load (as an energy source). One has to bear in mind that the core loss effect in the device has been neglected because of low-frequency excitations during the tests. In order to account for core loss effects, it is required that an equivalent resistance in parallel with inductance L_d should be incorporated in the circuit in Fig. 3. Resistance of the harvester coil (Coil H1 and Coil H2) becomes $R_1 + R_2 = 2.45$ Ω and inductance $L_1 + L_2 = 141$ mH. Resistance of the MR damper coil is $R_d = 3.6$ Ω and inductance $L_d = 71$ mH.

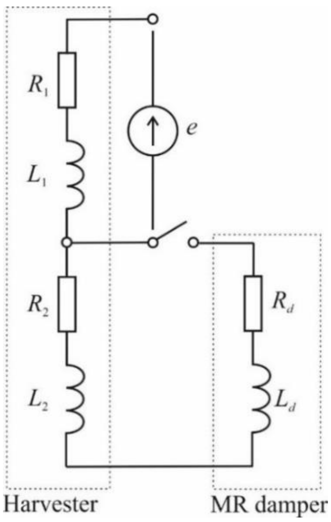

Fig. 3. Equivalent circuit of the EHMRD under idle run and under the load

4. EXPERIMENTS AND DATA ANALYSIS

To obtain the data requisite for the reconstruction of velocity across the EHMRD, measurements were taken of emf induced in the harvester coil in the experimental set-up incorporating a testing machine MTS 810 controlled via a FlexTest SE controller (MTS, 2006). The diagram of the experimental set-up is shown in Fig. 4. The measurement unit based on high-precision operational amplifiers was used for gain regulation and to offset the measured analogue quantities. The processing unit, based on the STM32F407 processor, has all the requisite peripheral systems ensuring the sufficient computational capacity of CPU and FPU units (STMicroelectronics, 2017). Embedded system was tested using the following peripheral blocks integrated in the structure: analogue-digital converter (ADC), timers/counters units capable of interrupts and PWM signal generation, and a serial port UART. Two channels of a 12-bit A/D converter are responsible for velocity and emf measurements, conditioned by the measurement unit. The measurement unit converts the measured voltages into voltages from the range (0, +3.3) V, acceptable by STM32F407 processor. Thus, the processed data are duly transmitted (via an UART port), monitored and uploaded to a PC. Recorded data are sampled with the frequency of 1 kHz (periodical interrupt-driven function). Four additional digital outputs pin of STM32F407 processor are used to measure the sample time period (T_0), time duration of velocity reconstruction from emf (T_A), time duration of control algorithm (T_C) and time of data transmission (T_S).

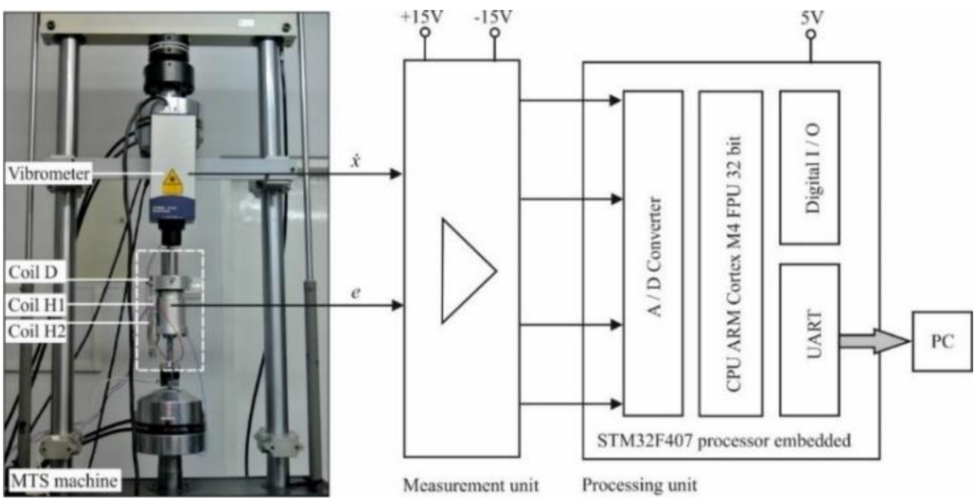

Fig. 4. Diagram of the experimental set-up

Measurement data were registered in the two modes of the EHMRD's operation: under idle run and under the load, the applied inputs were sine and triangular displacements of the piston rod with the amplitude 5 mm and frequency varied from 1 to 7 Hz with 1 Hz increments. These levels of input amplitude and frequency were designed in the context of potential implementation of the EHMRD in a semi-active vibration reduction system. Velocity $\dot{x}$ was measured with a laser vibrometer (Polytec, 2005), with resolution 0.1 μm/s (the level for 1 Hz) for the ADC voltage range ±10 V. Measurement data were recorded, analysed and processed using a PC computer supported by MATLAB/Simulink.

To reconstruct the velocity across the EHMRD, the authors propose the self-sensing function that is determined in a multi-stage procedure. Stage 1 consisted of the initialization of the peripheral systems and parameters of the processing unit. In Stage 2, the type and parameters of the input excitations (piston rod displacement x) were selected, alongside the operating mode of the device (under idle run or under the load). In Stage 3, the velocity $\dot{x}$ and emf data registered under idle run (e) and under the load (e_L) were uploaded to a PC. Stage 4 involved the analysis of measurement data supported by MATLAB; moreover, the actual form and parameters of the self-sensing function were determined accordingly. In Stage 5, the self-sensing function was verified using a different set of data.

In Stage 4, the measurement data were analysed and processed in the time and frequency domain. The time-domain analysis involved the comparison of time histories of velocity $\dot{x}$ and emf e, in the case of the frequency domain analysis, the Digital Fourier Transform (DFT) values of respective quantities were compared for the assumed inputs excitations x. DFT modulus was calculated using the *fft.m* of MATLAB function based on the Cooley-Tukey algorithm (Frigo and Johnson, 2005). The number equal to the nearest power of 2 greater than the length of the registered data was used as the FFT points number. The missing data of an input vector are padded with trailing zeros to the determined FFT length.

Figs. 5 a, b show time histories of velocity $\dot{x}$, emf e (under idle run) and e_L (under the load) applied to the Coil H1, at frequency 1 Hz and 7 Hz. These quantities are found to be in phase and they reach the zero value at identical time instants. Differences between time histories of e and e_L appear to be minor. The maximal relative difference approaches 0.1052 at 1 Hz and 0.1748 at 7 Hz. The integral of the squared error per period is 2.2293 at 1 Hz and 0.9561 at 7 Hz. Similar differences and error values are registered at other frequencies.

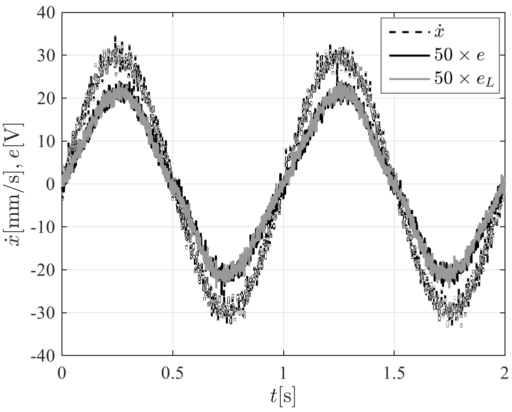

(a) sine input, *f* =1 Hz

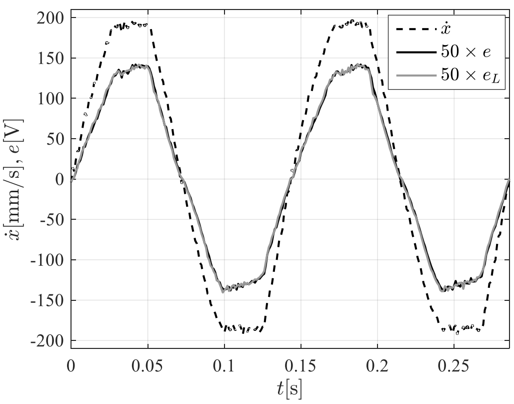

(b) sine input, *f* =7 Hz

Fig. 5. Time history of velocity and emf; sine input

Figs. 6 a, b plot the DFT modulus of $|\dot{X}(f)|$ and emf under idle run $|E(f)|$ and under the load $|E_L(f)|$ applied to the coil A, at frequency 1 and 7 Hz. Apparently, the differences between DFT modulus of $|E(f)|$ and $|E_L(f)|$ are rather small. The maximal relative difference is 0.32 at 1 Hz and 0.2 at 7 Hz. The integral of the squared error calculated at frequency range (1, 10) Hz equals 0.0018 at 1 Hz and 0.011 at 7 Hz. Similar results were obtained at other frequencies.

It is reasonable to suppose, therefore, that the time history of rod velocity $\dot{x}$ could be reconstructed from emf readouts e.

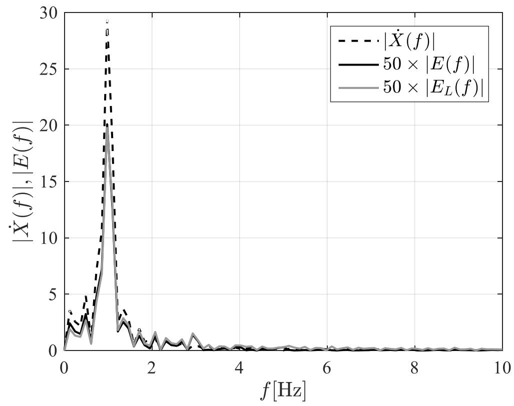

(a) *f* =1 Hz

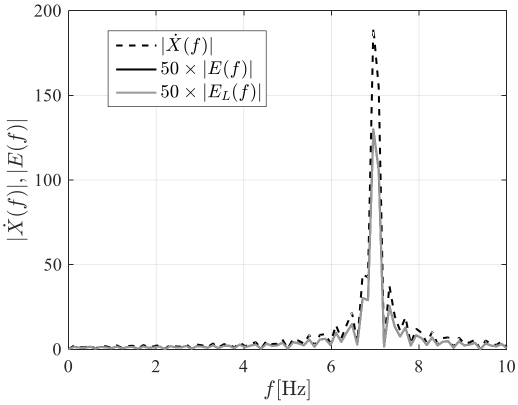

(b) f =7 Hz

Fig. 6. DFT values of velocity and emf; sine input

5. VELOCITY RECONSTRUCTION

5.1. Identification of self-sensing function

Following the discussion, the self-sensing function $\dot{x} = f(e)$ is proposed, defined by the first-order polynomial. When analysing the problem in time domain, the first harmonic amplitude of the velocity $\dot{X}_1$ and emf $\dot{E}_1$ calculated from the time series at each frequency in the range (1, 7) Hz yields the formula:

$$\dot{X}_1 = aE_1 + b \tag{1}$$

In frequency domain, the first harmonic modulus of the velocity $|\dot{X}_1(f)|$ and emf $|E_1(f)|$, determined from DFT series at each frequency in the range (1, 7) Hz, yields the formula:

$$|\dot{X}_1(f)| = a|E_1(f)| + b \tag{2}$$

The values of parameters a and b calculated by the least square

DOI 10.2478/ama-2019-0019

method (*polyfit* function available in MATLAB) are summarized in Table 1. Parameters *a* and *b* were obtained in the time domain and in the frequency domain for the sets of data registered under idle run (S_t^1, S_f^1), under the load (S_t^2, S_f^2) and jointly for the two modes (S_t^3, S_f^3). The goodness of fit of $\dot{X}_1$ and $|\dot{X}_1(f)|$ to the predicted values derived from (1) and (2) was evaluated recalling the Pearson's linear correlation coefficient *r*. Fig. 7, 8 show the relationship (1) and (2) obtained for S_t^1 and S_f^1 data set.

Tab. 1. Calculated parameters *a*, *b* and correlation coefficient *r*

Domain	Data set	a	b	r
Time	S_t^1	73.24	0.011	0.9999993
	S_t^2	73.35	0.058	0.9999989
	S_t^3	73.31	0.035	0.9999981
Frequency	S_f^1	73.25	-0.0054	0.9999992
	S_f^2	73.34	0.044	0.9999993
	S_f^3	73.29	0.025	0.9999461

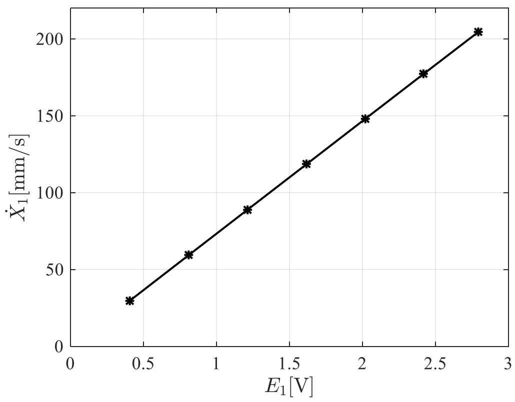

Fig. 7. First harmonic amplitude of velocity vs. first harmonic amplitude of emf

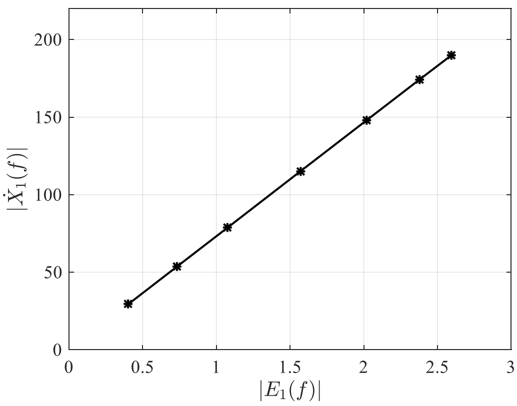

Fig. 8. Modulus of first harmonic of velocity vs. modulus first harmonic of emf

Actual values of parameters *a* and *b* in Table 1 were selected based on the computed values of MSE (Mean-Squared Error) between the measured velocity $\dot{x}$ and reconstructed velocity $\dot{x}_e$ defined as follows:

$$MSE = \frac{1}{M}\sum_{i=1}^{M}(\dot{x}_i - \dot{x}_{ei})^2 \quad (3)$$

where *M* is the number of samples per a single period of input displacement *x*(*t*).

Each pair of values of parameters *a* and *b* (Table 1) was recalled to compute the velocity $\dot{x}_e$ reconstructed from *e* for two data sets registered under idle run and under the load for each frequency in the range (1, 7) Hz.

Fig. 9 gives the medium MSE error computed for each data set, in accordance with the formula:

$$S_D^{m,n} = \frac{1}{K}\sum_{i=1}^{K} MSE(i) \quad (4)$$

where: *K* = 7 is the number of input frequencies; *D* = *t* in time domain or *D* = *f* in frequency domain; *m*, *n* = 1, 2, 3 are data sets used to obtain the parameters *a* and *b* (*m*) and to reconstruct velocity from emf (*n*).

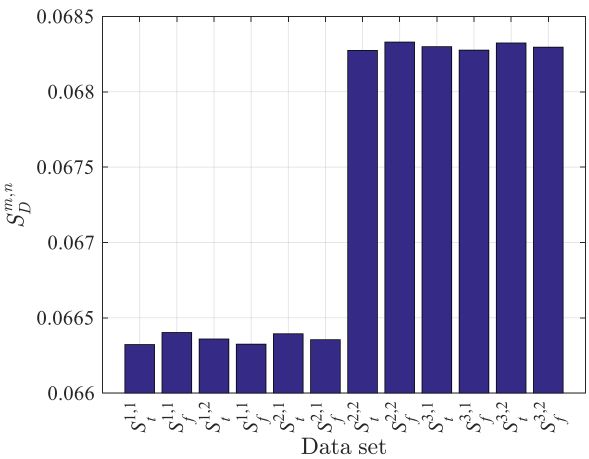

Fig. 9. Medium value of MSE error calculated for each data set

It appears that the smallest error value $S_D^{m,n}$ is obtained for *a* and *b* values derived for the data set $S_t^{1,1}$, that is why these values of a and b were recalled in further considerations. Fig. 10a, 10b compare the plots of measured velocity $\dot{x}$ with that reconstructed from formula (1) $\dot{x}_e$ for sine excitation inputs and at frequency 1 Hz and 7 Hz. Recalling the switching algorithms widely used in semi-active vibration control systems, such as sky-hook and ground-hook algorithms (Karnopp et al., 1974) expressed by formula (5) and (6), it is clearly apparent that in order to calculate the control u_{sky} or u_{grd}, the velocity $\dot{x}_e$ should be determined with sufficient precision.

$$u_{sky} = \begin{cases} u_s; \ \dot{x}_s \cdot \dot{x}_e \geq 0 \\ 0; \ \dot{x}_s \cdot \dot{x}_e < 0 \end{cases} \quad (5)$$

$$u_{grd} = \begin{cases} u_g; \ -\dot{x}_u \cdot \dot{x}_e \geq 0 \\ 0; \ -\dot{x}_u \cdot \dot{x}_e < 0 \end{cases} \quad (6)$$

where $\dot{x}_s$ is velocity of a sprung mass and $\dot{x}_u$ is velocity of an unsprung mass.

In the context of these algorithms, of particular importance are the points where the velocity sign should change. The maximum time between the instants when the signs of velocity $\dot{x}$ and $\dot{x}_e$ should change is found to be 600 μs, determined from the respective time histories. This value is almost equal to the sampling period 1 ms.

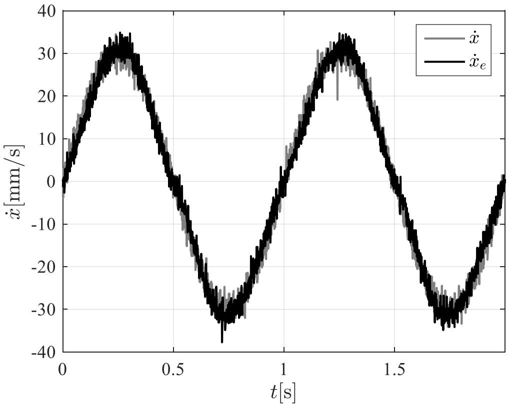

(a) f =1 Hz

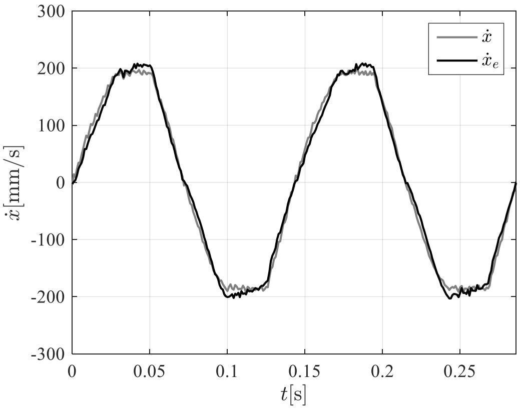

(b) f =7 Hz

Fig. 10. Time history of velocity measured and reconstructed from emf; sine input

5.2. Verification of self-sensing function

In order to verify the introduced self-sensing function, the triangle displacement input was applied. Figs. 11, 12 plot velocity $\dot{x}$ readout from vibrometer and the reconstructed velocity obtained under idle run $\dot{x}_e$ and under the load $\dot{x}_{eL}$. It appears that the time instants when the velocity sign is changed are determined with the level of accuracy 600 μs. Most significant differences are registered for constant values of velocity $\dot{x}_e$ and $\dot{x}_{eL}$, which is associated with the steady-state emf value having approached emf (e).

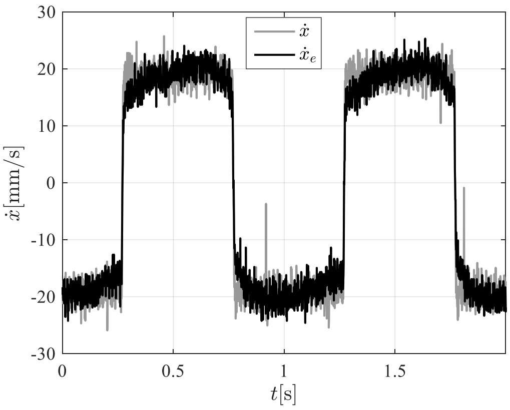

(a) under idle run

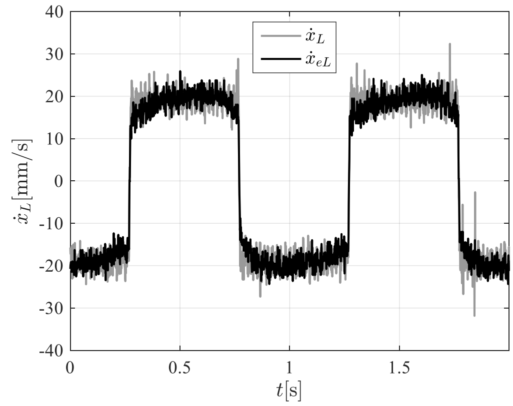

(b) under the load

Fig. 11. Time history of velocity measured and reconstructed from emf; triangle input, 1 Hz

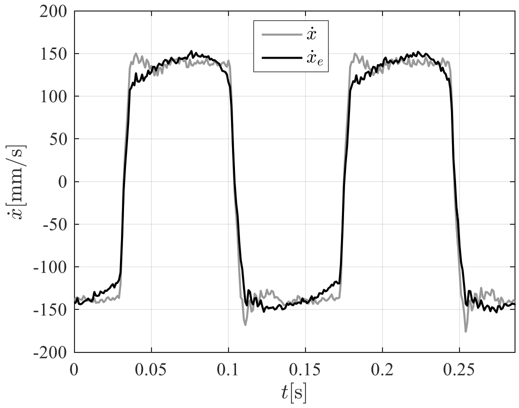

(a) under idle run

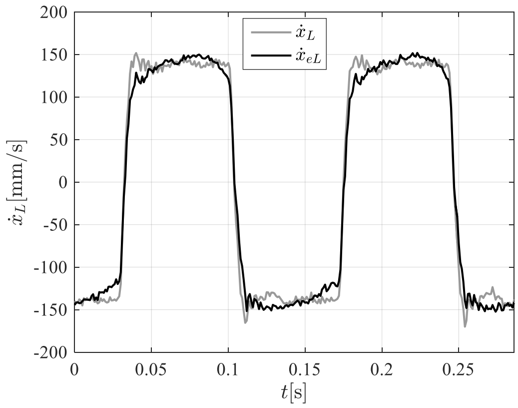

(b) under the load

Fig. 12. Time history of velocity measured and reconstructed from emf; triangle input, 7 Hz

5.3. Implementation and application of self-sensing function

The proposed and duly verified self-sensing function has been implemented and tested in a STM32F407 processor embedded system. For the purpose of testing, the clock and peripheral systems of the processor STM32F407 were duly configured and the adequacy of velocity measurement and velocity $\dot{x}$ reconstruction from emf e was tested. Further, testing was done to investigate the temperature correction of parameters *a* and *b* in the harvester characteristic and the effectiveness of the sky-hook algorithm.

DOI 10.2478/ama-2019-0019

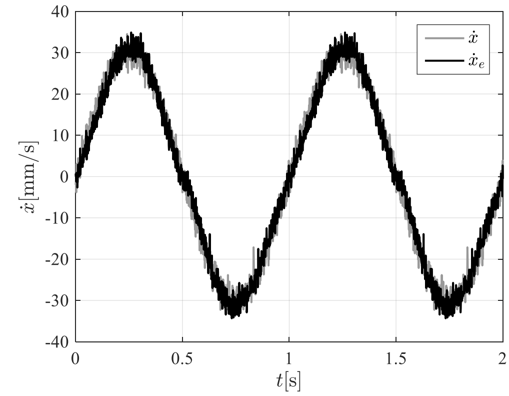

(a) *f* =1Hz

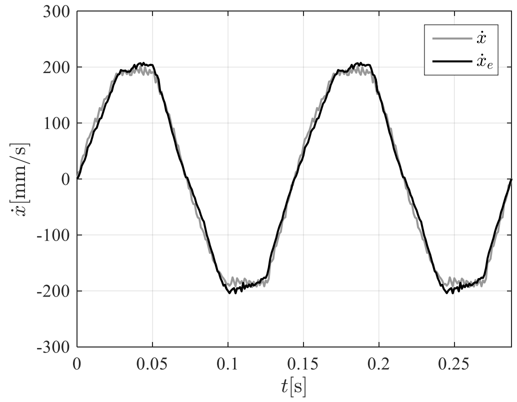

(b) *f* =7Hz

Fig. 13. Time history of velocity measured and reconstructed from emf signal; sine input

Figs. 13a, 13b show time histories of velocity $\dot{x}$ and velocity $\dot{x}_e$ derived in accordance with algorithm (1), initiated upon the processing unit for sine wave inputs at frequency 1 and 7 Hz. It appears that the results agree well with those given in Fig. 10, which confirms the effectiveness of channel configuration and the adequacy of the self-sensing function.

To illustrate the correction to the characteristic $\dot{X}_1 = g(E_1)$, emf generated by the harvester is assumed to be temperature-dependent. This effect is attributable to the reduced magnetisation of ferromagnetic steel with increasing temperature (Kittel, 1996). The proposed correction of the self-sensing function with respect to the measured temperatures involves the modification of values of coefficients *a* and *b*, according to the identified characteristics *a*(*T*) and *b*(*T*). Fig. 14 plots time histories of temperature and the values of coefficients *a* and *b*. Apparently, the value of *a* tends to increase with increasing temperature, thus compensating for the decrease of the emf generated by the harvester. In the investigated temperature range, the value of coefficient *b* remains almost unchanged. The temperature-dependence of *a* and *b* is illustrated in Figs. 15, 16.

The operating principle of the *sky-hook* control algorithm (5) running on STM32F407 under the applied sine inputs with frequency 1 Hz and 7 Hz is presented in Fig. 17a, 17b. The value of control u_{sky} is effected through comparing the readouts of instantaneous sprung mass velocity $\dot{x}_s$ and reconstructed velocity $\dot{x}_e$ values. When the energy in the system is to be dissipated, the value of control voltage u_{sky} is set equal to u_s, producing the current in the MR damper coil. At the remaining time instants when the velocity product $\dot{x}_s \cdot \dot{x}_e < 0$, the control value $u_{sky} = 0$, which corresponds to the current level equal to 0.

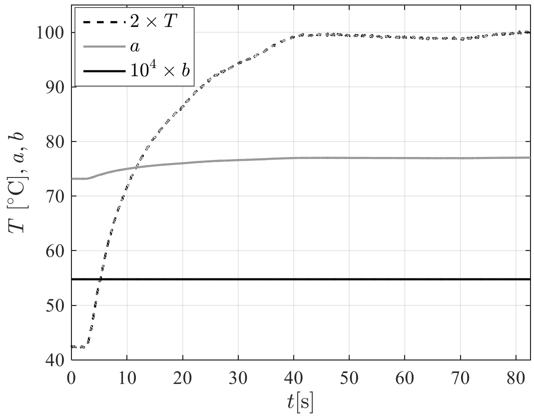

Fig. 14. Time history of temperature, coefficient *a* and *b*

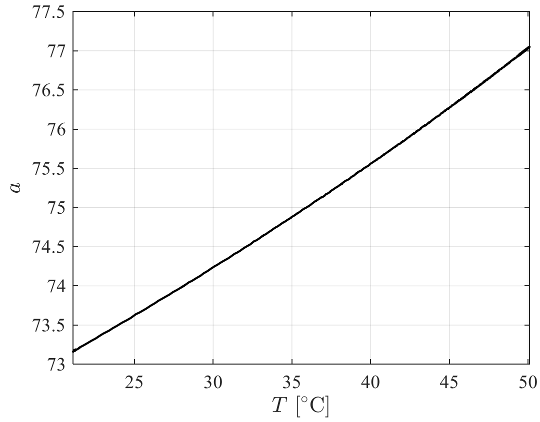

Fig. 15. Coefficient *a* versus temperature

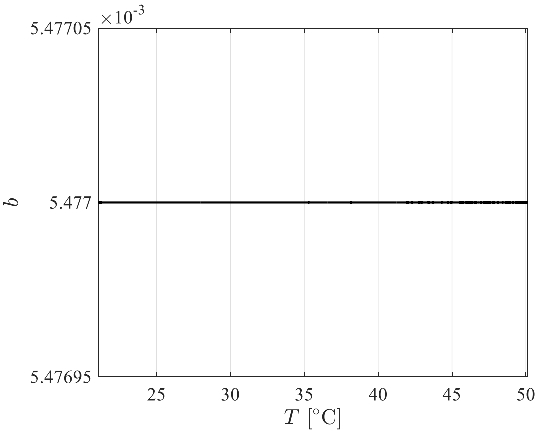

Fig. 16. Coefficient *b* versus temperature

Fig. 18 shows time histories of logic states for four STM32F407 processor digital outputs used for measuring the times: T_A, T_C, T_S and T_0. The logic state of the output was pre-set prior to the execution of the analysed code section, and then, reset after the task completion. The beginnings and ends of the measurement procedure: T_A, T_C, T_S and T_0 are indicated with arrows in Fig. 18. The time histories were registered with a logic analyser at the frequency 50 MSample/s.

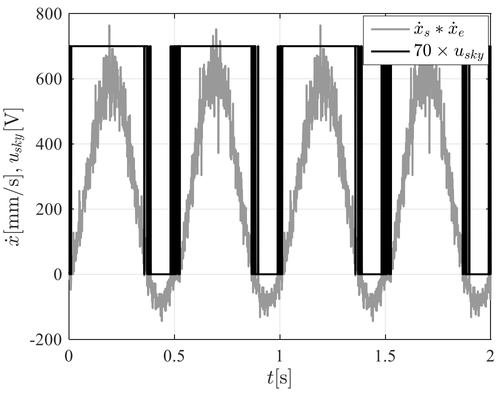

(a) f =1Hz

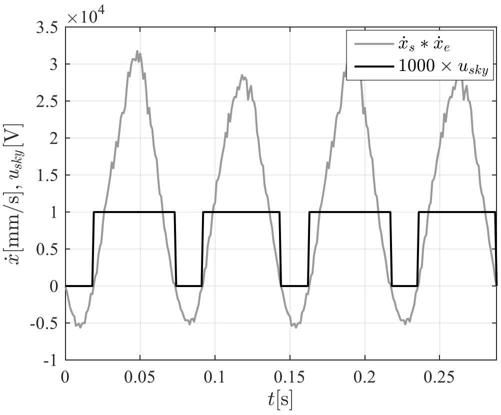

(b) f =7Hz

Fig. 17. Calculated velocity product and control; sine input

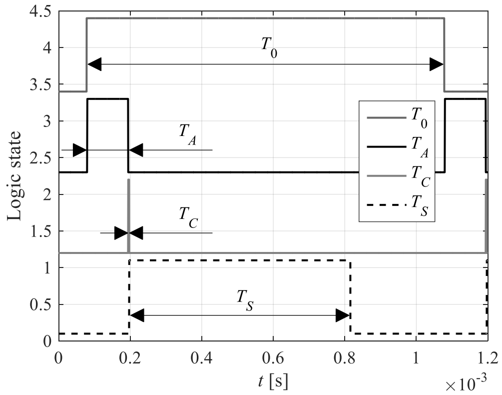

Fig. 18. Measurement of times T_0, T_A i T_S using logic analyser

A single measurement of T_A, T_C, T_S and T_0 is insufficient to confirm the time stability involved in particular phases of application code/algorithm execution; that is why, the measurement procedure had to be repeated several time. Results are summarized as histograms in Figs. 19–22. The velocity reconstruction time duration T_A is found to be 114.3 × 10^{-6} with jitter 10 × 10^{-9} s, the control algorithm time duration T_C is equal to 2.64 × 10^{-6} s with jitter 80 × 10^{-9} s. The time of data transmission T_S from the processing unit to the computer is equal to 620 × 10^{-6} s with jitters 2 × 10^{-6} s. The sample period T_0 equals 1 × 10^{-3} s with jitter 1 × 10^{-6} s. Actually, the sampling period in T_A, T_C, T_S and T_0 measurements can be taken as constant because the jitter is attributed mostly to the adopted method of measurements. The sum of control algorithm time duration and of data transmission time is found to be less than T_0. Actually, the final solution of the embedded system will not involve data transmission to a PC, which will vastly reduce the processor time, which should be spent on the implementation of advanced algorithms for correcting the characteristic $\dot{x} = f(e)$ and control of the EHMRD.

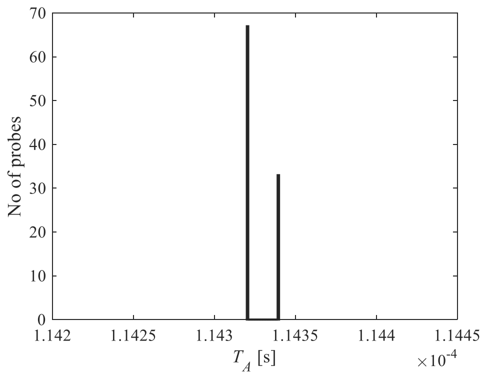

Fig. 19. Histogram of velocity reconstruction time duration T_A

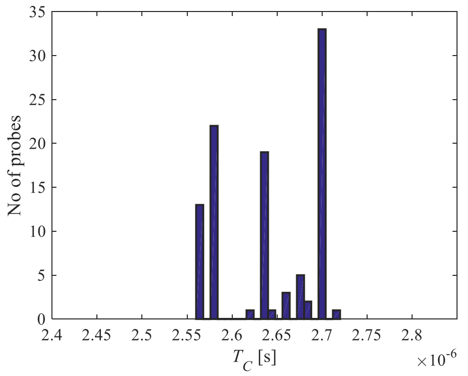

Fig. 20. Histogram of control algorithm time duration T_C

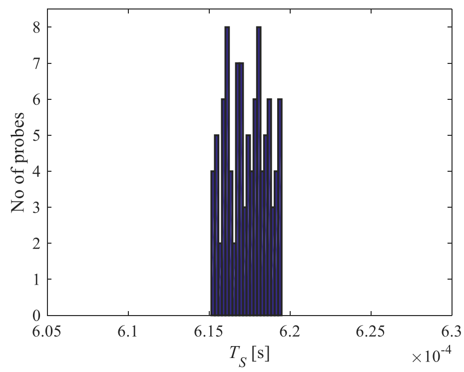

Fig. 21. Histogram of data transmission time T_S

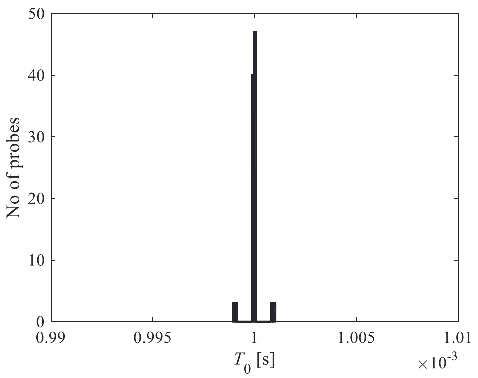

Fig. 22. Histogram of sampling time T_0

DOI 10.2478/ama-2019-0019

Power required to supply the measurement and processing unit determined using a power-supply DP832 (RIGOL, 2016) and a digital multimeter DM3058 (RIGOL, 2015) was found to be 0.4 W (supply voltage: +5 VDC, current: 80 mA). The power level was measured for the CPU operated in the run mode at 168 MHz, while the peripheral systems were active and supported by the application. The predicted current uptake by the CPU unit obtained in CubeMX taking into account all peripheral systems and GPIO becomes 46 mA (supply voltage +3.3 VDC, yielding the power ratings of. 0.15 W). Results summarized in the work (Sapinski and Rosół 2016) confirm that the EHMRD is capable of generating power sufficient to supply measurement and processing units. Power is generated for Coil H1 or Coil H2 at frequencies in excess of 2.5 Hz, with the amplitude 4 mm.

6. CONCLUSIONS

The primary objective of the study was to demonstrate that the EHMRD can act effectively as a velocity sensor and is applicable in semi-active vibration control systems. Accordingly, the self-sensing function is derived enabling the velocity EHMRD to be reconstructed from the emf induced in the harvester coil. The proposed function was verified, implemented and tested in the embedded system based on a STM32F407 processor.
The results lead us to the following conclusions:

- As regards the technical aspects, the proposed self-sensing function ensures the satisfactory levels of accuracy in reconstruction of velocity signals from emf measured in the harvester coil.
- Verification of the proposed self-sensing function revealed that a first-order polynomial can be well used in velocity reconstruction from emf readouts.
- The actual values of the self-sensing function parameters obtained in the time domain and in frequency domain allow the velocity reconstruction with similar accuracy levels (the maximum relative difference between the error values equals 3%).
- Time instants in which the velocity sign is changed are determined with sufficient accuracy allowing the implementation of switching algorithms,
- Implementation of the self-sensing function in the embedded system showed the results to be identical with those obtained using MATLAB.
- Efficiency of the embedded system is sufficiently high to allow for implementation of advanced strategies for control of EHMRD and for distribution of energy recovered by the harvesting component.
- To improve the accuracy of velocity reconstruction for piston rod inputs in the range (1, 3) Hz, it is required that emf signals should be low-pass filtered.
- Implementation of the self-sensing function in the embedded system, including the analogue signal measurement procedure, enables the 10-fold oversampling of emf measurements and operations on medium values.
- Analysis of the sample time period, time duration of velocity reconstruction from emf and time duration of control algorithm confirms the applicability of the embedded system to harvester control at vibration frequencies up to 200 Hz.

In further studies, the proposed self-sensing function used for velocity reconstruction and implemented on an embedded system will be applied in EHMRD-based vibration control system.

REFERENCES

1. **Ahamed R., Ferdaus M.M., Li Y.** (2016), Advancement in energy harvesting magneto-rheological fluid damper: A review, *Korea-Australia Rheology Journal*, 28(4), 355–379.
2. **Ahamed R., Rashid M.M., Ferdaus M.M., Yusuf H.B.** (2017), Modelling and performance evaluation of energy harvesting linear magnetorheological (MR) damper, *Journal of Low Frequency Noise Vibration and Active Control*, 36(2), 177–192.
3. **Chen C., Liao W.H.** (2012), A self-sensing magnetorheological damper with power generation, *Smart Materials and Structures*, 21 025014.
4. **Chen Z. H., Ni Y.Q., Or S.W.** (2015), Characterization and modeling of a self-sensing MR damper under harmonic loading, *Smart Structures and Systems*, 15, 1103–1120.
5. **Choi Y.T., Werely N.M.** (2009), Self-powered magnetorhelogical dampers, *Journal of Vibration Acoustics*, 131, 044501.
6. **Frigo M., Johnson S.G.** (2005), The Design and Implementation of FFTW3, *Proceedings of the IEEE*, 93 (2), 216–231. Invited paper, Special Isue on Pro-gram Generation, Optimization, and Platform Adaptation, http://www.fftw.org/fftw-paper-ieee.pdf.
7. **Hu G., Lu Y., Sun S., Li W.** (2017), Development of a self-sensing magnetorheological damper with magnets in-line coil mechanism, *Sensors and Actuators A: Physical*, 255, 71–78.
8. **Jung H.J., Jang D.D., Lee H.J., Lee I.W., Cho S.W.** (2010a), Feasibility Test of Adaptive Passive Control System Using MR Fluid Damper with Electromagnetic Induction Part, *Journal Engineering Mechanics*, 136(2), 254–259.
9. **Jung H.J., Jang D.D., Koo J.H., Cho S.W.** (2010b), Experimental Evaluation of a 'Self-Sensing Capability of an Electromagnetic Induction System Designed for MR Dampers, *Journal of Intelligent Material Systems and Structures*, 21, 837–836.
10. **Karnopp D.C., Crosby M.J., Harwood R.A.** (1974), Vibration control using semi-active force generator, *ASME Journal of Engineering for Industry*, 96(2), 619–626.
11. **Kittel C.** (1996), *Introduction to solid state physics*, John Wiley & Sons, Inc., Eighth Edition.
12. **Li Z., Zhuo L., Kuang J., Luhrs G.** (2013a), Energy-Harvesting Shock Absorber with a Mechanical Motion Rectifier, *Smart Materials and Structures*, 22, 028008.
13. **Li Z., Zhuo L., Luhrs G., Lin L., Qin Y.** (2013b), Electromagnetic Energy harvesting shock absorbers: design, modeling and road tests, *IEEE Transactions Vehicle Technology*, 62, 1065–74.
14. **Liao W.H., Chen C.** (2010), *Self-powered, sensing magnetorheological dampers US Patent Application*, 12/896,760.
15. **MTS System Corporation** (2006), *MTS 810 & 858 Material Testing Systems*, Technical Documentation.
16. **Ni Y.O., Chen Z., Or S.W.** (2015), Experimental Identification of a Self-Sensing Magnetorheological Damper Using Soft Computing, *Journal of Engineering Mechanics*, 141(7) 04015001.
17. **Peng G., Li W., Hu G., Alici G.** (2011), Design and simulation of a self- sensing MR damper, *15th International Conference on Mechatronics Technology*, 112–117.
18. **Polytec Inc**. (2005) OFV-505/503 *Vibrometer Sensor Head*, Technical Data, https://www.polytec.com.
19. **RIGOL Technologies Inc.** (2016), DP800 *Series Programmable Linear DC Power Supply*, Technical Data, https://www.rigol.com.
20. **RIGOL Technologies Inc.** (2015), *DM3068 6 ½ digits Digital Multimeter*, Technical Data, https://www.rigol.com.
21. **Sapiński B.** (2008), An experimental electromagnetic induction device for a magnetorheological damper, *Journal of Theoretical and Applied Mechanics*, 46, 4, 933–947.
22. **Sapiński B.** (2010), Vibration power generator for a linear MR damper, *Smart Materials and Structures*, 19, 105012.

23. **Sapiński B., Krupa S.** (2013), Efficiency improvement in a vibration power generator for a linear MR damper: numerical study, *Smart materials and Structures*, 22, 045011.
24. **Sapinski B.** (2014), Energy harvesting MR linear damper: prototyping and testing, *Smart Materials and Structures*, 23, 035021.
25. **Sapinski B., Rosół M., Węgrzynowski M.** (2016), Investigation of an energy harvesting MR damper in a vibration control system, *Smart Materials and Structures*, 25, 125017.
26. **STMicroelectronics** (2017), STM32F405/415, STM32F407/417, TM32F427/437 and STM32F429/439 advanced ARM®-based 32-bit MCUs, RM0090 Reference manual, Rev. 15.
27. **Wang D.H., Bai X.X., Liao W.H.** (2010), An integrated relative displacement self-sensing magnetorheological damper: prototyping and testing, *Smart Materials and Structures*, 19, 105008.
28. **Wang D.H., Bai X.X.** (2013), A magnetorheological damper with an integrated self-powered displacement sensor, *Smart Materials and Structures*, 22, 075001.
29. **Xinchun G., Yonghu H., Yi R., Hui L., Jinping Q.** (2015), A novel self-powered MR damper: theoretical and experimental analysis, *Smart Materials and Structures*, 24, 105033.
30. (2017), A novel velocity self-sensing magnetorheological damper: Design, fabricate, and experimental analysis, *Journal of Intelligent Material Systems and Structures*, 26, 527–540.
31. **Zhu S.Y., Shen W.A., Xu Y.L., Lee W.C.** (2012), Linear electromagnetic devices for vibration damping and energy harvesting: modeling and testing, *Engineering Structures*, 34, 198−212.

Acknowledgment: This work is supported by AGH University of Science and Technology under research program No. 16.16.130.942.

ABSTRACTS

Patryk Różyło
Passive Safety of a Buggy Type Car in the Aspect of a Dynamic Analysis of the Frame

This article presents passive safety issues of a buggy-type car. The issue has been presented in the context of the dynamic impact analysis of the aluminium frame of the vehicle into a rigid wall. The study was conducted using the finite element method in the Abaqus® software. With regard to numerical calculations, a dynamic impact simulation was performed, which defined the critical areas of the structure. Numerical analysis allowed to obtain both the state of the strain of the frame structure and the characteristics of the construction work during the impact. The results of the research provide high-quality prepared FEM model.

Volodymyr Zelenyak
Mathematical Modeling of Stationary Thermoelastic State for a Plate with Periodic System Inclusions and Cracks

Pallet flow rack are widely used in intralogistics to maximize warehouse capacity and to reduce the travel by fork-lifts. However, the use of pallet flow racks is associated with increased danger due to the use of gravity conveyors in their design. For this purpose, the gravity conveyors of pallet flow rack have a two safety elements – brake rollers and a stopping mechanism with pallet separator, which are working as a system. Brake rollers limit the speed of pallets, while the stopping mechanism allows exuding a pressure on the unloading pallet from the following behind it. A pallet should have such a speed, controlled by the brake rollers, so that it could be stopped by a stopping mechanism without damaging it. Based on the Cox impact theory, an original method for determining the allowable speed of a pallet in a pallet flow rack is proposed. The method ensures safe operation of the stopping mechanism with pallet separator and takes into account the mechanical properties and design parameters of the pallet separator stopper. A calculation example is provided for the most commonly used types of pallets – Euro pallet (1200 mm × 800 mm) and Industrial pallet (1200 mm × 1000 mm). The obtained results agree well with the pallet speed range of 0.2 to 0.3 m/s recommended by the manufacturers of pallet flow racks.

Vladimir Morkun, Ihor Kotov
Intellectualization of Emergency Control of Power Systems on the Basis of Incorporated Ontologies of Knowledge-Bases

The research deals with improvement of methods and systems of controlling integrated power systems (IPSs) on the basis of intellectualization of decision-making support. Complex analysis of large-scale accidents at power facilities is performed, and their causes and damages are determined. There is substantiated topicality of building condition knowledge-bases as the foundation for developing decision-support systems in power engineering. The top priorities of the research include developing methods of building a knowledge base based on intensity models of control actions influencing the parameters of power system conditions and introducing the smart system into information contours of the automated dispatch control system (ADCS), as well as assessing practical results of the research. To achieve these goals, the authors apply methods of experiment planning, artificial intelligence, knowledge presentation, mathematical simulation, and mathematical statistics as well as methods of power systems studying. The basic research results include regression models of a power system sensitivity to control actions, methods of building a knowledge base based on the models of sensitivity matrices, a structure of the smart decision-support system, a scheme of introducing the decision-support system into the operating ADCS environment. The problem of building a knowledge base of the dispatch decision-support system on the basis of empirical data resulted from calculating experiments on the system diagram has been solved. The research specifies practical efficiency of the suggested approaches and developed models.

Volodymyr Iasnii, Petro Yasniy
Degradation of Functional Properties of Pseudoelastic NiTi Alloy under Cyclic Loading: an Experimental Study

The influence of the cyclic loading on the functional properties of NiTi was studied. Cylindrical specimens with a diameter of 4 mm and a gage length of 12.5 mm were tested under uniaxial cyclic loading with control crosshead displacement at a temperature of 0°C. The dependences of the stress and strain range as well as dissipation energy on the number of loading cycles at different initial stress range were analysed. During the first 10 loading cycles, a rapid decrease in the strain range and energy dissipation was observed. Dissipation energy was invariant to the loading cycles' number at $N > 20$ cycles and to the stress range that did not exceed the martensite finish stress level, was within the same scatter band and can be described by the single dependence. With the stress range growth at $N < 20$ cycles from 509 to 740 MPa, the value of dissipation energy increases and that of relative dissipation energy decreases. Loss coefficient, which characterises material damping ability, significantly decreases during the first 10 loading cycles and remains practically unchanged up to the failure of the specimens. At the stabilisation area, the loss coefficient is almost non-sensitive towards the stress range.

Oleh Knysh, Ivan Rehei, Nazar Kandiak, Serhij Ternytskyi
Experimental Evaluation of the Tractive Effort of the Chain Conveyor During Book Block Spine Processing by Cylindrical Milling Cutter at Perfect Binding

The article reports on a device for book block spines processing that was designed and assembled on a perfect binding machine Trendbinder. The article shows workability of designed device. The authors have developed a methodology for the experimental study of the tractive effort of chain conveyors by technological load, the wireless module for data measurement and software for its processing. Extensive coverage is given to experimental research of the tractive effort of chain conveyors during book block spine processing depending on book block velocity, type of paper from which they are made and setting angle of cylindrical milling cutter relatively to direction of book blocks movement. The authors have examined the change in the tractive effort. The article experimentally confirms that sluggishness of chain drive causes vibration of the tractive effort. This effect can be observed during free-running movement of chain with carriers of perfect binding machine as well as during technological load influence. The article describes that between research parameters the setting angle of cylindrical milling cutter has the main impact relatively on the direction of book blocks movement.

Leon Kukiełka, Radosław Patyk, Łukasz Bohdal, Wojciech Napadłek, Rafał Gryglicki, Piotr Kasprzak
Investigations of Polypropylene Foil Cutting Process Using Fiber Nb:Yag and Diode Nd:YVO4 Lasers

Lasers are widely used in a variety of manufacturing processes including: depaneling, drilling, cutting, repair, trimming, micromachining. Polypropylene foils are intensively investigated as materials with great number of potential applications. Laser cutting is a major operation used in forming these materials and preparing the final workpieces. At the moment, the main challenge when cutting polypropylene is to obtain high quality products characterized by optimum sheared edge condition, minimum surface damage, freedom from burrs, slivers, edge wave, distortion, residual stresses and to obtain minimum width of HAZ zone. The amount of adjusTab. process parameters and the fact that the influence of these parameters on the process is not fully understood makes it difficult to control the cutting process. In practice, the right setup for the lasers is mostly found by trial and error combined with experience. Therefore, the final product frequently has serious defects. The paper presents the possibility of using fiber and diode lasers for forming of workpieces from polypropylene multilayer foil using cutting technology. The effect of selected process parameters and conditions on quality of sheared edge and material degradation is discussed.

Vladimir Golik, Vladimir Morkun, Natalia Morkun, Vitaliy Tron
Investigation of Mechanochemical Leaching of Non-Ferrous Metals

The research deals with metal extraction from off-grade ores and concentration tailings. There are provided results of simulating parameters of reagent leaching of metals in the disintegrator according to the metal recovery ratio. The research substantiates the method of waste-free processing of chemically recovered ores. Recovery of metals into solution is the same both under multiple leaching of tailings or ore in the disintegrator and agitation leaching of tailings or ore previously activated in the disintegrator with leaching solutions. The time of agitation leaching is more by two orders of magnitude than that of the disintegrator processing. Recovery of metals into solution is most affected by the content of sodium chloride in the solution. Then, in decreasing order, go the content of sulfuric acid in the solution, the disintegrator rotor rpm and L:S ratio.

Dorota Kula, Ewaryst Wierzbicki
Surface Localized Heat Transfer Equation for Periodic Composites

A characteristic feature of the description of physical phenomena formulated by an appropriate boundary or initial-boundary value problem and occurring in microstructured materials is the investigation of the unknown field in the form of decomposition referred to as micro-macro hypothesis. The first term of this decomposition is usually the integral average of the unknown physical field. The second term is a certain disturbance imposed on the first term and is represented in the form of a finite or infinite number of singleton fluctuations. Mentioned expansion s usually referred to as a two-scale expansion of the unknown physical field. In the paper, we purpose to apply two-scale expansion in the form of a certain Fourier series as a result of an applying Surface Localization of the unknown field. The considerations are illustrated by two examples, which results in analytical approximated solutions to the Effective Heat Conduction Problem for periodic composites, including the full dependence on the microstructure length parameter.

Zenon Hendzel, Jakub Wiech
Robotic Swarm Self-Organization Control

This article proposes a new swarm control method using distributed proportional-derivative (PD) control for self-organisation of swarm of nonholonomic robots. Kinematics control with distributed proportional-derivative (DPD) controller enables generation of desired robot trajectory achieving collective behaviour of a robotic swarm such as aggregation and pattern formation. Proposed method is a generalisation of virtual spring-damper control used in swarm self-organisation. The article includes the control algorithm synthesis using the Lyapunov control theory and numeric simulations results.

sciendo
acta mechanica et automatica, vol.13 no.2 (2019)

Maciej Rosół, Bogdan Sapiński

Ability of Energy Harvesting MR Damper to Act as a Velocity Sensor in Vibration Control Systems

The study investigates the self-sensing ability in an energy harvesting magnetorheological damper (EHMRD). The device consists of a conventional linear MR damper and an electromagnetic harvester. The objective of the work is to demonstrate that the EHMRD with specific self-powered feature can also serve as a velocity sensor. Main components of the device and design structure are summarized and its operation principle is highlighted. The diagram of the experimental set-up incorporating the measurement and processing unit is provided, the experimental procedure is outlined and data processing is discussed. The self-sensing function is proposed whereby the relative velocity of the EHMRD can be reconstructed from the electromotive force (emf) induced in the harvester coil. To demonstrate the adequacy of the self-sensing action (i.e., the induced emf should agree well with the relative velocity), the proposed self-sensing function is implemented and tested in the embedded system that will be a target control platform. Finally, the test results of the system utilizing a switching control algorithm are provided to demonstrate the potentials of the EHMRD acting as a velocity sensor and to confirm its applicability in semi-active vibration control systems.